QUANTITATIVE RESERVOIR CHARACTERIZATION USING HIGH-RESOLUTION SEISMIC VELOCITY STRUCTURE AND ROCK PHYSICS MODEL

カクダ, クレット

https://doi.org/10.15017/2534444

出版情報：Kyushu University, 2019, 博士（工学）, 課程博士
バージョン：
権利関係：

QUANTITATIVE RESERVOIR CHARACTERIZATION USING HIGH-RESOLUTION SEISMIC VELOCITY STRUCTURE AND ROCK PHYSICS MODEL

KAKDA KRET

2019

QUANTITATIVE RESERVOIR CHARACTERIZATION USING HIGH-RESOLUTION SEISMIC VELOCITY STRUCTURE AND ROCK PHYSICS MODEL

by

Kakda Kret

A dissertation summited in partial fulfillment of requirements

for the degree of

Doctoral Engineering

Examination Committee:

Prof. Takeshi Tsuji (Chairman)

Prof. Yasuhiro Fujimitsu

Prof. Hemanta Hazarika

九州大学

KYUSHU UNIVERSITY

Department of Earth Resources Engineering

Graduate School of Engineering

Kyushu University

Japan

July 2019

Abstract

The accurate identification of geological structures (i.e., faults and gas chimneys) and rock properties is required in oil/gas exploration and development. Three- or four-dimensional seismic reflection survey are commonly conducted to image geological structure, estimate physical/hydraulic properties and identify dynamic behaviors of the oil/gas reservoirs. Enhancing the geological information using the seismic data contributes to reduce risks during reservoir exploration, especially in new areas with lack of wells. Furthermore, mapping of the distribution of gas hydrate and free gas in deep water sediment of the plate convergent margin is important for both in evaluation of potential hydrocarbon resources and prevention of submarine geo-hazards. In addition, the quantitative reservoir characterization is important in environmental problem. One of the potential solutions to reduce the amount of emitted CO_2 into atmosphere is to store CO_2 in the geological formations. The CO_2 geological storage can be conducted in the geological formation that has been focusing on oil and gas exploration and development.

Several subsurface characterization techniques have been developed for exploration in reservoirs, including the analysis of seismic data combined with rock physics model. In this study, I used and advanced these methodologies to elucidate the distribution of gas hydrate and free gas in the Sanriku-Oki forearc basin, northeast Japan. To quantify seismic data (i.e., hydraulic and elastic property estimation), furthermore, I developed a new rock physics method to estimate pore geometry and grain elastic moduli. This thesis was divided into four chapters as summarized below.

Chapter 1 describes the background, motivation and objective of this study. Then, I introduce the previous/ongoing studies about seismic data interpretation and rock physics models for reservoir characterization.

In Chapter 2, automated velocity analysis was applied to a 3D seismic data volume in order to obtain a high-resolution seismic velocity model that I used to investigate the influence of fluid behavior on the subsurface distribution of gas hydrate in the Sanriku-Oki

forearc basin, northeastern Japan. I identified free-gas accumulations as zones of low P-wave velocity separated from overlying high-velocity gas hydrates by the clear seismic boundary of the Bottom-Simulating Reflector (BSR). Then, the conductive modeling was used to map upward heat flow in our study area from the depth of the BSR derived from the high-resolution velocity model. The BSR-derived heat flow demonstrated that upward fluid flux has a considerable influence on the distributions of both gas hydrate and free gas. The areas of high heat flow (representing fluid flow) corresponded to underlying permeable geological features such as gas chimneys, faults, and the edges of porous slumps, suggesting that these features provide fluid migration pathways from Eocene to Oligocene source rocks to free-gas and gas-hydrate accumulations in overlying sedimentary rocks. The techniques I have employed can contribute to the quantification of gas-hydrate and free-gas resources in similar deep-water reservoirs off the eastern continental margin of Japan and at tectonically similar plate subduction margins in other regions.

In Chapter 3, a grid-search inversion method was proposed to estimate pore geometry and grain elastic moduli from observed velocity–porosity relationships. This approach could be useful to predict hydraulic properties from seismic velocity. In the inversion, laboratory-derived velocity–porosity relationships were compared with the theoretical relationship calculated from crack aspect ratio and grain elastic moduli via the Differential Effective Medium (DEM) model. Compared with existing approaches to estimate elastic moduli and pore geometry, our approach is easy to apply because it can be applied to physical properties measured at atmospheric pressure without changing pressure. I tested the proposed inversion method using synthetic data, and successfully estimated the grain elastic moduli and crack aspect ratio. I also applied the proposed inversion method to *P*-wave velocity and porosity measured in the laboratory on various rock samples acquired at the hydrothermal field and plate-spreading center, and found that the velocity–porosity relationship derived from DEM theory for the inverted model parameters agreed with the laboratory data. Using the proposed method, the average pore aspect ratio and grain elastic moduli for basaltic and hydrothermal ore deposit samples were estimated. Furthermore, the Root Mean Square Error distribution obtained in the grid-search inversion enables us to evaluate the uncertainty of the estimated values.

Chapter 4 summarized new findings and new approaches in this dissertation. High-resolution seismic velocity models and heat flow prediction provided the key information to understand gas hydrate and free gas related to fluid flow in the Sanriku-Oki forearc basin, controlled by complex structural features (i.e. faults, chimneys, and edge of slumps) from deep source rock to shallow reservoirs. Furthermore, grid-search inversion was used to identify the pore geometry and grain elastic moduli using velocity-porosity relationship from discrete samples of hydrothermal ore deposit, which could be used to estimate hydraulic property of reservoir rocks from seismic velocity. The methodologies developed in this study could be combined for quantitative reservoir characterization.

Table of Contents

List of Figures

List of Tables

Chapter 1

Introduction

1-1 Research background and motivations

What is gas hydrate?

Gas hydrate is an ice-like crystalline substance, trapping a large amount of gas molecules within water molecule lattices (Kvenvolden, 1993). It extensively occurs on continental slopes and rises under low temperature and high-pressure condition. Gas hydrate is widespread in permafrost regions and beneath the sea in sediments of continental margins (Figure 1-1; Krey et al., 2009). Hydrates occur in different crystalline structures. The three most common types are structure I (sI), structure II (sII), and structure H (sH) (Figure 1-2) (Collett et al., 2009). The amount of gas present in the form of hydrates around the world has been estimated to range from 10^5 to 10^6 Tcf (US Department of Energy, 2007). Gas hydrates are viewed as a cleaner resource given that methane has a lower carbon content than conventional fuels such as coal (Englezos and Lee, 2005). Biogenic gas is dominantly composed of methane and thermogenic gas contains heavier hydrocarbons. Biogenic gas is a widespread component in shallow marine sediments in areas with high primary productivity, while production of thermogenic gas, apart from the organic matter supply, depends on anoxic conditions and sedimentation burial depths over long periods. The characterization of hydrate deposits involves collection and interpretation of geophysical, geochemical, sedimentological and thermal data. Recent studies in a number of marine sedimentary systems such as Hydrate Ridge (Suess et al., 2001), Nankai Trough (Takahasi et al., 2001), Congo Angola basin (Charlou et al., 2004), and the Sea of Okhotsk (Ginsburg et al., 1993) show that most of the gas forming gas hydrate has a microbial origin.

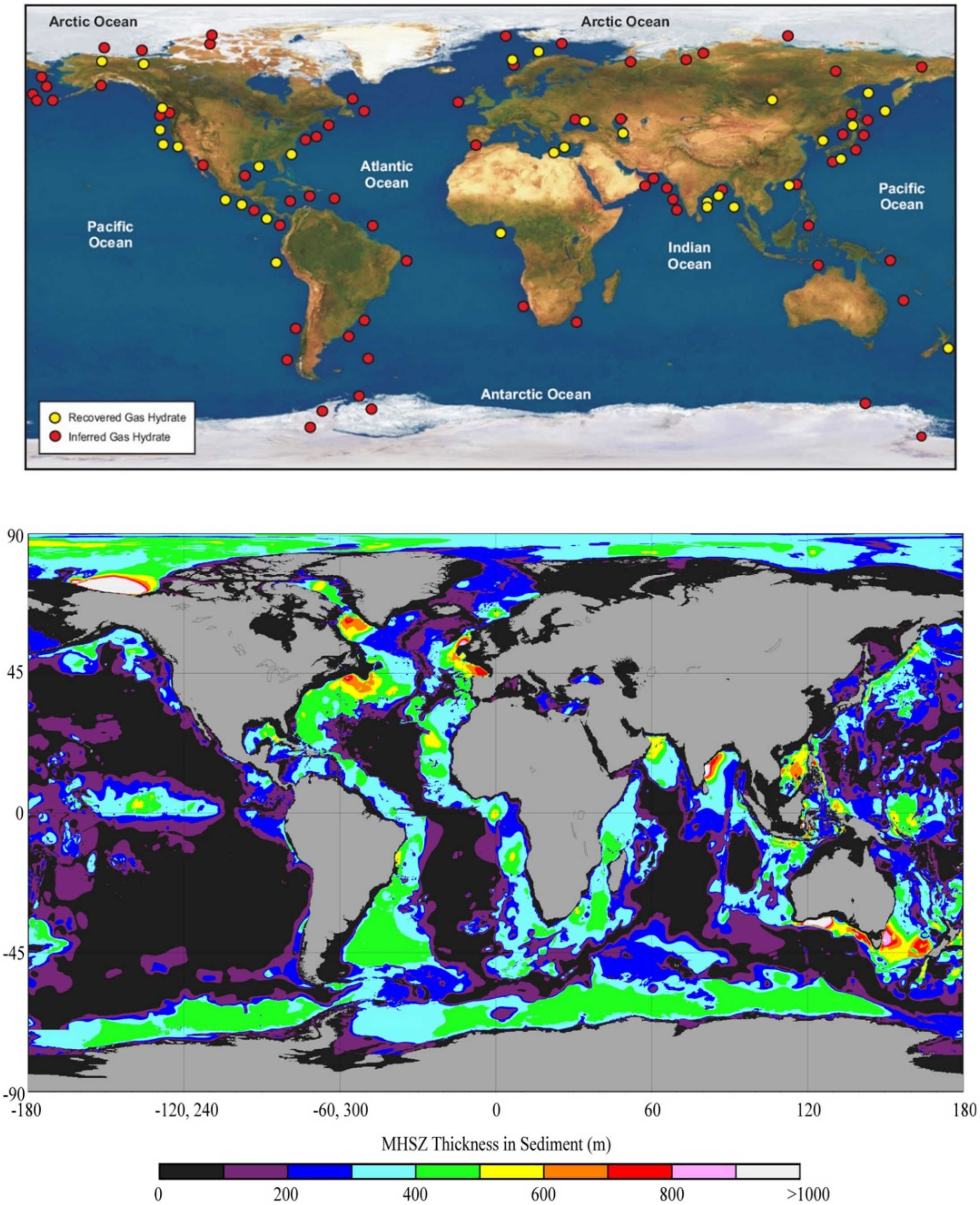

Figure 1-1. *(a) Distribution of known methane hydrate accumulations courtesy of Council of Canadian Academies (2008), based on data from Kvenvolden and Rogers (2005). (b) Estimated global methane hydrate stability zone thickness (MHSZ) in the seafloor sediments (Krey et al., 2009).*

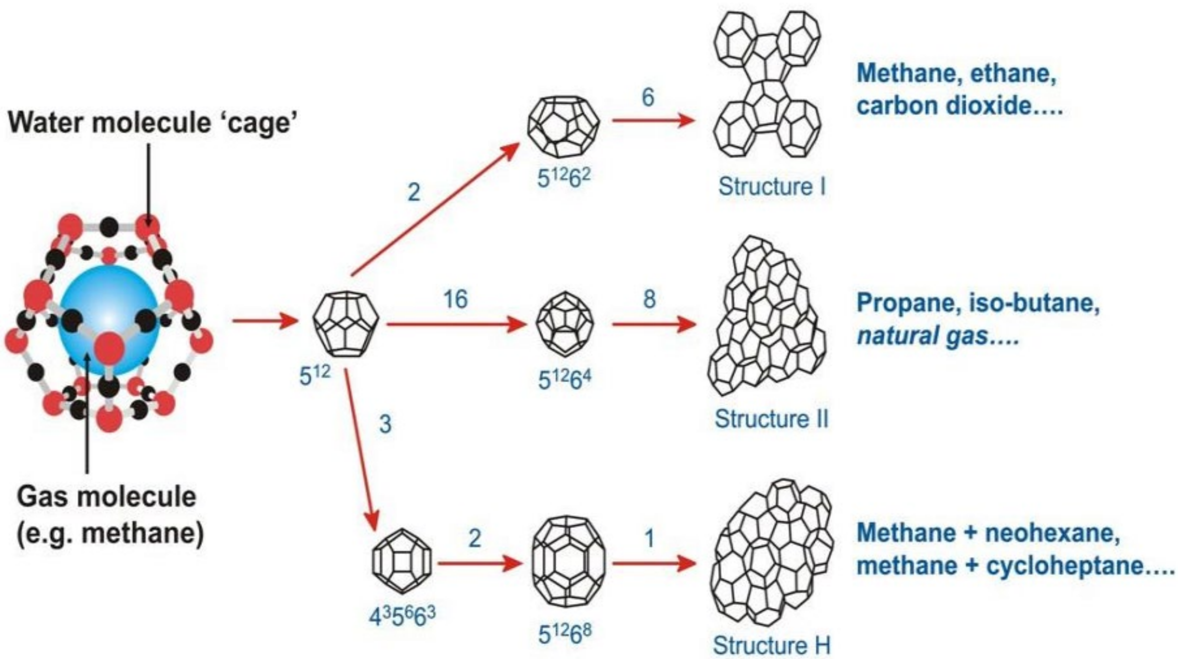

Figure 1-2. *Gas-hydrate crystal structures. The five types of water cages that make up the gas-hydrate structures are the pentagonal dodecahedron (5^{12}), the tetrakaidecahedron ($5^{12}6^{2}$), the hexakaidecahedron ($5^{12}6^{4}$), the irregular dodecahedron ($4^{3}5^{6}6^{3}$), and the icosahedrons ($5^{12}6^{8}$). The three structure types of gas hydrate are shown: structure I, II and H (Collett et al., 2009).*

Gas hydrate stability

Gas hydrate formation in marine sediments requires natural gas and water existing at very specific pressure and temperature (Kvenvolden, 1988). The stability of hydrates is affected by the composition of gas and ionic impurities in the water (Kvenvolden, 1998). Understanding of precise gas composition is important in gas hydrate stability modelling, as a variation in gas composition moderate (5 - 10%) can shift the modelled GHSZ by tens to-hundreds of meters (Sloan and Koh, 2008). Important parameters influencing hydrate formation include gas composition, bottom water temperature, geothermal gradient, and pore water salinity (Coffin et al., 2007). The pressure and temperature conditions required for pure methane hydrate stability in marine sediments in a normal seawater salinity environment are illustrated in Figure 1-3. Gas hydrates are stable in water depths greater than 200 to 600 meters depending on the gas composition and seafloor temperatures (Milkov and Sassen, 2002). The depths of favorable pressure and temperature conditions is known as the "gas hydrate stability zone" (GHSZ). The thickness of GHSZ vary significantly across the globe, as illustrated in Figure 1-3.

High saturations of methane hydrate in marine sediments are discovered within continental margins, where the high concentrations of organic carbon in these settings and fast sedimentation rates required to accumulate the organic carbon to form a source rock (Muller and Suess, 1979). The density of gas hydrates vary from 0.8 to 1.2 gm/cm3 depending on the composition of gas that was used to form the hydrate (Makogon et al., 2007) and the texture of the hydrate.

Gas hydrates would naturally dissociate when they exceed the limit of the temperature of stability of gas hydrates because of time and burial, which are mainly controlled in a specific geological setting. The thickness of the GHSZ tends to be constant for a given water depth because the geothermal is relatively uniform over a broad region beneath the seafloor for a certain period of time (Schulz and Zabel, 2006). However, a variation in the water depth would modify the pressure conditions on marine sediments, significantly affecting the stability of gas hydrate deposits. As most of continental margins present the suitable pressure and temperature conditions for gas hydrate formation, the presence of sufficient gas molecules seems to be the main limiting factor affecting gas hydrate distribution (Schulz and Zabel, 2006).

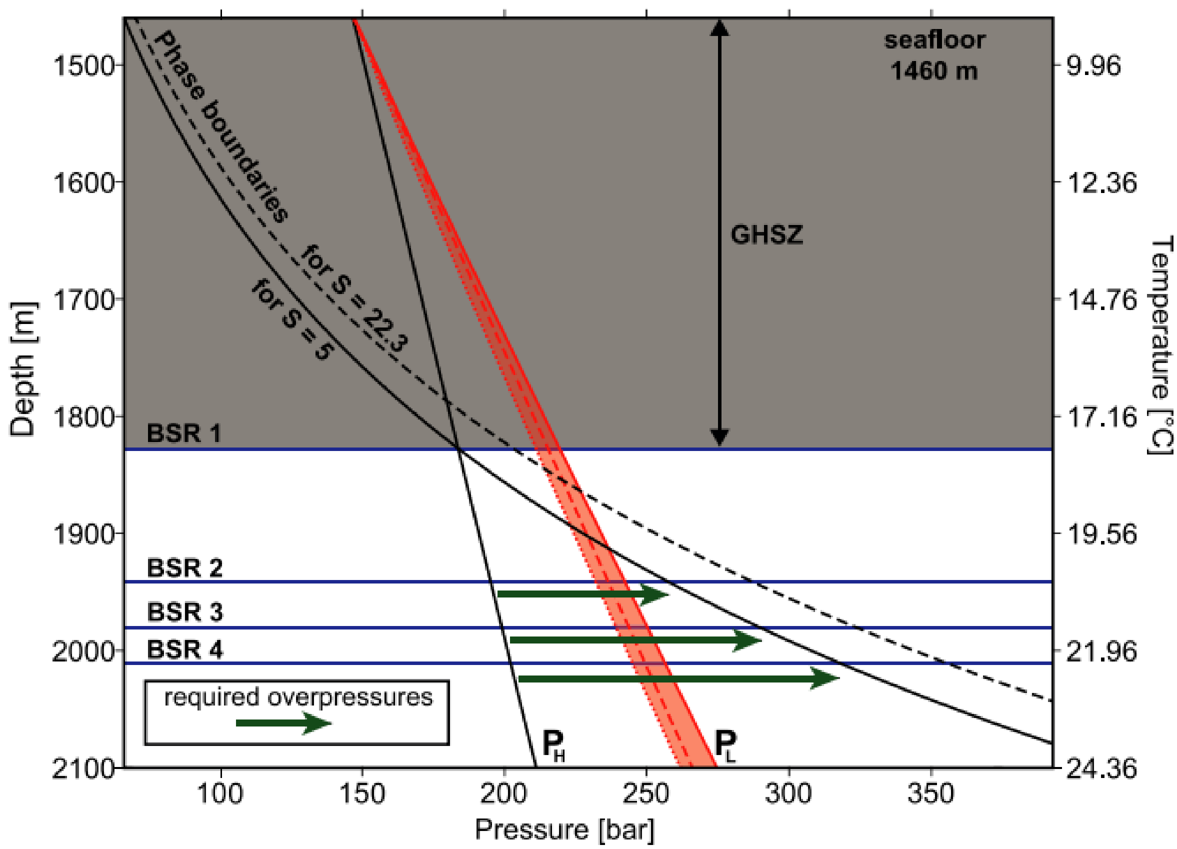

Figure 1-3. *Stability diagram of gas hydrates in the deep sea (Zander et al., 2017). The stability temperature for clathrate increases with pressure/depth. The intersections of the geotherm and the temperature of gas hydrate stability define the depth of the base of the gas hydrate stability zone (GHSZ).*

The important of fluid-flow systems in the continental margin

Fluid flow refers to the fluid migration from the subsurface and through the seafloor into the ocean and atmosphere. Focused fluid flow features have been investigated on continental margins worldwide (Rajan et al., 2012a; Vadakkepuliyambatta et al., 2013). Fluid flow can be induced by varying processes, including rapid sediment loading (Dugan and Flemings, 2000), faulting (Cartwright et al., 2007), uplift and erosion (Xu et al., 2016), dissociation of gas hydrates (Mienert et al., 2005), hydrocarbon generation and leakage from deep and shallow source rocks (Vadakkepuliyambatta et al., 2013) and earthquakes (Fischer et al., 2013). The density and pressure gradients between sedimentary layers serve a major role in rate of fluid migration. Fluid flow rate is controlled by the permeability of the medium, the pressure gradient, and fluid viscosity (Darcy, 1856). Low-permeability formations can restrain flow of fluids resulting in excess pore pressure generation. Methane gas generated through organic matter reactions in marine sediments forms the most common hydrocarbon associated with fluid flow (Schoell, 1988). Depending on the subsurface geology, source of fluids, and differential pressure, upward rising fluids produce various subsurface features. Fluids were delivered to the shallow subsurface and are difficult to characterize due to lack of direct observations and their transient nature (Talukder, 2012).

Fluid migration through sedimentary formations within heterogeneous distribution of small gas accumulations lead to attenuation of seismic energy (Taladay et al., 2017). These zones of low-amplitude seismic signals can appear on the seismic data in different shapes based on the nature of their formation. Attenuated seismic features are observed with mud mobilizations (Løseth et al., 2003), gas chimneys (Hustoft et al., 2010) and faults. Due to the large attenuation of seismic signals inside a chimney, therefore delineating the source of fluids is commonly difficult. Leaking faults are usually associated with high-amplitude acoustic anomalies, which indicate the presence of gas accumulations.

The important of gas hydrate research

There have been considerable and increasing interests in gas hydrate worldwide owing to its important role on climate change and potential future energy resource. The dynamic behavior of methane hydrate in subsurface marine environments has also been a major focus of studies related to rapid climate change and geohazards (Burwicz et al., 2011; Mienert et al., 2005). The influence of hydrate on the global carbon cycle, and on the carbon stored in hydrate reservoirs for methane production, is a new and evolving field of research (Qorbani et al., 2017). Understating how the structural effects are controlling the distribution of hydrate and free gas in the sediment will enhance our knowledge of the system as a whole, and may provide insight into carbon exchange and storage in the deep ocean.

The need for energy has generated a strong international expectation in the exploration for natural gas hydrates. Gas hydrate exploration expeditions have been developed recently in Canada, China, India, Japan, Taiwan and the United States. Sophisticated technologies and global economy will determine the future production of gas from gas hydrate deposits (Hester and Brewer, 2009). The future of gas hydrate exploitation serving as an energy resource depends on important factors including the geological studies to identify concentration sites and settings where methane can be effectively extracted from gas hydrate and to determine the most efficient means of dissociating gas hydrates in situ and extracting gas safely.

Methane is a potent greenhouse gas and would act to warm the Earth, causing to continue dissociation of gas hydrate. The Intergovernmental Panel on Climate Change (IPCC) declares that methane is about 25 times more potent than carbon dioxide as a greenhouse gas over a century (Stocker et al, 2013). Marine CO_2 sequestration was conducted at an experimental stage, focusing on transport limitations and exchange time rates (Zhou et al., 2008), CO_2 solubility (Yang et al., 2000), CO_2-hydrate formation kinetics, CO_2-hydrate stability (Circone et al., 2003) and numerical modelling for spatial characterization of gas hydrate deposits (Janicki et al., 2017).

Classification of gas hydrate deposits

Hydrate deposits have been divided into four depended on their reservoir conditions (Li et al., 2010) as follows:

Class 1: This class of hydrate accumulation consists of two zones: a hydrate bearing interval and underlying two-phase fluid zone containing free gas and water (Figure 1-4). Hydrate bearing intervals are characterized by low effective permeability due to the very high hydrate saturation in their pore space. The bottom of the hydrate stability zone often coincides with the bottom of the hydrate interval. From a gas production point of view, this type of hydrate deposits are most desirable for exploitation due to the hydrate thermodynamic proximity to the hydration equilibrium. Therefore, it requires only small changes in pressure and temperature to induce dissociation process.

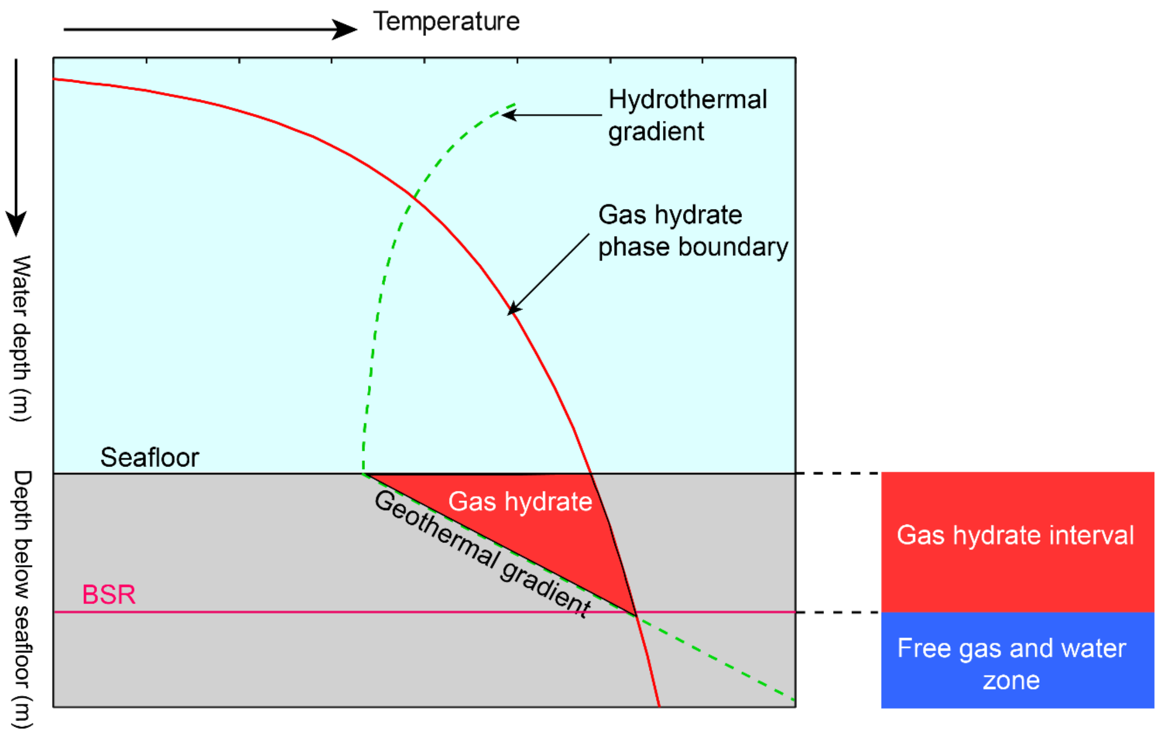

Figure 1-4. *Class 1 gas hydrate accumulation showing the gas hydrate interval coinciding with BSR and the underlying free gas zone. (Modified from Silpngarmlert, 2007).*

Class 2 hydrate deposit consists of two zones: a hydrate bearing interval, and an underlying water interval with no free gas. In this class of hydrate accumulation, the bottom of the hydrate interval does not necessarily indicate the bottom of the hydrate stable region, as the entire hydrate interval may fall within the hydrate stable region (Figure 1-5). Numerical gas generation research (Moridis and Collett, 2003) revealed that relative permeability conditions resulting from the appearance of the gas phase in the previous water-filled zones could easily interfere with the favorable decompression regime. In terms of gas recovery, depressurization may seem to be more effective because of the very incompressible nature of water, resulting in strong pressure disturbances being dissipated over a wide range of hydrate-water interfaces.

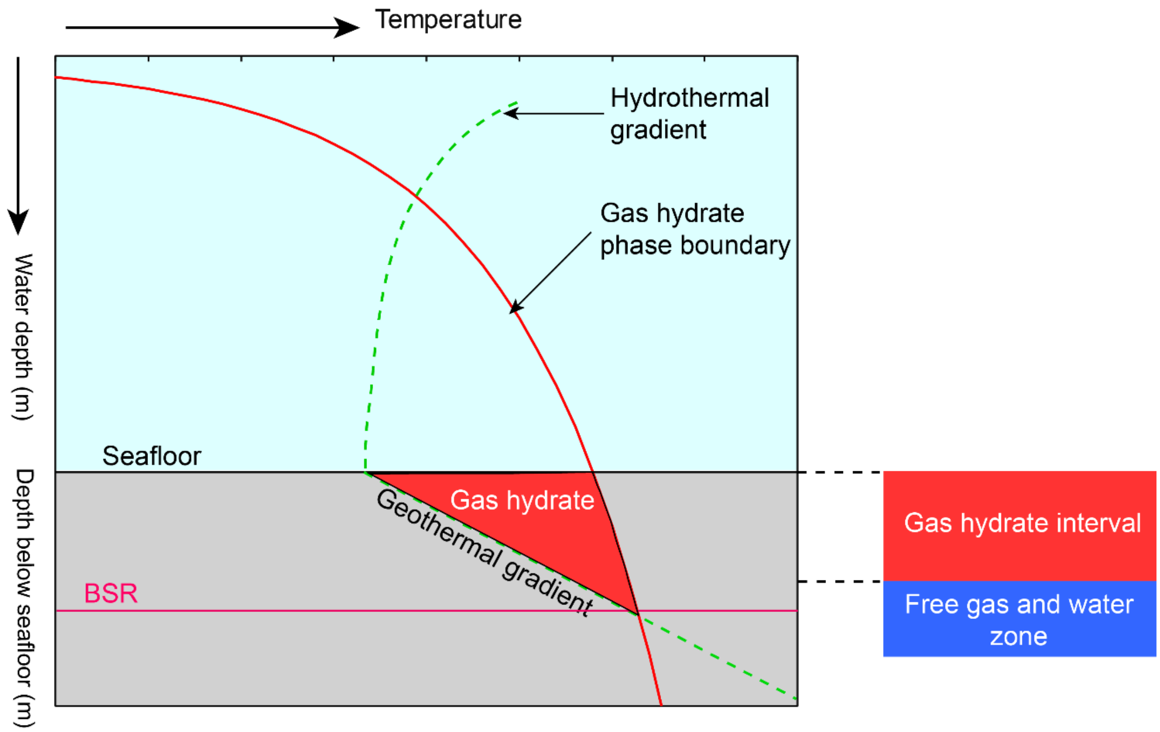

Figure 1-5. *Class 2 gas hydrate accumulation showing the gas hydrate interval not coinciding with BSR, and the underlying water zone. (Modified from Silpngarmlert, 2007).*

Class 3 has only one area in comparison to class 1 and 2, hydrate interval with no underlying gas zone (Li and Moridis, 2010). The lower part of the interval does not necessarily mark the bottom of the hydrate stability zone, while the entire hydrate interval can fall into the hydrate stability zone (Figure 1-6). Gas hydrate reserve generally have high hydrate saturation, reducing effective permeability of gas and water, especially in reservoirs with low permeability. This makes the depressurization caused by the recovery of gas. For this type of hydrate reserve, thermal stimulation seems to be the technique of proper production.

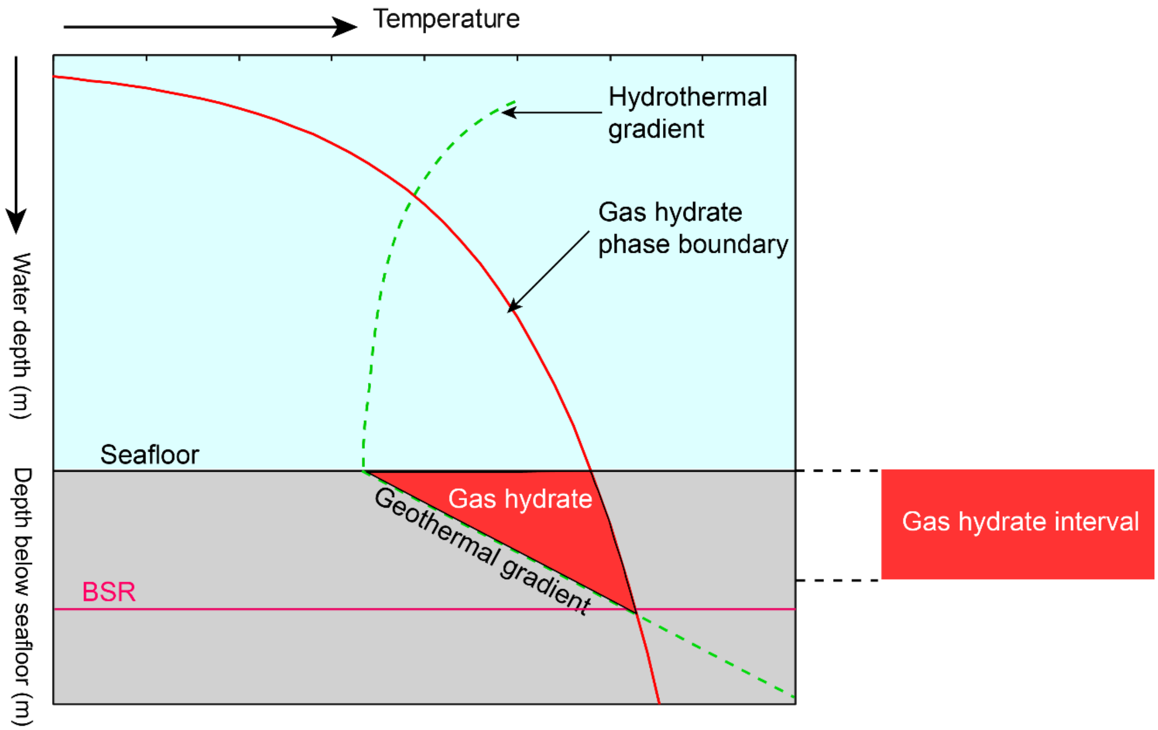

Figure 1-6. *Class 3 hydrate accumulation showing the methane hydrate interval not coinciding with BSR, with no underlying water and/or free gas zone. (Modified from Silpngarmlert, 2007).*

Class 4: Class 4 accumulations are significantly different from the others due to their low saturation (Moridis and Sloan, 2007). They occur in submarine hydrate deposits and are considered not a promising target for exploitation.

Seismic evidence for characterizing gas hydrate deposits

Since the evaluation of gas hydrate reserves is considered to be highly uncertain, therefore, an efficient technology to detect and characterize gas hydrate deposits is required. By using seismic reflection techniques, the presence of gas hydrate in offshore continental margin has been detected (Baba and Yamada, 2004; Jia et al., 2016; Chhun et al., 2018).

Natural gas hydrate accumulations have commonly been inferred on seismic reflection profiles from the presence of a bottom-simulating reflector (BSR) at the base of the mostly pressure-temperature-controlled gas hydrate stability zone. The BSR can be easily recognized because it is parallel to the seafloor and has strong inverse polarity reflections that cross cut sedimentary layers and represent the strong impedance contrast between the base of the hydrate and the underlying sediment or free gas zone (Hyndman and Spence, 1992). Gas hydrate occurrence and the existence of a BSR depend on the local lithology and the structural setting (Reidel et al., 2006a), the amount of water, and its salinity (Milkov et al., 2004b). The structural patterns in a particular depositional setting affect influence the amount of gas hydrate and the associated free-gas accumulations (Bünz et al., 2005). Gas hydrate deposits are structurally controlled, associated with fluid-flow paths varying with depositional settings (Hustoft et al., 2007) (Figure 1-7).

Zones of high amplitude reflections occurring above the BSR akin to the Upper BSRs observed in seismic data were found in the Nankai prism (Inamori ert al., 2004), which are well correspond to highly concentrated gas hydrates zones in comparison to core analyses (Boswell et al., 2014). Moreover, high amplitude reflections suggesting gas-charged sediments are common beneath the BSR (Chhun et al., 2018). Other seismic indicators of gas-charged fluids include flat spots, and dim spots, which are known as direct hydrocarbon indicators, and are therefore crucial features in defining of hydrocarbons in marine sediments (Spence et al., 2010). Seismic blanking within the gas hydrate stability zone is characteristic of the reduction of pore space due to the effect of gas hydrate saturation (Boswell and Collett, 2011).

Analyses of the seismic velocities and amplitude behavior at the BSR provide an efficient way of characterizing the distribution of gas hydrates within marine sediments (Hyndman and Spence, 1992; Korenaga et al., 1997). The flow of gas toward and through the gas hydrate stability zone is a fundamental process that can lead to the deposition of concentrated gas hydrate deposits (Milkov and Sassen, 2001), seafloor methane seepage (Greinert et al., 2010), and also potentially to the generation of excess fluid pressure that can

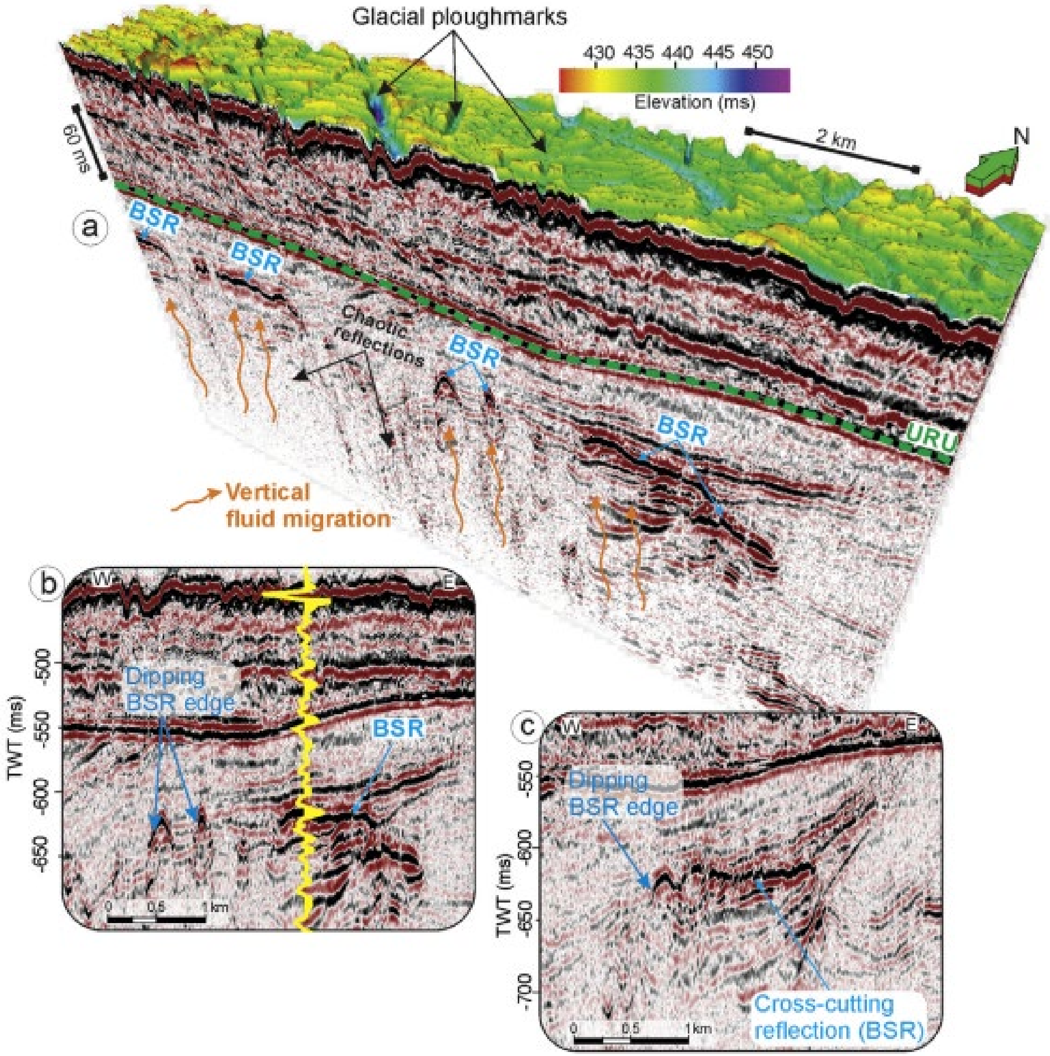

Figure 1-7. *(a) High-resolution 3D seismic showing high-amplitudes, reverse polarity reflector, interpreted as BSRs, and chaotic seismic reflection below. (b) and (c) Zoomed in views of BSR from 3D seismic profiles exhibit various shape of BSRs. A seismic trace (yellow) show the polarity reversal at the BSR (Vadakkepuliyambatta et al., 2015).*

destabilize near-seafloor sediments (Crutchley et al., 2010b). Additionally, gas hydrate can be deposited in the areas, where BSRs are not observed (Riedel et al. 2006) but fluid flow is active. Therefore, characterizing regions where such focused flow reflecting temperature variation takes place are essential for our general understanding of these issues surrounding the gas hydrate system using high quality three-dimensional (3D) seismic data.

To characterize the physical properties from 3D seismic data (e.g., seismic velocity), rock physics models are commonly used. Rock physics model combined with most of the geophysical measurements and mathematical tools helps to account for the uncertainty in the data (Mavko et al., 1998; Chhun et al., 2018; Jia et al., 2016). The rock physics section is applied to distinguish rock properties, understand reservoir heterogeneity, generate a representative rock physics model, and establish relationships between physical rock properties and seismic elastic properties. Rock physics model addresses the relationships between rock properties, such as porosity, lithology, fluid saturations, velocities, and geological deposition environment. The model can be a simple theoretical relation, such as granular media models or inclusion models (Mavko et al., 1998) that fits well-log observations, used in quantitative seismic interpretation and reservoir characterization.

1-2 Objective

This study is aimed at advancing the use of 3D seismic data to improve the geological understanding of exploration targets, and to use the rock physics model for characterizing the physical properties of reservoir rocks. 1) The first goal is to better understand controlling mechanisms for the occurrence and development of focused fluid flow features (i.e. fluid flow through faults and chimneys) and their relationship to gas hydrate-related bottom-simulating reflector (BSR) in Sanriku-Oki forearc basin in the complex tectonic structure. 2) The second goal is to estimate crack aspect ratio (pore geometry) and grain elastic moduli of hydrothermal deposits and basalts.

To accomplish these tasks, first, automated velocity analysis was applied (Fomel, 2009) to pre-stack seismic data to obtain seismic profiles and high-resolution velocity models, and then fluid flux was estimated (i.e. heat flow) using depth of BSR from the obtained high-resolution velocity results. Secondly, the grid-search inversion method based on differential effective medium (DEM) theory was proposed to velocity-porosity relationship to obtain elastic moduli and pore aspect ratios. I could assess the relationships between pore geometry and grain elastic moduli and characterize reservoir quality in term of physical (i.e. grain elastic moduli) and hydraulic properties using permeability models (Sarout, 2012).

1-3 Reservoir characterization using high-resolution seismic data

Reservoir characterization plays an essential role in the primary exploration and development. It contributes to the prediction of reservoir properties as well as to the economic potential of the field. In general, a reservoir study can be categorized into different scales such as molecular scale, pore scale, core scale, and field scale. Predicting a reservoir characteristic of a field is difficult because of the data resolution challenges. As real geological structures within the earth vary in a three-dimensionally, therefore, it is reasonable that 3D seismic data should provide a more accurate and informative image of the subsurface. 3D seismic surveys are very useful in many exploration expeditions due to the high resolution of structures and stratigraphy as well as rock properties that can be delineated relied on seismic attributes properties. High-resolution 3D seismic data provide insight into the presence of hydrocarbon (Figure 1-8), sedimentary facies, migration pathways, and fluid movement used in discussing and evaluating reservoir potential without depending on drilling data.

The seismic reflection method became commercially viable as an exploration technique in the hydrocarbon explorations. Seismic reservoir characterization and prospect evaluation are based on seismic reservoir properties such as acoustic impedance (Eng and Tsuji, 2019), elastic moduli, and *Vp/Vs* ratio (Tsuji et al., 2011). Other studies have characterized gas hydrate and free gas, and estimated hydrate saturation using seismic data integrated with rock physics model (Chhun et al., 2018; Crutchley et al., 2015). Therefore, seismic reflection method is an effective technique for gas hydrate exploration like other petroleum resources. Quantification of gas hydrate and free gas from such anomalous seismic velocities based on certain rock properties can provide valuable pre-drill information for site selection to conduct further research on both exploration and exploitation.

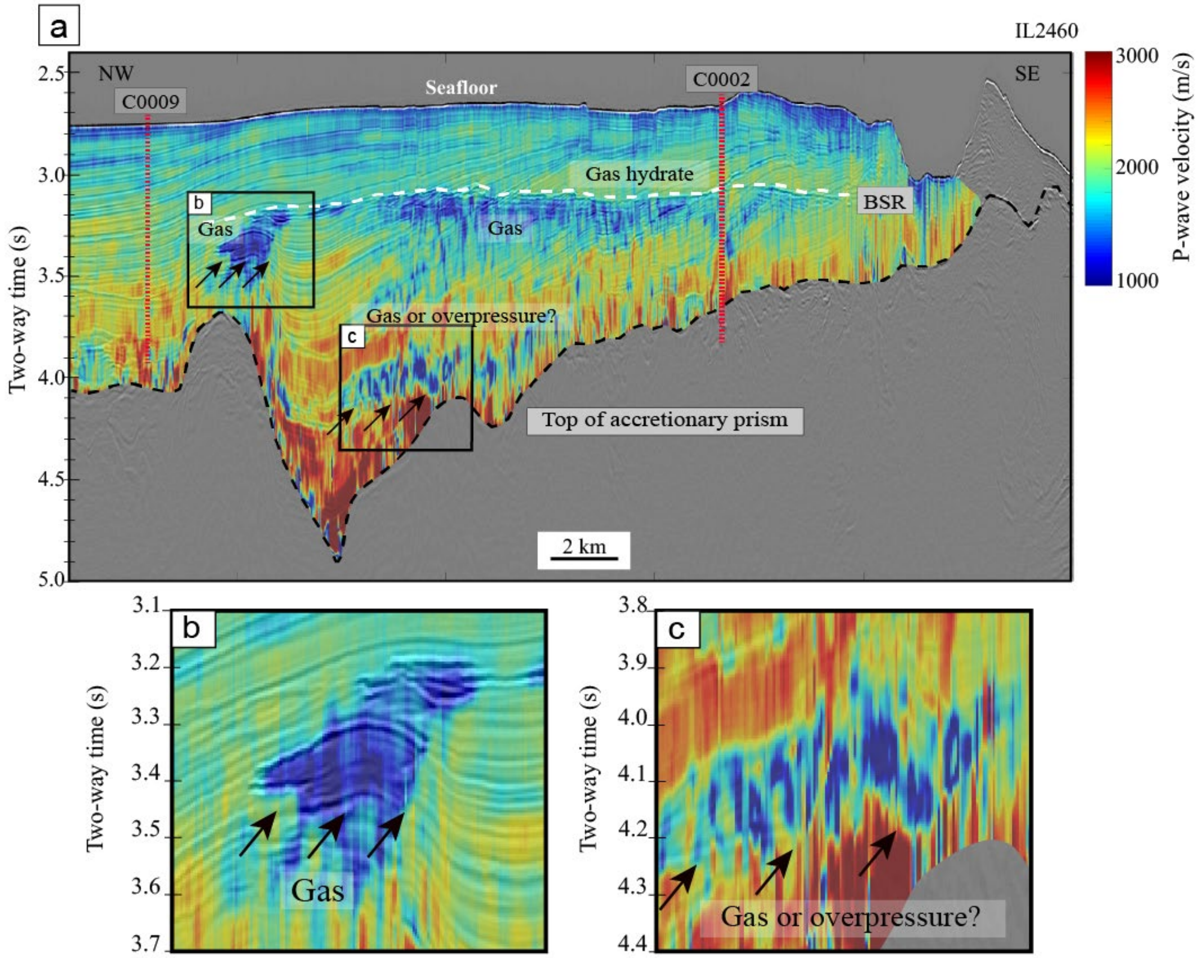

Figure 1-8. *(a) seismic velocity profile showing gas hydrate (high velocity above BSR) and gas accumulation (low velocity beneath BSR). The gas accumulation zones are clearly imaged on the enlarged profile of panels (b) and (c). Black arrows illustrate the base of gas reservoirs (chhun et al., 2018).*

In chapter 2, I present seismic evidence for the existence of gas hydrates and free gas of Sanriku-Oki forearc basin. I applied automated velocity analysis to pre-stack 3D seismic data to obtain high-resolution P-wave velocity to delineate the distribution of gas hydrate, and then I estimated heat flow using depth of BSRs. These seismic data shed new lights on the links among high heat flow (i.e. fluid flux) and subsurface gas hydrate, origin of gas source and structural styles controlling the formation and accumulation of gas hydrate in the Sanriku-Oki forearc basin.

1-4 Rock physics model

The effective physical properties of heterogeneous rocks are often needed in Earth sciences, especially elastic properties in laboratory-scale rock physics and field-scale geophysics. Both elastic properties and hydraulic properties of rocks are controlled by heterogeneities in rocks constituting the Earth's crust, which may arise from the variable mineral composition, the presence of pores/cracks (Figure 1-9; Jiang et al., 2018) and the nature of the saturating fluid. Indeed, the physical model can be any rock physics model including velocity-saturation (Mavko and Mukerji, 1998), velocity-porosity (Doyen, 1988), velocity-pressure (Doyen, 2007), amplitudes-velocities (Buland and More, 2003), and porosity-permeability, etc.

Differential effective medium (DEM) theory, one of the rock physics approach, is applied to the problem of estimating the physical properties of elastic media with penny-shaped cracks, filled either with gas or liquid (Marko et al., 1998). It is known that such a model captures many of the essential physical features of fluid-saturated or partially saturated rocks. The effect of crack/pore on the seismic velocities of rocks and composites has been studied by many researchers using velocity-pressure relationship, as crack is closed when increasing pressure (Wilkens et al., 1991; Berryman and Berge, 1996). In general, these studies show that when porosity is held constant, thinner voids

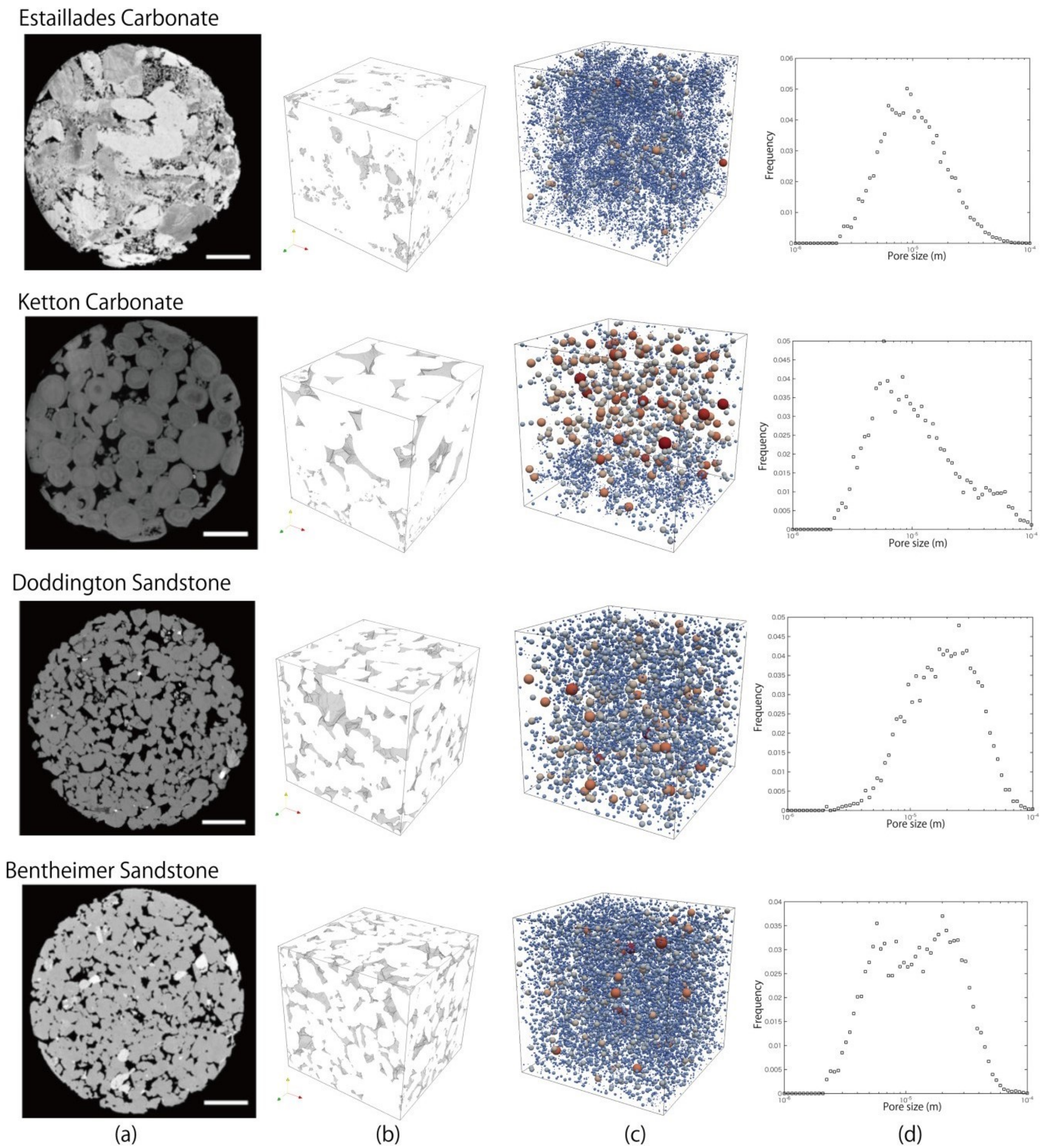

Figure 1-9. *CT slice image of different rocks (Alyafei et al., 2016); (b) 3D rock model after segmentation; (c) distributions of spheres showing pore bodies; and (d) pore-size distribution data (Jiang et al., 2018).*

(cracks) lower the seismic velocities significantly more than spherical pores, or vesicles. This effect is caused by the more substantial lowering of both the bulk and shear moduli of the rock (the effective moduli) when cracks are present. Hence, the shapes of the voids and cracks that populate rocks have a substantial influence on their seismic velocities. The pore aspect ratio is defined as the ratio of the short axis length over the long axis length of the ellipsoid (Figure 1-10).

In chapter 3, I applied grid-search inversion method to estimate average pore geometry and grain elastic moduli from porosity-velocity relationship acquired from hydrothermal ore deposits. I could use the information derived from my analyses for reservoir characterization using permeability models based on crack aspect ratios (Sarout, 2012; Figure 1-11).

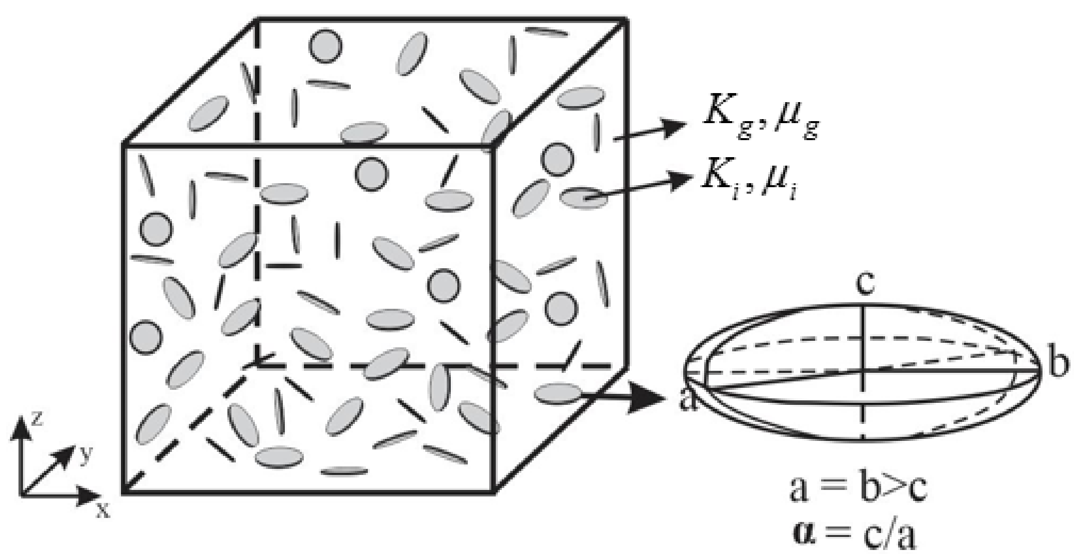

Figure 1-10. *3D schematic image showing distribution of random pores with constant crack aspect ratio (α) within rock sample.* K_g *and* μ_g *represent elastic moduli of grain.* K_i *and* μ_i *represent elastic moduli of inclusion within pores.*

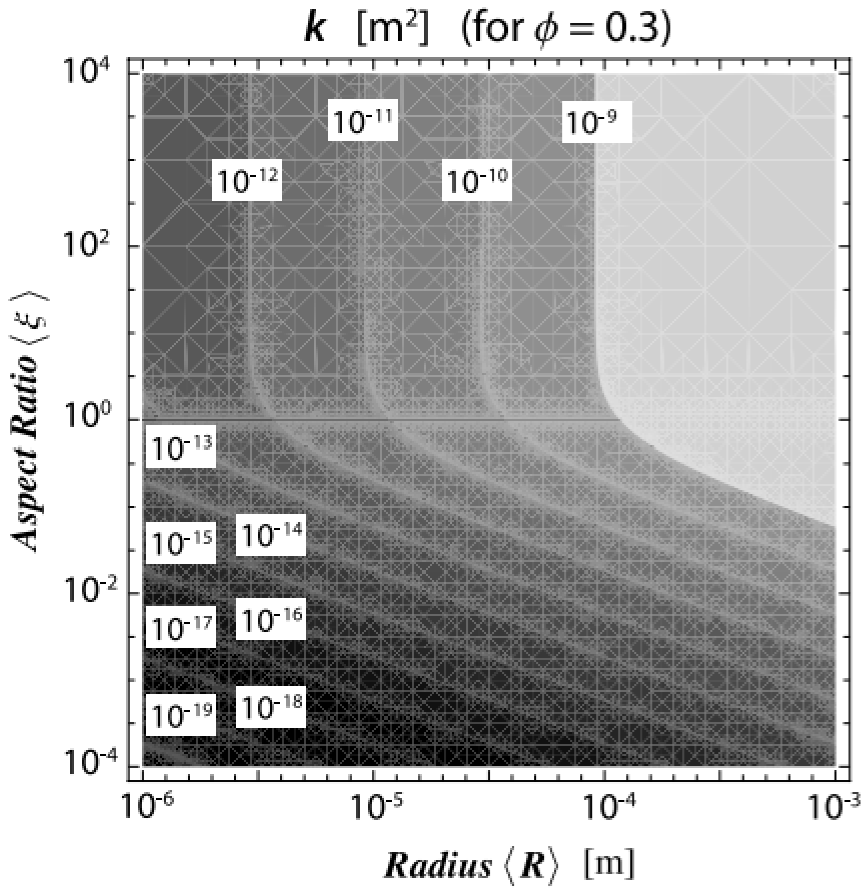

Figure 1-11. *Predictions of the new permeability model in terms of cavities average aspect ratio ξ and average radius R for a porosity Φ (Sarout, 2012).*

1-5 Chapter organization and contributions

This thesis focuses on the application of high-resolution seismic velocity analysis and rock physics model for reservoir characterization. There are four chapters in this thesis, including this introduction chapter. The main methodologies, interpretation, discussion and conclusion are described in Chapters 2 and 3. The methodologies described in Chapter 2 include automated velocity analysis and heat flow estimation. In Chapter 3, a grid-search inversion based on differential effective medium (DEM) theory was applied to P-wave velocity-porosity relationship to obtain crack aspect ratio and gain elastic moduli of core samples acquired at hydrothermal deposits.

Chapter 2 demonstrates the application of automated velocity analysis to 3D seismic data to characterize the gas hydrate and free gas distribution in the Sanriku-Oki forearc basin. Bottom simulating reflectors (BSRs), known as the base between gas hydrate and free gas, were identified and mapped. Furthermore, seismic attributes, high-resolution and BSR-derived heat flow were obtained to delineate the spatial distribution of gas hydrate and free gas. Faults, slumps and chimneys were observed in seismic profiles, providing migration pathways allowing methane to move upward to gas hydrate zones. This chapter has been submitted to G-cubed journal (under review), and partially presented in International Symposium on Earth Science and Technology 2017 and The Society of Exploration Geophysicists of Japan 2018.

Chapter 3 presents a grid-search inversion based on differential effective medium (DEM) theory (a method of rock physics model) applied to P-wave velocity - porosity relationship of core samples acquired from hydrothermal ore deposit. The model is efficiently applied to estimate the average crack aspect ratio and grain elastic moduli of core samples for core samples measured at the atmospheric pressure. I found that samples measured at atmospheric pressure and under higher effective pressure show the similar relationship between velocity and porosity and have similar average crack aspect ratios. Some part of this work was presented at the International Symposium on Earth Science and Technology 2017, and The 10th AUN/SEED-Net Regional Conference on Geological and Geo-Resource Engineering. This chapter was published at Exploration Geophysics (Kret et al., 2019).

Chapter 4 presents the conclusions and prospects for this research work in the future on rock physics model and seismic data for more rigorous reservoir characterization.

1-6 References

Alyafei, N., T. J. Mckay, and Solling, T. I. 2016. Characterization of petrophysical properties using pore-network and lattice-Boltzmann modelling: Choice of method and image sub-volume size. Journal of Petroleum Science and Engineering, 145, 256–265. https://doi.org/10.1016/ j.petrol.2016.05.021

Baba, K., Y, Yamada. 2004. BSRs and associated reflections as an indicator of gas hydrate and free gas accumulation: an example of accretionary prism and forearc basin system along the Nankai Trough, off central Japan. Resour. Geol. 54, 11 –24. http:// dx.doi.org/10.1111/j.17513928.2004.tb00183.x.

Berryman, J.G., and P. A. Berge. 1996. Critique of two explicit schemes for estimating elastic properties of multiphase composites. *Mech. Mater.*, 22:149–164.

Boswell, R., and T.S. Collett. 2011. Current perspectives on gas hydrate resources. *Energy Environ. Sci. 4*, 1206–1215.

Boswell, R., T. Saeki, C. Shipp, M. Frye, B. Shedd, T. Collett, D. Shelander, D. McConnel. 2014. Prospecting for Gas Hydrate Resources. Department of Energy, FITI Methane Hydrate Newsletter. *Interpreation, 14*, 9–13.

Buland, A. and H. More. 2003. Bayesian linearized AVO inversion: Geophysics, 68, 185 – 198, doi: 10.1190/1.1543206.

Bünz, S., J. Mienert, M. Vanneste, and K. Andreassen. 2005. Gas hydrates at the Storegga Slide: Constraints from an analysis of multicomponent, wide-angle seismic data: *Geophysics*, 70, no. 5, B19–B34.

Burwicz, E.B., L.H. Rüpke, and K. Wallman. 2011. Estimation of the global amount of submarine gas hydrates formed vial microbial methane formation based on numerical reaction-transport modeling and a novel parameterization of Holocene sedimentation. *Geochim. Cosmochim. Acta*, *75*, 4562–4576.

Cartwright, J., M. Huuse, A. Aplin. 2007. Seal bypass systems. *Aapg Bulletin*, 91, 1141 - 1166.

Charlou, J.L., J.P. Donval, Y. Bouquet, H. Ondreas, J. Knoery, P. Cochonat, D. Levaché, Y. Poirier, P. Jean-Baptiste, E. Fourré, B. Chazallon, and the ZAIROV Leg 2 Scientific Party. 2004. Physical and chemical characterization of gas hydrates and associated methane plumes in the Congo-Angola Basin. *Chemical Geology*, 205, 405-425.

Chhun, C., A. Kioka., J. Jia, and T. Tsuji. 2018. Characterization of hydrate and gas reservoirs in plate convergent margin by applying rock physics to high-resolution seismic velocity model. Marine and Petroleum Geology, 92, 719–732. https://doi.org/10.1016/j.marpetgeo.2017.12.002.

Circone, S., L.A. Stern, S.H. Kirby, W.B. Durham, B.C. Chakoumakos, C.J. Rawn, et al. 2003. CO_2 hydrate: synthesis, composition, structure dissociation behavior, and a comparison to structure I CH4 hydrate. *Journal of Physical Chemistry* B 107 (23), 5529-5539.

Coffin, R., Pohlman, J., Gardner, J., Downer, R., Wood, W., Hamdan, L., Walker, S., Plummer, R., Gettrust, J., Diaz, J., 2007. Methane hydrate exploration on the mid Chilean coast: a geochemical and geophysical survey. *J. Pet. Sci. Eng.* 56, 32-41.

Collett, T. S., A. H. Johnson, C. C. Knapp, and R. Boswell. 2009. Natural GasHydrates: A Review,eds., Natural gas hydrates-Energy resource potential and associatedgeologic hazards: AAPG Memoir 89, p. 146–219.

Council of Canadian Academies 2008 *Energy From Gas Hydrates: Assessing the Opportunities and Challenges for Canada.*

Crutchley, G. J., D. R. A. Fraser., I. A. Pecher., A. R. Gorman., G. Maslen, and S. A., Henrys. 2015. Gas migration into gas hydrate-bearing sediments on the southern Hikurangi margin of New Zealand. *Journal of Geophysical Research: Solid Earth*, *120*(2), 725-743.

Crutchley, G. J., S. Geiger, I. A. Pecher, A. R. Gorman, H. Zhu, and S. A. Henrys. 2010b. The potential influence of shallow gas and gas hydrates on sea floor erosion of Rock Garden, an uplifted ridge off shore of New Zealand, Geo–Mar. Lett., 30(3–4), 283–303.

Doyen, P. 2007. Seismic reservoir characterization: EAGE.

Doyen, P. 1988. Porosity from seismic data: A geostatistical approach: Geophysics, 53, 1263 –1275, doi: 10.1190/1.1442404.

Dugan, B., and P.B. Flemings. 2000. Overpressure and Fluid Flow in the New Jersey Continental Slope: Implications for Slope Failure and Cold Seeps. *Science*, 289, 288-291.

Eng, C., and T. Tsuji. 2019. Influence of faults and slumping on hydrocarbon migration inferred from 3D seismic attributes: Sanriku-Oki forearc basin, northeast Japan. *Marine and Petroleum Geology*, *99*, 175-189. https://doi.org/10.1016/j.marpetgeo.2018.10.013.

Englezos, P and J. D. Lee. 2005. Gas hydrates: A cleaner source of energy and opportunity for innovative technologies. *Korean Journal of Chemical Engineering*, 22(5), 671-681.

Darcy, H. 1856. Les Fontaines Publiques de la Ville de Dijon, Dalmont, Paris.

Fischer, D., J.M. Mogollón, M. Strasser, T. Pape, G. Bohrmann, N. Fekete, V. Spiess, S. Kasten. 2013. Subduction zone earthquake as potential trigger of submarine hydrocarbon seepage. *Nature Geoscience,* 6, 647- 651.

Fomel, S. 2009. Velocity analysis using AB semblance. *Geophysical Prospecting*. 57 (3), 311–321. http://dx.doi.org/10.1111/j.1365-2478.2008.00741.x.

Ginsburg, G.D., Soloviev, V.A., Cranston, R.E., Lorenson, T.D., and Kvenvolden, K.A., 1993. Gas hydrates from the continental slope, offshore Sakhalin Island, Okhotsk Sea. *Geo Marine Letters*, 13, 41-48.

Greinert, J., K. B. Lewis, J. Bialas, I. Pecher, A. A. Rowden, D. Bowden, M. De Batist, and P. Linke. 2010. Methane seepage along the Hikurangi Margin, New Zealand: Overview of studies in 2006 and 2007 and new evidence from visual, bathymetric and hydroacoustic investigations, Mar. Geol., 272, 6–25.

Hester, K.C., and P.G. Brewer. 2009. Clathrate hydrates in Nature. *Annual Review of Marine Science,* 1, 303-327.

Hyndman, R. D., and G. D. Spence. 1992. A seismic study of methane hydrate marine bottom simulating reflectors: Journal of Geophysical Research, 97, 6683–6698.

Hustoft, S., S. Bünz, and J. Mienert. 2010. Three-dimensional seismic analysis of the morphology and spatial distribution of chimneys beneath the Nyegga pockmark field, offshore mid-Norway. *Basin Research*, *22*(4), 465-480.

Hustoft, S., J. Mienert, S. Bünz, and H. Nouzé, 2007, High-resolution 3D-seismic data indicate focused fluid migration pathways above polygonal fault systems of the mid-Norwegian margin: *Marine Geology*, 245, 89–106.

Inamori, T. and H. Hato. 2004. Detection of methane hydrate-bearing zones from seismic data. *Resour. Geol., 54*, 99–104.

Janicki, G., S. Schlüter, T. Hennig, and G. Deerberg. 2017. Numerical simulation of gas hydrate exploitation from subsea reservoirs in the Black Sea. *Energy Procedia*, *125*, 467-476.

Jia, J., T, Tsuji, and T. Matsuoka. 2016. Gas hydrate saturation and distribution in the Kumano Forearc Basin of the Nankai Trough. Explor. Geophys. 48 (2), 137 –150. http://dx.doi.org/10.1071/EG15127.

Jiang, F., T, Tsuji, and T, Shirai. 2018. Pore Geometry Characterization by Persistent Homology Theory. *Water Resources Research*, *54*(6), 4150-4163.

Korenaga, J., W. S. Holbrook, S. C. Singh, and T. A. Minshull. 1997. Natural gas hydrates on the southeast US margin: Constraints from full waveform and traveltime inversions of wide-angle seismic data: Journal of Geophysical Research, 102, 15345–15365.

Kret, K., T. Ikeda, and T. Tsuji. 2019. Grid-search inversion based on rock physics model for estimation of pore geometry and grain elastic moduli: application to hydrothermal ore deposits and basalt. *Exploration Geophysics*, 1-11.

Krey, V., J. G. Canadell., N. Nakicenovic., Y. Abe., H. Andruleit., D. Archer., ... and J. F. Lamarque. 2009. Gas hydrates: entrance to a methane age or climate threat? *Environmental Research Letters*, *4*(3), 034007.

Kvenvolden, K. A. 1993. Gas hydrates-geological perspective and global change. *Reviews of geophysics*, *31*(2), 173-187.

Kvenvolden, K.A. 1988. Methane hydrate d A major reservoir of carbon in the shallow geosphere? *Chem. Geol*. 71, 41-51.

Kvenvolden, K. A. and B. W. Rogers. 2005. Gaia's breath–global methane exhalations *Marine Petroleum Geol.* 22 579–90.

Li, G., G. J. Moridis, K. Zhang, and X. S. Li. 2010. Evaluation of gas production potential from marine gas hydrate deposits in Shenhu area of South China Sea. *Energy & Fuels*, *24*(11), 6018-6033.

Løseth, H., L. Wensaas, B. Arntsen, and M. Hovland. 2003. Gas and fluid injection triggering shallow mud mobilization in the Hordaland Group, North Sea. *Geological Society, London, Special Publications*, *216*(1), 139-157.

Makogon, Y.F., S.A. Holditch, and T.Y. Makogon. 2007. Natural gas hydrates - A potential energy source for the 21st century. *Journal of Petroleum Science and Engineering*. 56(1-3), 14-31.

Mavko, G., T. Mukerji, and J. Dvorkin. 1998. *The Rock Physics Handbook, Tool for Seismic Analysis in Porous Media*. Cambridge, UK: Cambridge Univ. Press.

Mavko, G., and T. Mukerji. 1998. A rock physics strategy for quantifying uncertainty in common hydrocarbon indicators: Geophysics, 63, 1997–2008, doi: 10.1190/1.1444493.

Mienert, J., M. Vanneste., S. Bünz., K. Andreassen., H. Haflidason., and H. P. Sejrup. 2005. Ocean warming and gas hydrate stability on the mid-Norwegian margin at the Storegga Slide. Mar. Petrol. Geol. 22, 233–244.

Milkov, A. V., G. R. Dickens, G. E. Claypool, Y.-J. Lee, W. S. Borowski, M. E. Torres, W. Xu, H. Tomaru, A. M. Tréhu, and P. Schulthesis, 2004b, Co-existence of gas hydrate, free gas, and brine within the regional gas hydrate stability zone at Hydrate Ridge Oregon margin: Evidence from prolonged degassing of a pressurized core: *Earth and Planetary Science Letters*, 222, 829–843.

Milkov, A. V., and R. Sassen. 2001. Estimate of gas hydrate resource, northwestern Gulf of Mexico continental slope, Mar. Geol., 179, 71 –83.

Milkov, A.V., and Sassen, R. 2002. Economic geology of offshore gas hydrate accumulations and provinces. *Marine and Petroleum Geology*. 19, 1-11.

Moridis, G. and T. Collett. 2003. Strategies for gas production from hydrate accumulations under various geologic conditions, in: Proceedings of TOUGH Symposium, Lawrence Berkeley National Laboratory, Berkeley, California.

Moridis, G.J., and E.D. Sloan. 2007. Gas production potential of disperse low-saturation hydrate accumulations in oceanic sediments, *Energy Conversion and Management*, 48, 1834–1849.

Muller, P. J., and E. Suess. 1979. Productivity, sedimentation rate, and sedimentary organic matter in the oceansI. Organic carbon preservation. Deep Sea Research Part A. *Oceanographic Research Papers*, 26(12), 1347-1362.

Qorbani, K., B. Kvamme., and T. Kuznetsova. 2017. Simulation of CO_2 Storage into Methane Hydrate Reservoirs, Non-equilibrium Thermodynamic Approach. Energy Procedia, 114, 5451-5459.

Rajan, A., J. Mienert, S. Bünz. 2012a. Acoustic evidence for a gas migration and release system in Arctic glaciated continental margins offshore NW-Svalbard. *Marine and Petroleum Geology*, 32, 36-49.

Reidel, M., T. S. Collett, M. J. Malone, and Expedition 311 Scientists, 2006a, Gas hydrate transect across northern Cascadia margin: EOS, **87**, no. 33, 325–330.

Riedel, M., I. Novosel., G. D. Spence., R. D. Hyndman., N. R. Chapman., R. C. Solem., and T. Lewis. 2006. Geophysical and geochemical signatures associated with gas hydrate–related venting in the northern Cascadia margin. *Geol. Soc. Am. Bull.,* 118(1):23–38. doi:10.1130/ B25720.1

Sarout, J. 2012. Impact of pore space topology on permeability, cut-off frequencies and validity of wave propagation theories. *Geophysical Journal International* 189: 481–92. doi:10.1111/j.1365-246X.2011.05329.x.

Schoell, M. 1988. Multiple origins of methane in the Earth. *Chemical Geology*, 71, 1 -10.

Schulz, H.D., and M. Zabel. 2006. Marine Geochemistry, 2nd Edition. Springer Verlag, Berlin, Germany, 574 pp.

Silpngarmlert, S. 2007. Numerical modeling of gas recovery from methane hydrate reservoirs.

Sloan, E.D. and C.A. Koh, 2008. Clathrate Hydrates of Natural Gases, third ed. CRC Press, Boca Raton, FL.

Spence, G.D., R.R. Haacke, R.D. Hyndman. 2010. Seismic indicators of Natural Gas Hydrate and underlying free gas. In *Geophysical Characterization of Gas Hydrates*; Riedel, M., Willoughby, E.C., Chopra, S., Eds.; *Society of Exploration Geophysicists*: Tulsa, OK, USA, 39–71.

Stocker, T. F., D. Qin, G. K. Plattner, M. M. B. Tignor, S. K. Allen, J. Boschung, ... and P. M. Midgley. 2014. Climate Change 2013: The physical science basis. contribution of working group I to the fifth assessment report of IPCC the intergovernmental panel on climate change.

Suess, E., Torres, M. E., Bohrmann, G., Collier, R. W., Rickert, D., Goldfinger, C., … and Jung, C. 2001. Sea floor methane hydrates at Hydrate Ridge, Cascadia margin. *Geophysical Monograph-American Geophysical Union*, *124*, 87-98.

Takahasi, H., Japan Petroleum Exploration Co., L., T. Yonezawa, J.N.O. Corporation, Y. Takedomi, and Ministry of Economy T.A.I. 2001. Exploration for Natural Gas Hydrate in Nankai-Trough Wells Offshore Japan, Offshore Technology Conference, 13040, Houston (TX), Offshore Technology Conference.

Taladay, K., Boston, B., & Moore, G. (2017). Gas-in-place estimate for potential gas hydrate concentrated zone in the Kumano Basin, Nankai Trough Forearc, Japan. *Energies*, *10*(10), 1552.

Talukder, A.R. 2012. Review of submarine cold seep plumbing systems: leakage to seepage and venting. *Terra Nova*, 24, 255-272.

Tsuji, T., J. Dvorkin, G. Mavko, N. Nakata, T. Matsuoka, A. Nakanishi, A., ... and O. Nishizawa. 2011. Vp/Vs ratio and shear-wave splitting in the Nankai Trough seismogenic zone: insights into effective stress, pore pressure, and sediment consolidation. *Geophysics*, *76*(3), WA71-WA82. https://doi.org/10.1190/1.3560018

US Department of Energy, 2007. http://www.netl.doe.gov/technologies/oil /gas/FutureSupply/MethaneHydrates/about-hydrates/estimates.htm, Vadakkepuliyambatta, S., S. Bünz, J. and Mienert, S. Chand. 2013. Distribution of subsurface fluid-flow systems in the SW Barents Sea. *Marine and Petroleum Geology* ,43, 208-221.

Vadakkepuliyambatta, S., M.J. Hornbach, S. Bünz, and B. J. Phrampus. 2015. Controls on gas hydrate system evolution in a region of active fluid flow in the SW Barents Sea. *Marine and Petroleum Geology*, *66*, 861-872.

Wilkens, R.H., G. J. Fryer., and J. Karsten. 1991. Evolution of porosity and seismic structure of upper oceanic crust: importance of aspect ratios. *J. Geophys. Res.,* 96:17891–17995.

Xu, X., Z. Wan, X. Wang, Y. Sun, and B. Xia. 2016. The characteristics of heat flow in the Shenhu gas hydrate drilling area, northern South China Sea. *Marine Geophysical Research*, *37*(4), 325-335.

Yang, S.O., I. M. Yang, and C.S. Lee. 2000. Measurement and prediction of phase equilibria for water + CO_2 in hydrate forming conditions. *Fluid Phase Equilibrium*, 175 (1-2), 75-89.

Zander, T., M. Haeckel, C. Berndt, W.C. Chi, I. Klaucke, J. Bialas, J., ... and O. Atgın. 2017. On the origin of multiple BSRs in the Danube deep-sea fan, Black Sea. *Earth and Planetary Science Letters*, *462*, 15-25.

Zhou, X., S. Fan, D. Liang, and J. Du. 2008. Replacement of methane from quartz sand-bearing hydrate with carbon dioxide-in-water emulsion. *Energy Fuels,* 22 (3), 1759-1764.

Chapter 2

Distributions of gas-hydrate and free-gas accumulations

2-1 Introduction

Natural gas hydrates are widespread in sediments along continental margins and in permafrost regions. They are crystalline inclusion compounds consisting of both water and gas molecules in the form of rigid lattice cages in the pore spaces of marine sediments. They form under conditions of low temperature and high pressure (*Kvenvolden,* 1993; *Sloan and Koh,* 2007; *Holbrook et al.,* 1996; *Claypool and Kaplan*, 1974). There are large accumulations of gas hydrate and free gas in marine sediments; these have become targets for energy exploration along continental margins worldwide (*Kvenvolden,* 1993; *Collett and Ladd,* 2000). They are also of interest because of their potential to cause slope instability and submarine slumps due to destabilization of gas hydrates during exploration or earthquake (*Xu and Germanovich,* 2006; *Kvenvolden,* 1993; *Sloan and Koh,* 2007; *Waite et al.,* 2009). Such geohazards have the potential to contribute to climate change by releasing large volumes of methane into the atmosphere (*Dickens and Owen,* 1995; *Pecher et al.,* 2005). Therefore, high-resolution mapping of gas hydrates and associated free gas is important both for future energy supplies and for prevention of submarine geohazards.

Since 1993, abundant researches on methane hydrates in Japan have aimed to establish future energy resources (*Oyama and Masutani*, 2017). *Fujii et al.* (2015) estimated the total amount of methane in gas-hydrate-bearing sediments in the eastern part of the Nankai Trough to be 40 trillion cubic feet. Gas hydrates are clearly recognizable in seismic reflection data as strong continuous reflections (known as bottom-simulating reflectors; BSRs) because of the strong acoustic impedance contrast between hydrated and non-hydrated sediments (*Shipley et al.,* 1979). Because the phase transition between gas hydrate and free gas is temperature and pressure dependence, BSRs are characteristically parallel or subparallel to the seafloor. Gas hydrates are commonly trapped over accumulations of free gas sourced by upward fluid fluxes from deeper sedimentary basins (*White,* 1979*; Fraser et al.,* 2016). Because of the distinct seismic character of BSRs, seismic imaging can be used to map gas-hydrate accumulations and underlying free gas along continental margins. High-resolution velocity models are needed to determine the physical properties of gas hydrates and associated free gas, including their spatial distribution and gas saturation (*e.g., Wang et al.,* 2018; *Chhun et al.,* 2018).

Methane hydrates are widely distributed in various forearc basins along the convergent margin of the Japan Trench (Figure 2-1) (*Tanikawa et al.,* 2016; *Taladay et al.,* 2017; *Eng and Tsuji,* 2019). In the Sanriku-Oki basin, one of several forearc basins between the subducting Pacific plate and the northeastern Japan arc, seismic profiles show clear BSRs (*Takano and Tsuji,* 2017). In this study, I applied an automated velocity-picking algorithm to a high-resolution 3D seismic volume in the Sanriku-Oki basin. In areas where no reference borehole velocity data is available, such as my study area, this approach can provide a higher resolution and more accurate velocity structure than other quantitative seismic analysis techniques such as acoustic impedance inversion.

Heat flow is a key factor in evaluations of free-gas and gas-hydrate resources (*Riedel et al.,* 2010; *Li et al.,* 2010; *Poort et al.,* 2012). The heat flow related to fluid flux in marine sediments is affected by faults, slumping, and transgression and regression cycles (*Phrampus et al.,* 2107; *Crutchley et al.,* 2017;*Vargas-Cordero et al.,* 2018; *Singhroha et al.,* 2019). Previous studies estimated heat flow from either directly at drilling sites (*Xu et al.,* 2016) or using thermal probes (*Davis et al.,* 1990; *Hyndman and Wang,* 1993), or using BSR depths (*Yamano et al.,* 1982; *Grevemeyer and Villinger*, 2001; *Ashi et al.,* 2002; *Kinoshita et al.,* 2011; *Ohde et al.,* 2018; *Li et al.,* 2014; *Henrys et al.,* 2003). In this study, I mapped heat flow within a 3D seismic volume by using BSR depths derived from a high-resolution

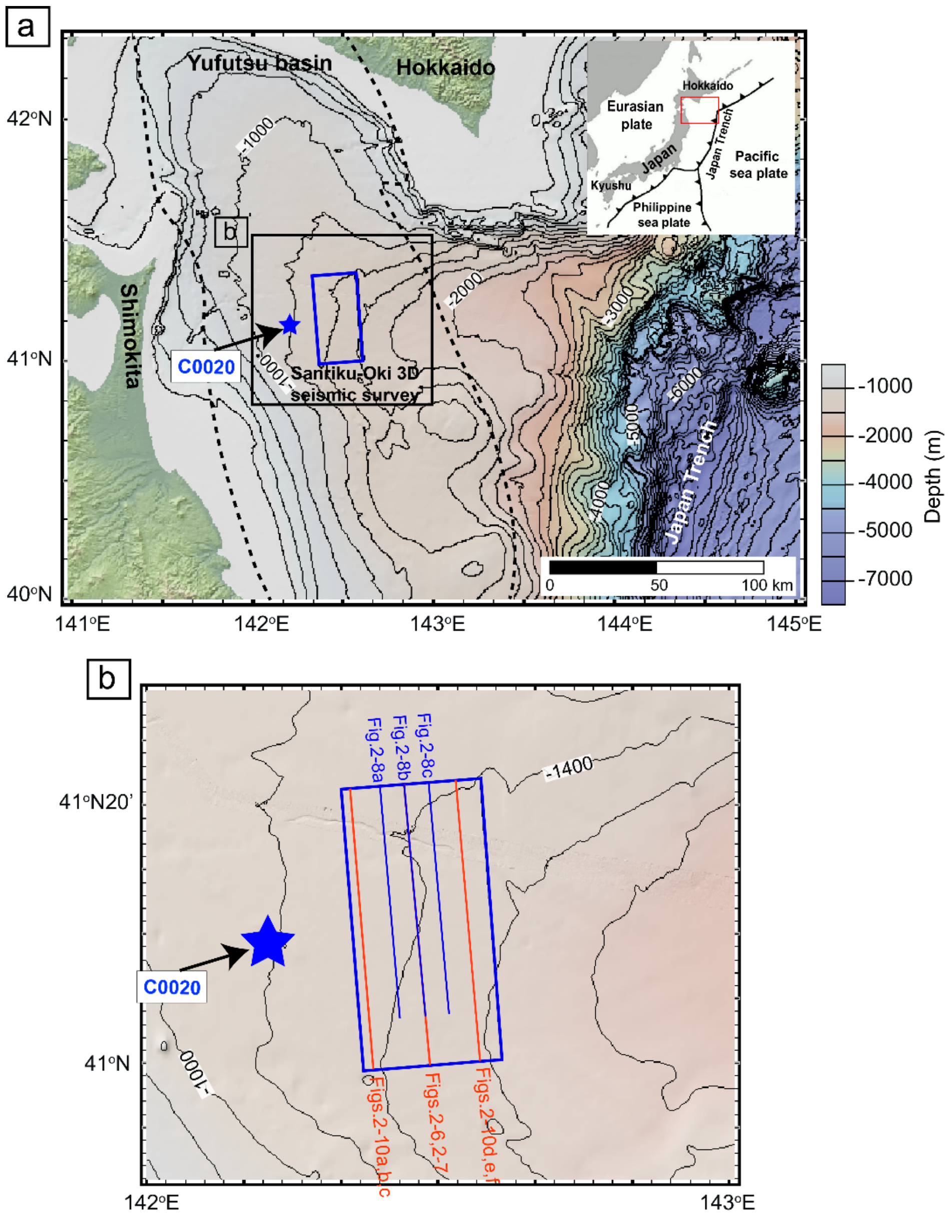

Figure 2-1. *(a) Bathymetric map of offshore northeastern Japan. The inset map shows the study area in relation to a simplified plate tectonic framework. Black dashed area indicates a continuation of forearc basin of northeast Japan. (b) The area of the Sanriku-Oki 3D seismic survey (blue rectangle). Blue stars indicate the locations of site C0020. Red and blue lines represent the seismic lines shown in Figures 2-6, 2-7, 2-8, and 2-10.*

velocity model to investigate the mechanism of formation of gas-hydrate and free-gas systems at a plate convergent margin and to attempt to understand the complex interactions of sedimentary and tectonic processes that control their formation.

2-2 Geological setting

The Sanriku-Oki forearc basin is a part of a N–S trending basinal zone that extends from southern central Hokkaido to offshore northeastern Honshu Island (Figure 1). Basin-filling sedimentation started during the Late Jurassic and has continued until the present, producing ~6000 m of basin-fill sediments in this study area (Takano and Tsuji, 2017). The saturate and aromatic fractions of organic extracts from the Sanriku-Oki borehole (Yufutsu oil and gas field) and adjacent wildcat boreholes revealed various biomarkers of higher plant origin (Yessalina and Suzuki, 2005). Analyses of Late Cretaceous to middle Eocene core samples at depths of 1252–2466 mbsf from the drilled site C0020 (Inagaki et al., 2012) showed that the major lithologies were siltstone, mudstone, sandstones, and coals. The total organic carbon contents of the sediments were 0.5 to 2.0% coals (Yessalina and Suzuki, 2005), maturity levels derived from vitrinite reflectance data were 0.5 to 0.7%, and organic type (II/III) coals in the succession provide potential sources for oil and gas (Osawa et al., 2002; Oda, 2003). The potential for hydrocarbon reserves in the Sanriku-Oki basin is similar to those of the Yufutsu oil and gas field on the southern coast of Hokkaido and the Ishikari Group in central Hokkaido (Osawa et al., 2002; Oda, 2003; Takano et al., 2013), both of which have similar depositional systems, stratigraphic frameworks, and hydrocarbon sources of dominantly Paleocene, Eocene, and Oligocene age.

The stratigraphic succession of the Sanriku-Oki forearc basin includes four major unconformities (Cretaceous, Oligocene, Miocene, and Quaternary; Takano and Tsuji, 2017). The Oligocene unconformity represents the largest tectonic transformation of the basin, which changed from a benched fluvial-dominated forearc basin to a deep marine forearc basin (Takano and Tsuji, 2017). Seismic profiles also show that the Cretaceous to Eocene structure of the forearc basin was strongly controlled by episodes of uplift and subsidence on the trench slope (Takano, 2017). Several marine transgressions and regressions have been recognized in the Upper Cretaceous to lower Eocene successions. A previous exploration well in the basin penetrated middle Upper Cretaceous rocks composed mainly of alternating beds of sandstone and mudstone (Takano and Tsuji, 2017). The lower to middle Eocene sequences above the Cretaceous unconformity consist mainly of sandstone, mudstone and coal beds (Takano and Tsuji, 2017). After Oligocene unconformity, this forearc basin setting type transformed to a deep slope condition due to tectonic subsidence (Takano, 2017), which overlain by transgressive deep marine sediments (i.e. muddy facies) governing over Neogene (i.e. Miocene and Pliocene) and Quaternary succession. In addition, the exploration well also indicated that the lower to late Miocene sequences were composed of sandstone, silty shale, siltstone, thin coal seams, and silty clay with intervals of sand and silts (Gross et al., 2015, Inagaki et al., 2012); and late Pliocene sequence was dominated by diatom-bearing silty clay (Gross et al., 2015, Inagaki et al., 2012). In spectacular, Neogene and Quaternary sequences were sandwiched by many mass-transport deposits which comprised a series of successive submarine slumping due to tectonic subsidence and frequent earthquakes triggered in this basin lying on the plate convergent subduction zone (Eng and Tsuji, 2019; Tanioka and Sataka, 1996).

Recent interpretations of seismic data (Takano and Tsuji, 2017; Takano et al., 2013) have indicated that there was intense deformation inferred from Oligocene unconformity. The dominantly tectonic controls of the formation of forearc basins result in different subsidence patterns (Dickinson, 1995), probably related to regional strike-slip tectonics (Takano et al., 2013; Itoh et al., 2014). Strike-slip faults induced by oblique subduction have been recognized in various forearc basins, for example, the Sumatra, Aleutian, and Kumano forearc basins (Dickinson, 1995; Tsuji et al., 2014; Martin et al., 2010).

2-3 Seismic data

I used 3D seismic reflection data acquired in the Sanriku-Oki forearc basin by the Ministry of Economy, Trade and Industry (METI). The data were acquired by 3D seismic vessel under the National Program for Oil and Gas Prospecting (2008FY METI Geophysical Survey and Basin Evaluation Project "Sanriku Oki 3D").

The energy source was an airgun array (3090 cubic inches or 0.0506 cubic meter) towed at 6 m depth and the data were recorded by 10 streamers of ~5000 m length towed at 8 m depth. Each streamer consists of 384 hydrophones. The hydrophones interval at 12.5m and shot interval at 25m gap are conducted. The CDP folds are 47. The rectangular survey area covered about 800 km^2 (40 km in-line × 20 km cross-line). The bin size was 12.5 m (in-line) × 25.0 m (cross-line) and the sampling interval was 4 ms. The in-line direction of the survey was 353° (Figure 2-1). The vertical resolution of the seismic data is about 5-10 m within the shallow sedimentary sequences. The data processing sequence included surface-related multiple elimination, and radon demultiple (Figure 2-2).

2-4 Method

The seismic data processing provided a high-resolution velocity model (Figure 2-2) that was used to identify BSRs. BSR-derived heat flow was then calculated, as described below.

2-4-1 Conventional semblance

Conventional semblance is a normalized coherency measure that was firstly defined by Taner and Koehler (1969). Semblance is routinely used to estimate MNO velocity as a function of zero-offset time (Figure 2-3a). Following normal move-out correction of a CMP gather, semblance as determined by Neidell and Taner (1971) is computed as:

$$S[i] = \frac{\sum_{j=i-M}^{i+M}(\sum_{k=0}^{N-1} q[j,k])^2}{N\sum_{j=i-M}^{i+M}\sum_{k=0}^{N-1} q[j,k]^2} \qquad (2\text{-}1)$$

where i and j are time sample indices, k is a trace number, and $q[j,k]$ is the trace amplitude at time index j and trace mummer k of the NMO-corrected gather. The inner sums over k

correspond to N MNO-corrected traces in a CMP gather, while the outer sums correspond to a time-smoothing window with length $2M + 1$ centered at time index i.

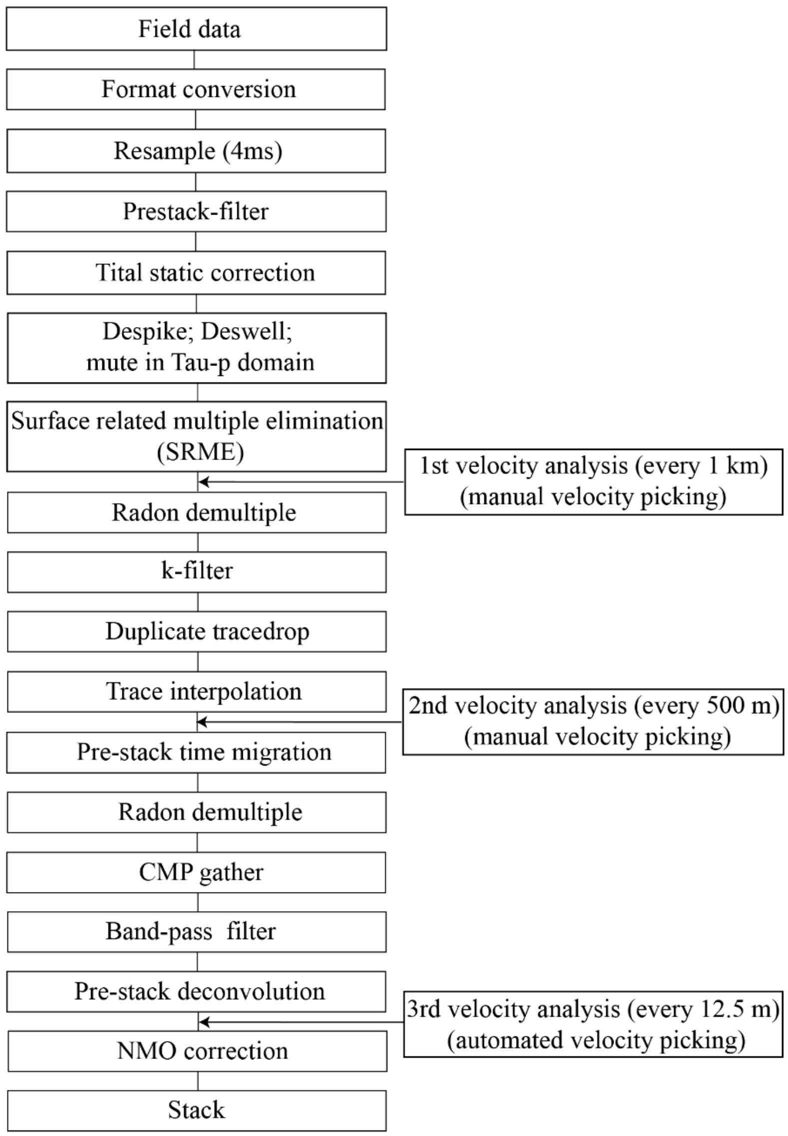

Figure 2-2. *Seismic processing flow for estimating high-resolution seismic velocity (JOGMEC report, 2010).*

2-4-2 AB semblance

The AB semblance (Figure 2-3b) is proposed to handle the velocity analysis of CMP gathers (Fomel, 2009). The AB semblance is computed as:

$$S_w(i) = \frac{\sum_{j=i-M}^{i+M}(\sum_{k=0}^{N-1} a(j,k)w(j,k))^2}{\sum_{j=i-M}^{i+M}(\sum_{k=0}^{N-1}\sum_{k=0}^{N-1} w^2(j,k))} \quad (2\text{-}2)$$

where w(j,k) indicates the weighting function for the index *j* and trace number *k*.

Suppose that the reference sequence has a trend of trace amplitude a(*j,k*):

$$w(j,k) = A(j) + B(j)\emptyset(j,k) \quad (2\text{-}3)$$

where $\emptyset(j,k)$ is a known function that can be chosen as the offset at trace *k*, and A(*j*) and B(*j*) are two coefficients. To estimate *A*(*j*) and *B*(*j*), I can to minimize the following objection function of misfit between the trend and trace amplitude that can turn as following:

$$F_j = \sum_{k=o}^{N=1}(a(j,k) - A(j) - B(j)\emptyset(j,k))^2 \quad (2\text{-}4)$$

Taking derivatives with respect to *A*(*j*) and *B*(*j*) in Equation (2-2) setting them to zero, and solving the two linear equations, *A*(*j*) and *B*(*j*) can be obtained as the following two least-squares fitting coefficients:

$$A[i] = \frac{\sum_{k=0}^{N=1}\emptyset(j,k)\sum_{k=0}^{N=1}a(j,k)\emptyset(j,k) - \sum_{k=0}^{N=1}\emptyset^2(j,k)\sum_{k=0}^{N=1}a(j,k)}{(\sum_{k=0}^{N=1}\emptyset(j,k))^2 - N(\sum_{k=0}^{N=1}\emptyset^2(j,k)} \quad (2\text{-}5)$$

$$B[i] = \frac{\sum_{k=0}^{N=1}\emptyset(j,k)\sum_{k=0}^{N=1}a(j,k) - N\sum_{k=0}^{N=1}a(j,k)\sum_{k=0}^{N=1}\emptyset(j,k)}{(\sum_{k=0}^{N=1}\emptyset(j,k))^2 - N(\sum_{k=0}^{N=1}\emptyset^2(j,k)} \quad (2\text{-}6)$$

Substituting *w*(*j,k*) = *A*(*j*) + *B*(*j*) $\emptyset$(*j,k*) into Equation 2-2 leads to the AB semblance.

Automated seismic velocity analysis based on AB semblance (Figure 2-3) was applied to all CMP gathers of the pre-stack seismic volume (*Fomel,* 2009; *Fomel et al.,* 2013; *Chhun et al.,* 2018). An optimum velocity-picking trajectory can be obtained using the eikonal equation with a finite-difference algorithm (*Fomel,* 2009). Velocity spectra derived from AB semblance are useful in the presence of strong amplitude anomalies and polarity reversal, while these properties lead to inaccurate velocity picking for conventional semblance (*Fomel, 2009*), and are therefore better suited to velocity analyses of sequences containing hydrate and gas reservoirs than conventional velocity analysis methods (Figures 2-3a and 2-3b). A constant velocity increment step of 2 m/s was used to accurately pick optimum velocities from velocity spectra for each reflector. The automatic picking velocity represents the vertical average root mean square (RMS) value without applying lateral and vertical smoothening to prevent the stretching effect.

The uncertainty of estimated velocity from both AB and conventional semblance range 0 to 30 m/s in the gas hydrate and free gas interval (Figures 2-3a and 2-3b), implying the accurate velocity result from these two semblances. The derived velocities were used to correct all CMP traces for normal moveout (NMO) (Figure 2-3d). NMO velocities were then converted to interval velocities according to Dix's equation (*Dix,* 1955). The resulting high-resolution interval velocity model and seismic profiles were crucial to my identification of hydrate and gas reservoirs and my interpretation of fluid migration.

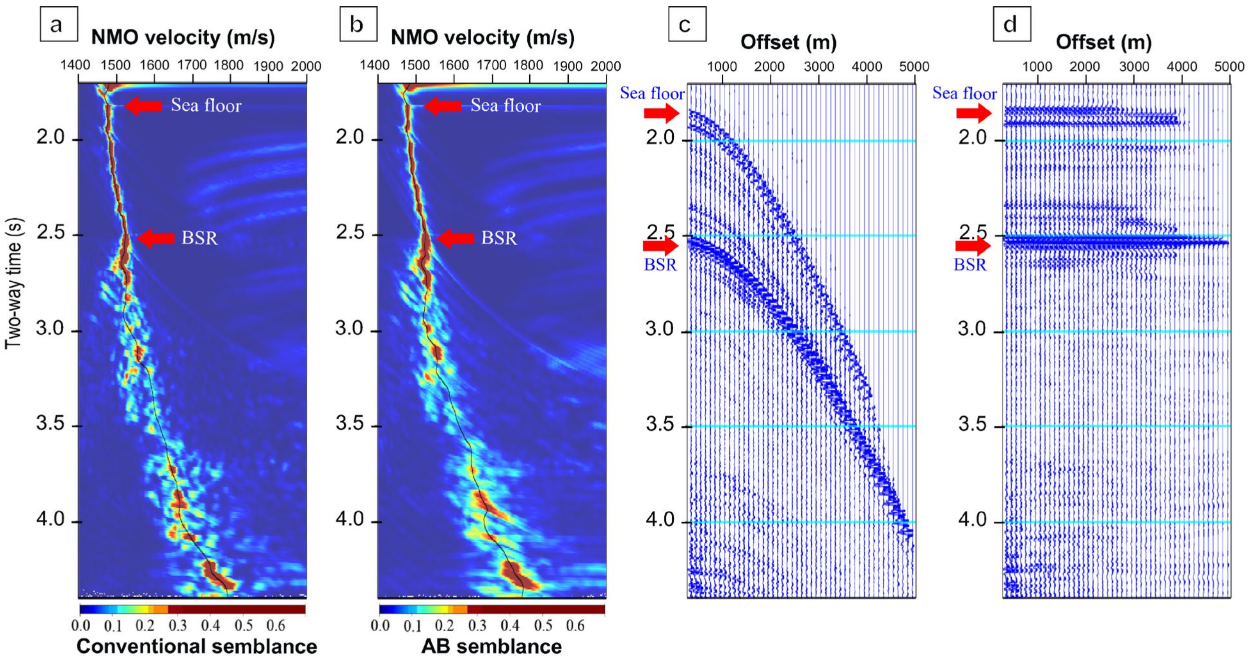

Figure 2-3. *Example of NMO-based velocity analysis of a CMP gather (location shown in Figure 2-1a). P-wave velocity versus two-way-time based on (a) conventional and (b) AB semblance velocity analyses. (c) Uncorrected and (d) NMO-corrected (AB semblance) CMP gathers.*

2-4-3 Heat flow calculation

Local heat flow can be estimated from the depth of the BSR (*Grevemeyer and Villinger*, 2001; *Yamano et al.,* 1982; *Hyndman and Spence,* 1992; *Horozal et al.,* 2009; *Li et al.,* 2014; *Davis et al.,* 1990). Because the BSR represents the phase transition between gas hydrate and free gas, the curve of gas-hydrate stability can be used to estimate heat flow under specific pressure and temperature conditions. Because there have no direct coring or logging data in my study area, I compute the BSR-derived heat flow using shallow and deep physical properties of sediments recovered from hole C0020A of Expeditions 337 (*Inagaki et al*., 2012; *Tanikawa et al*., 2016) and CK06-6 (*Aoike*, 2007) , located about 25 km west of my study area with 1180 m water depth. The coring and logging data used includes bulk density, porosity, thermal conductivity, temperature. The BSR-derived heat flow H (mW/m^2) can be calculated assuming a simple conductive heat transport equation as:

$$H = k(T_{bsr} - T_{sf})/Z_{bsr} \quad (2\text{-}7)$$

where T_{sf} is temperature at the seafloor (°C), T_{bsr} is temperature at the BSR (°C), Z_{bsr} is the depth of the BSR in meters below the seafloor (mbsf), and k is the thermal conductivity from the BSR to the seafloor (W/m °C). In equation (2-7), I used the depth of the BSR (Z_{bsr}) on reflection profile derived from my high-resolution velocity analysis. T_{bsr}, and k were determined from equations (2-8), and (2-9), respectively.

The seafloor temperature T_{sf} is assumed to be 3.6 ^{o}C in my study area, same as the seafloor temperature from hole C0020A in the water depth 1180 m (*Inagaki et al*., 2012).

I assumed that the pressure-temperature conditions at the BSR were those at which methane hydrate is stable. The formation pore pressure is hydrostatic or increased by a few percent of hydrostatic value to depth at least 2425 m in the off-Shimokita Basin (*Inagaki et al*., 2012). Because overpressure is unlikely at the relatively shallow depths of the BSR, the depth to the BSR (water depth plus overburden thickness) was converted to pressure by assuming a hydrostatic model for sediment pore pressure (*Hyndman et al.,* 1993; *Li et al.,* 2014). The temperature log data from hole C0020A (~ 25 km west of my study area) measured at 1200 to 2466 m below seafloor (mbsf), which is deeper than the depth of BSR (390 to 650 mbsf). We, therefore, used the hydrate phase boundary of *Maekawa et al*. (1995) instead of using temperature-depth relationship data, which could introduce large error in estimating the temperature at the BSR. I compared gas hydrate phase boundary equation of *Maekawa et al.* (1995) with previous gas hydrate phase boundary equations (Figure 2-4) (i.e., *Dickens and Quinby-Hunt*, 1994; *Tishchenko et al.*, 2005) and temperature-pressure relationship from hole C0020A (Figure 2-5).

The temperature at the BSR (T_{bsr}) was calculated using an empirical relation for equilibrium at the phase boundary of gas hydrate stability with 3.5 wt% sodium chloride solutions, similar to the salinity of natural seawater in pressures range up to 18 MPa (*Maekawa et al.,* 1995):

$$\ln(p/po) = -926.815 + 31979.3/T + 144.909\ln T + 5847.92x + 3220.26x2 + 5840.50\ln(1 - x) \quad (2\text{-}8)$$

where *T* is temperature (K) and *p* is the pressure (MPa), p^o is the atmospheric pressure (MPa), *x* is the mole fraction of sodium chloride in liquid phase.

The average thermal conductivity between the seafloor and the BSR, *k* in equation (2-7), was estimated by two-component system of water and solid matrix (*Davis et al.,* 1990; *Villinger et al.,* 1994) as follows:

$$k = k_w^{\emptyset} k_g^{1-\emptyset} \quad (2\text{-}9)$$

where $k_w^{\emptyset}$ ($0.6\ Wm^{-1}K^{-1}$) is thermal conductivity of water, $k_g^{1-\emptyset}$ ($2.5\ Wm^{-1}K^{-1}$) is the thermal conductivity of solid matrix, and $\emptyset$ is porosity.

The porosity-depth relationship (*Tanikawa et al.,* 2016) at hole C0020A is explained as:

$$\emptyset = 0.740\exp(-0.000456z) \quad (2\text{-}10)$$

where *z* is depth (mbsf).

Finally, I calculated the BSR-derived heat flow by substituting the parameters determined in equations (2-8)–(2-9) into equation (2-7).

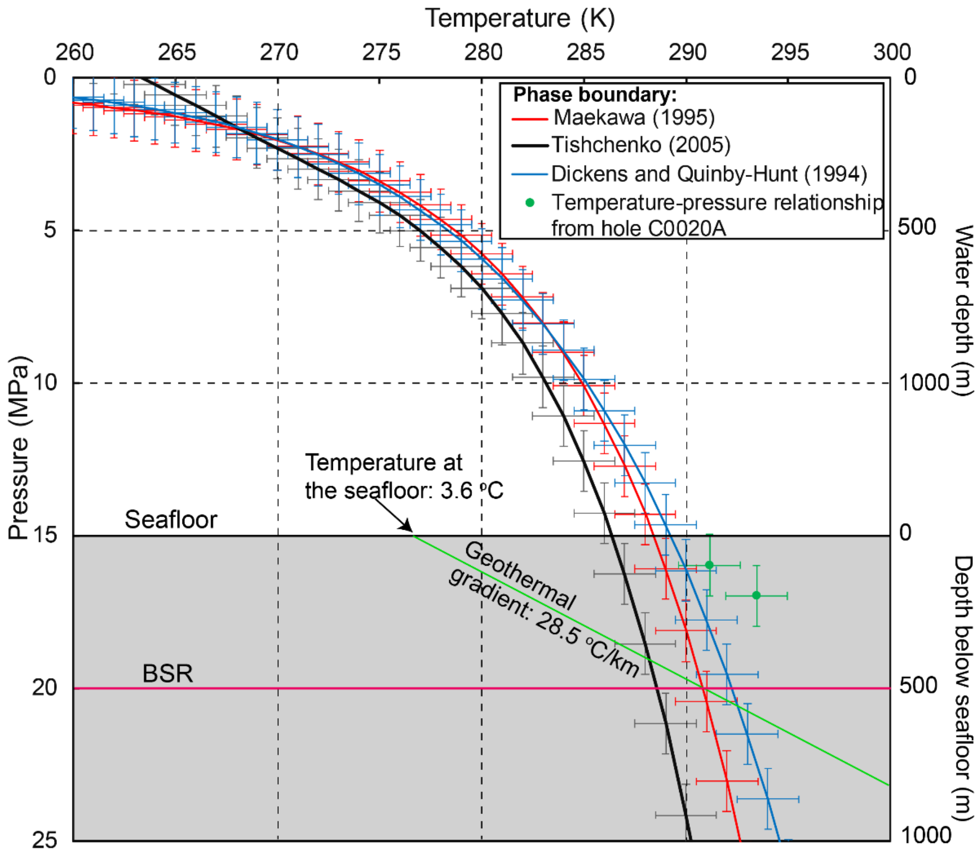

Figure 2-4. *Phase diagram of gas hydrate stability in my study area with a regional geothermal gradient of ~ 28.5 °C/km. Error bars correspond to 1 and 1.5 standard deviation for temperature and pressure, respectively.*

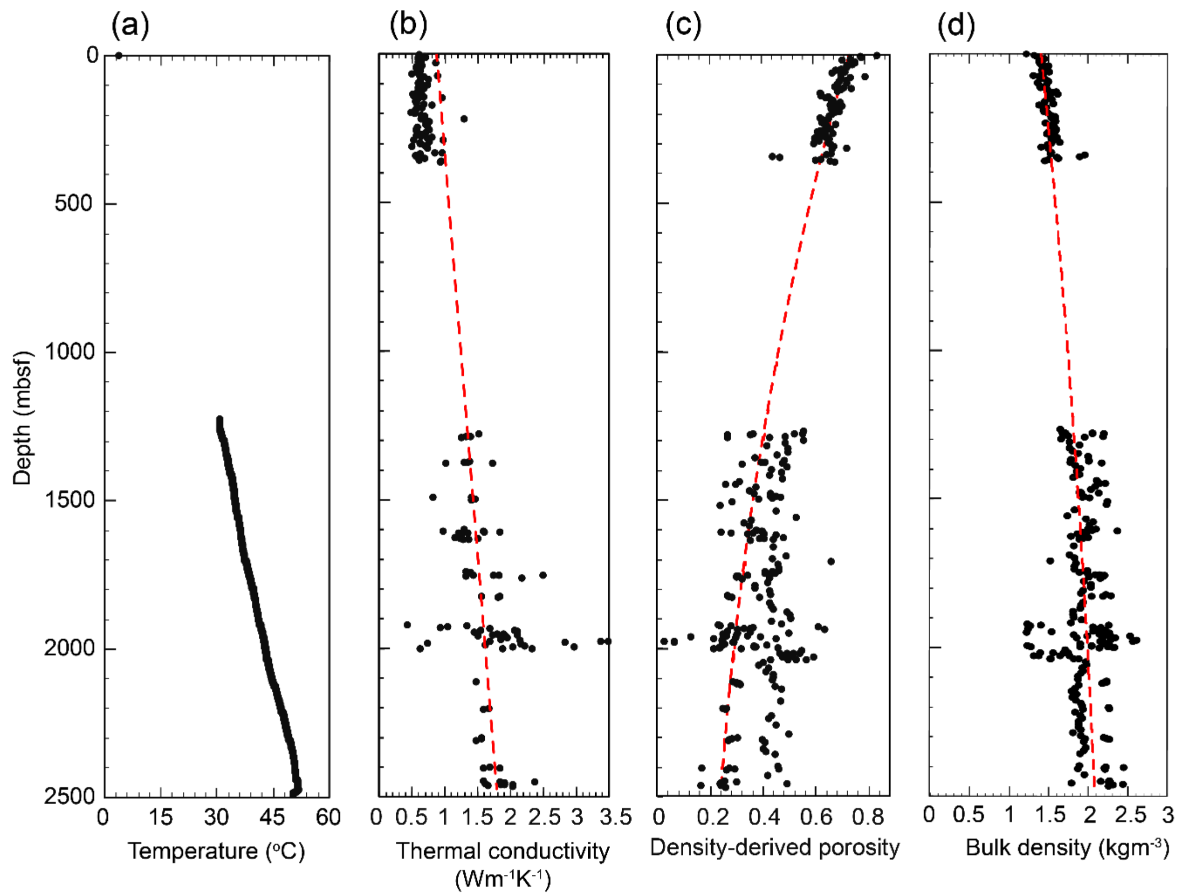

Figure 2-5. *Physical properties of sediments from hole C0020A during the expedition 337 (200 to 2446 m below seafloor) and CK06-06 (0 to 360 m below seafloor). (a) Temperature profile estimated using the Environmental Measurement Sonde (EMS). (b) Thermal conductivity. (c) Porosity. (d) Bulk density.*

2-5 Results and interpretation

2-5-1 Seismic profiles and high-resolution P-wave velocity model

The high-resolution seismic profiles I used greatly facilitated my interpretation of lithological boundaries and unconformities across the survey area (Figure 2-6). I estimated the depth of the BSR to be ~500 mbsf (Figure 2-7). High amplitude reflections beneath the BSR possibly represent temperature and pressure variations in the equilibrium state of gas hydrates (*Taladay and Moore,* 2015). I also observed lateral discontinuities in the BSR (Figures 2-8 and 2-10), which may represent either instability of the gas flux beneath the gas-hydrate zone or intense deformation (faults or chimneys) that cut the sedimentary sequence (Figures 2-10b and 2-10e) (*Bünz et al*., 2012; *Plaza-Faverola et al*., 2015; *Plaza-Faverola et al*., 2017). During dissociation of gas hydrate, free gas and water are expelled, which reduces the shear strength of sediments and makes them more prone to failure, which is likely the cause of the lateral discontinuities of the BSR within slump deposits.

Superimposition of my high-resolution P-wave velocity model on the reflection seismic profile (Figure 2-7b) shows that P-wave velocities clearly distinguish the sediments containing gas hydrate and free gas from the surrounding sediments. The high P-wave velocities I identified for gas-hydrate-bearing sediments (1700–2100 m/s) are consistent with those reported in other regions (*Ker et al*., 2019; *Iván et al.,* 2017; *Fraser et al*., 2016; *Li et al.,* 2013; *Pecher et al.,* 1996; *Korenaga et al.,* 1997; *Mienert and Posewang,* 1999). The concentration of CH_4 may localized seepage within slump areas or widespread CH_4 release from dissociation of gas-hydrate-related slumps leading to pore volume expansion, sediment weakening and even releasing methane into the water column (Faure et al., 2006; Pecher et al., 2005). My observation of high P-wave velocities within slump units above the BSR (Figures 2-7b, 2-8; slump E), similar to that investigated in seismic data (Pecher et al., 2005), suggesting the possibility of the gas-hydrate saturations in porous slump units in my study area are high.

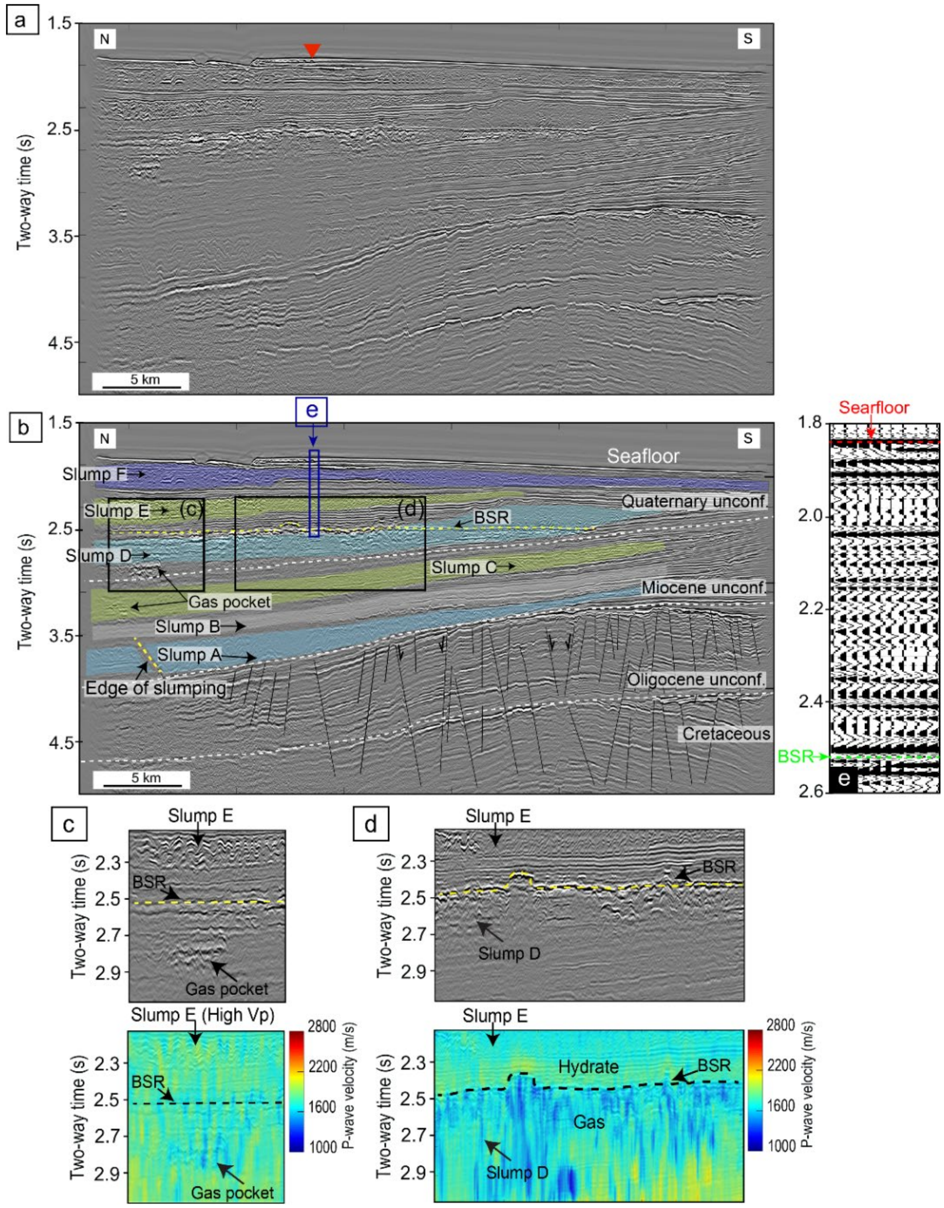

***Figure 2-6**. (a) N-S seismic reflection profile across the Sanriku-Oki forearc basin (location shown in Figure 2-1). (a) Uninterpreted profile and (b) interpreted seismic profile of panel (a). The strong reverse-polarity reflection represents the BSR (yellow dashed line). White dashed lines mark unconformities (Cretaceous, Oligocene, Miocene, and Quaternary) based on correlation with seismic stratigraphy of Takano (2017). Black lines indicate major faults. Colored areas mark six interpreted slump sequences (A to F) characterized by internal imbrication and chaotic structures. The red arrowhead in (a) shows the location of the CMP gather displayed in Figure 2-3. (c) and (d) The enlarged seismic profiles showing the strong amplitude reflection of gas pocket, gas accumulation zones and slumps with corresponding high P-wave velocity extracted from 3D velocity model.*

P-wave velocities are considerably lower beneath the BSR due to the saturation of free gas in the sediments there (*Singh et al.,* 1993; *Hyndman et al.,* 2001; *Pecher et al.,* 2001). According to my analyses, the P-wave velocity of sediments containing free gas is 1000–1500 m/s in my study area (Figures 2-7, 2-8, and 2-10). Although the seismic velocities of free-gas bearing zones are related to gas saturation, the velocity range I estimated is consistent with the results of previous studies (*Korenaga et al.,* 1997; *Tinivella and Accaino,* 2000; *Bünz et al.,* 2005). Attenuation of seismic signal strength beneath a BSR has been reported to represent an irregular distribution of zones of low-velocity gas-charged sediments that produces chaotic reflections (*Gorman et al., 2002*; *Arntsen et al.,* 2007). Time slices of my 3D velocity model at 2.4 s TWT (Figures 2-9a and 2-11a) and 2.5 s TWT (Figures 2-9b and 11b) strongly suggest that gas-hydrate and free-gas accumulations are widespread within my study area. The low-velocity, gas-charged sediments I interpreted extend ~30 km along a N–S direction in my study area.

To supplement my interpretation of the spatial distributions of gas hydrate and free gas within my study area, I compared several profiles extracted from my high-resolution P-wave velocity model with corresponding profiles of seismic amplitude envelopes published by *Eng and Tsuji* (2019) (Figure 2-8). The high envelope values they characterized as zones of free gas are well consistent with the low P-wave velocities I determined below the BSR between 2.5 and 2.9 s TWT (~500 to 900 m below the seafloor; Figure 2-7).

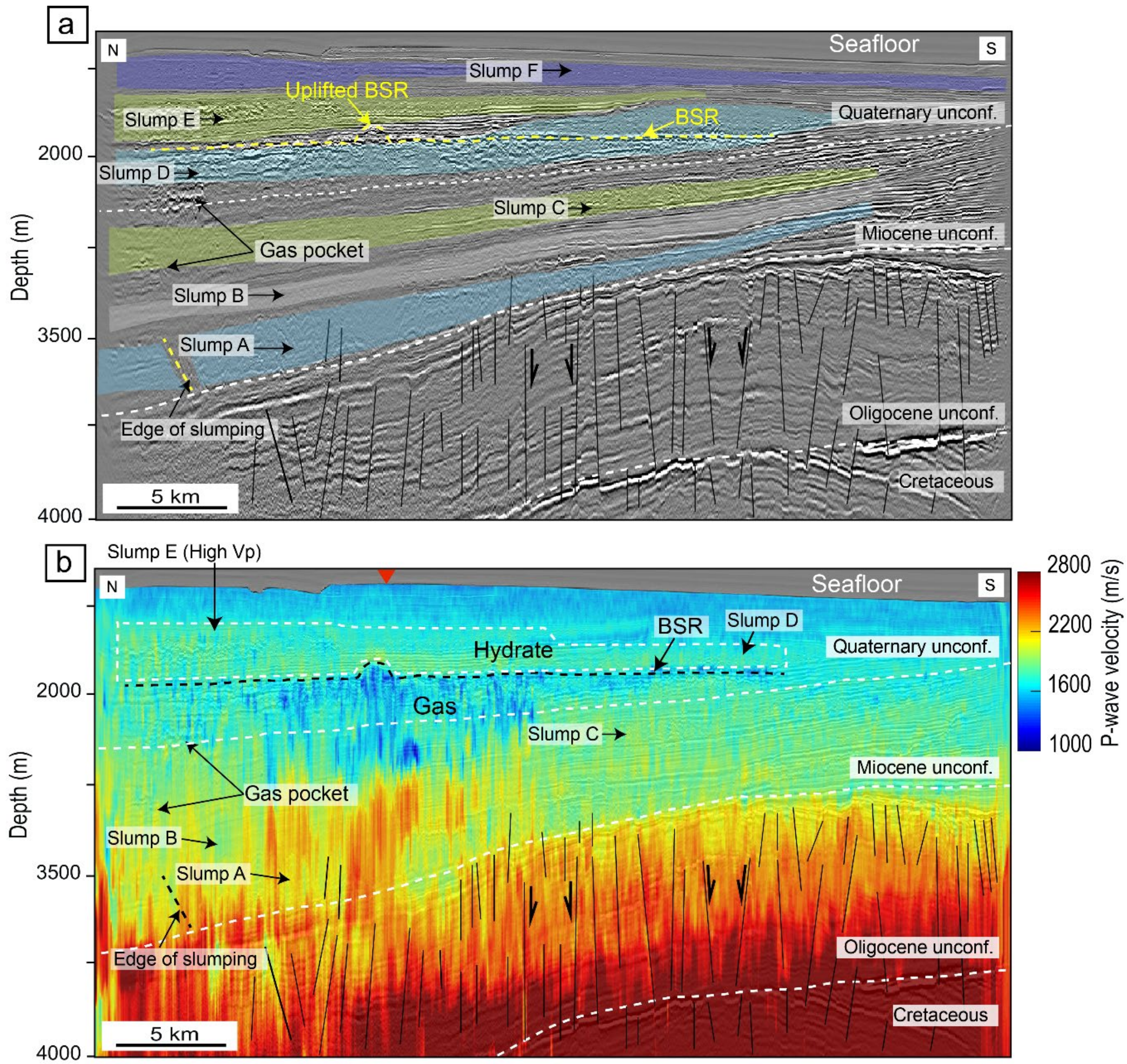

Figure 2-7. *(a) N-S seismic reflection depth profile illustrating intense normal faulting that can provide pathways for upward fluid migration from depth. (b) High-resolution P-wave velocity superimposed on the interpreted seismic depth profile in (a) showing gas hydrate zone (high velocities above BSR), free gas accumulations (low velocities beneath BSR), and a gas pocket in the slump D interval. The profile location is shown in Figure 2-1.*

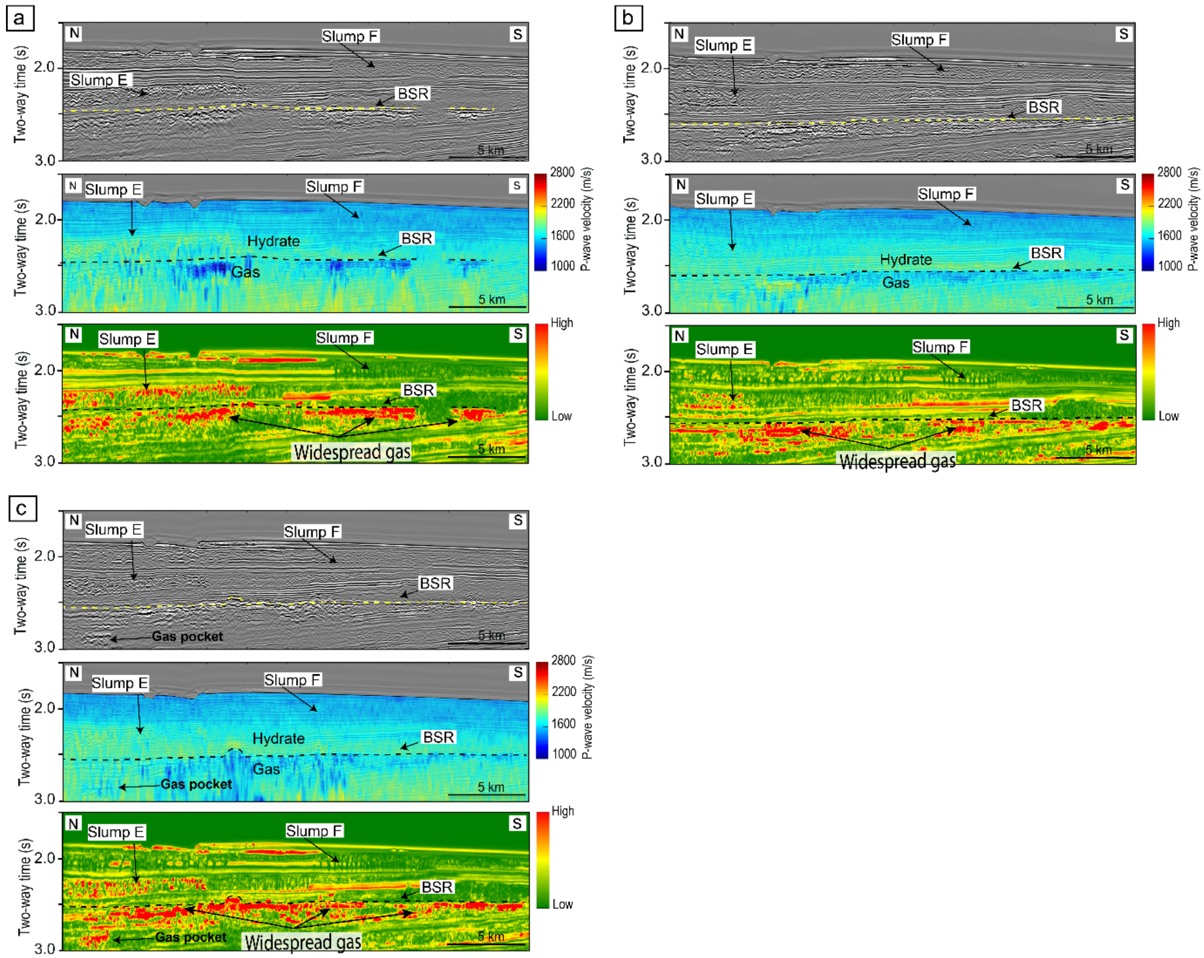

***Figure 2-8**. Comparisons of three profiles (a, b, and c) of seismic reflection profiles, high-resolution P-wave velocities extracted from the 3D velocity model of this study (upper panels; profile locations shown in Figure 2-1) with corresponding profiles of envelopes showing interpreted distributions of free gas below the BSR.*

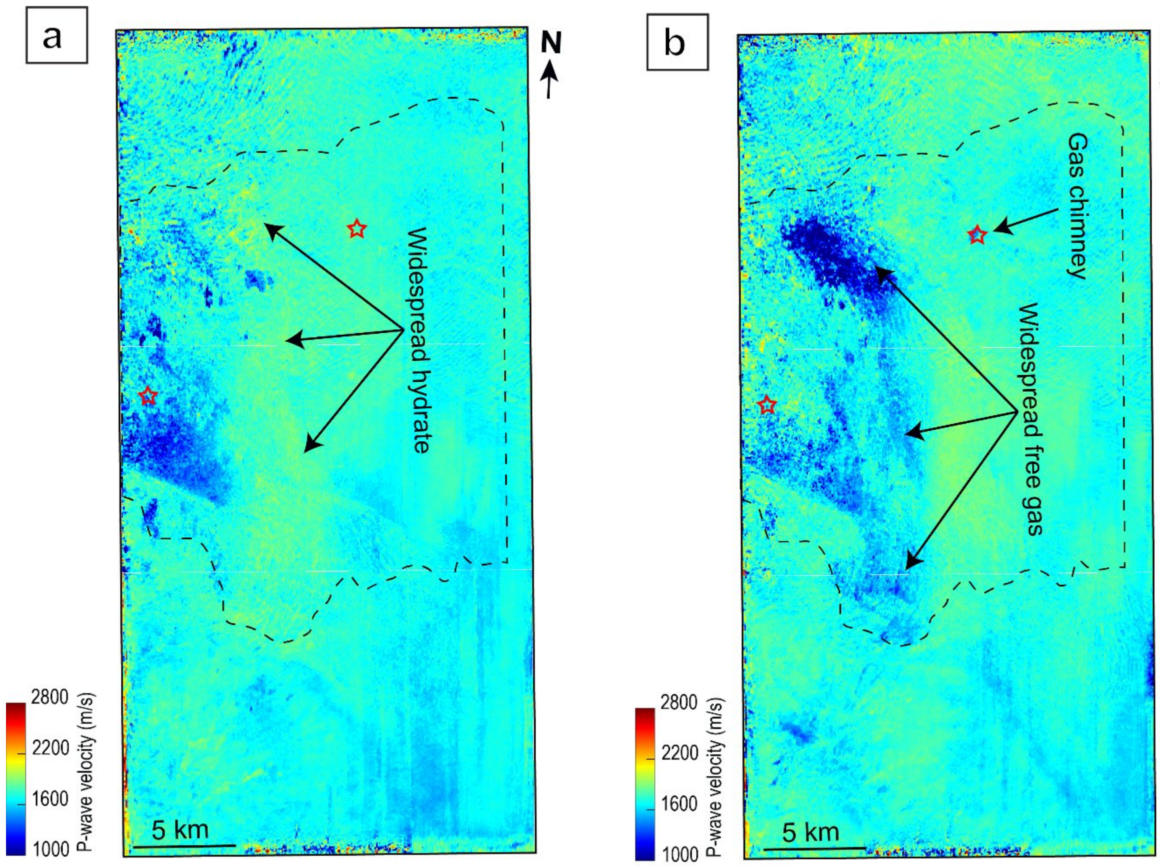

Figure 2-9. *Time slices from the 3D P-wave velocity model at (a) 2.4 s TWT, through gas-hydrate accumulations above the BSR, and (b) at 2.5 s TWT, through free-gas accumulations below the BSR. Black dashed lines mark the boundary of the BSR observed within my study area.*

2-5-2 Heat-flow mapping

I used the depth of the BSR determined from my high-resolution seismic velocity model to map heat flow in the study area (Figure 2-12). The depth of the BSR ranges from 390 to 650 mbsf (Figure 2-12a). The shallowest BSR is beneath seafloor channels in the northern part of the study area and corresponds to areas of high heat flow (Figure 2-12b). Other areas of high heat flow (Figure 2-12b) correspond to areas I interpreted to have high concentrations of free gas and gas-hydrate (Figures 2-10 and 2-11). Local areas of uplift of the BSR (Figures

2-7b and 2-12b) in the middle of the study area are associated with high heat-flow anomalies. Areas of high heat flow (~30 to 35 mW/m^2) were clearly associated with the edge of the area of slumping, and with gas chimneys and fault zones (Figures 2-12b and 2-12c). Heat flow at the location of the northernmost gas chimney is higher than its immediate surrounds (Figures 2-10a, 2-10d, and 2-12b), which suggests that high-temperature fluids are migrating upward through the chimney into the overlying gas-hydrate bearing sediment.

Several of the parameters I used in my calculations of heat flow may have introduced uncertainties in my results. These include depth to the BSR, pressure at the BSR, bathymetric irregularities, and the value I used for thermal conductivity. Although lateral variations in seismic velocity often lead to uncertainties in time-depth conversions (*Li et al.,* 2014), my high-resolution velocity model should have reduced those uncertainties. I estimated that depth errors up to a maximum of ~10 ms TWT in picking BSR reflectors would result in an error of ~7% in heat flow values.

The assumed pressure model could also have affected my estimates of the temperature gradient. The different result of lithostatic and hydrostatic pressure at the BSR is about 12%. Uncertainties in lithostatic and hydrostatic pressures could have generated an error of 7% in the estimated temperature at the BSR, leading to an error of ~ 9% in the heat flow values. Moreover, my errors in the calculation of thermal conductivity were ~1%, which is largely depend on depth of BSR as in the above equation (4), producing a heat flow error of 4%. Furthermore, for the case of sea floor temperature, the heat flow values would vary by 11% if I estimated the different seafloor temperature values of 3.6 ^{o}C and 2 ^{o}C. By using the high-resolution velocity model, therefore, the most significant error might have been in my determination of temperature (*Henrys et al.,* 2003). The cumulative error in my estimation of heat flow was 31% or even more, which is similar to errors in previous studies in other regions (*Yamano et al.,* 1982; *Ganguly et al.,* 2000; *Townend,* 1997). Even though I used a high-resolution P-wave velocity model to estimate the BSR-derived heat flow, I acknowledge that errors in my calculations could include the effects of, for example, hydrate morphology, sediment density, pore size, and grain size, all of which I considered to be negligible (*Rao et* *al.,* 2001). Nonetheless, my estimated heat flow (Figure 2-12) broadly agreed with heat flows measured ~50 km south of my study area (~32 mW/m^2; *Yamano et al.,* 2008; *Kimura et al.,* 2012).

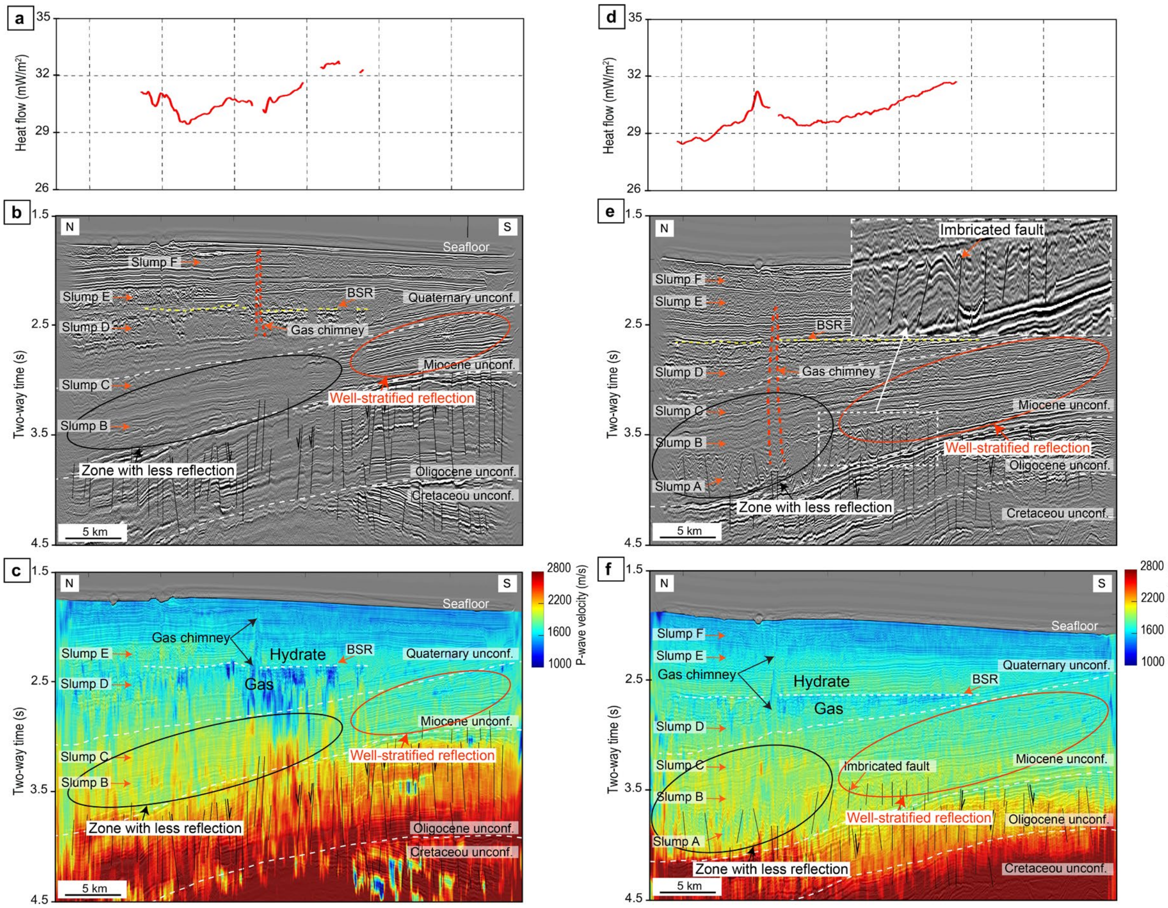

***Figure 2-10**. (a) and (d) BSR-derived heat flow along two profiles extracted from the 3D model (locations shown in Figure. 2-1). (b) and (e) Interpreted seismic reflection profiles showing the strong reflection of the BSR (yellow dashed lines). White dashed lines mark unconformities (Cretaceous, Oligocene, Miocene, and Quaternary) based on correlation with seismic stratigraphy of Takano (2017). Red arrows show slump sequences A to F. Black lines indicate major faults. Red dashed lines indicate interpreted gas chimneys that disrupt the sedimentary sequence and pierce the BSR. (c) and (f) P-wave velocity profiles showing gas hydrate and free-gas accumulations and chimney structures within which low P-wave velocities suggest the presence of high concentrations of free gas.*

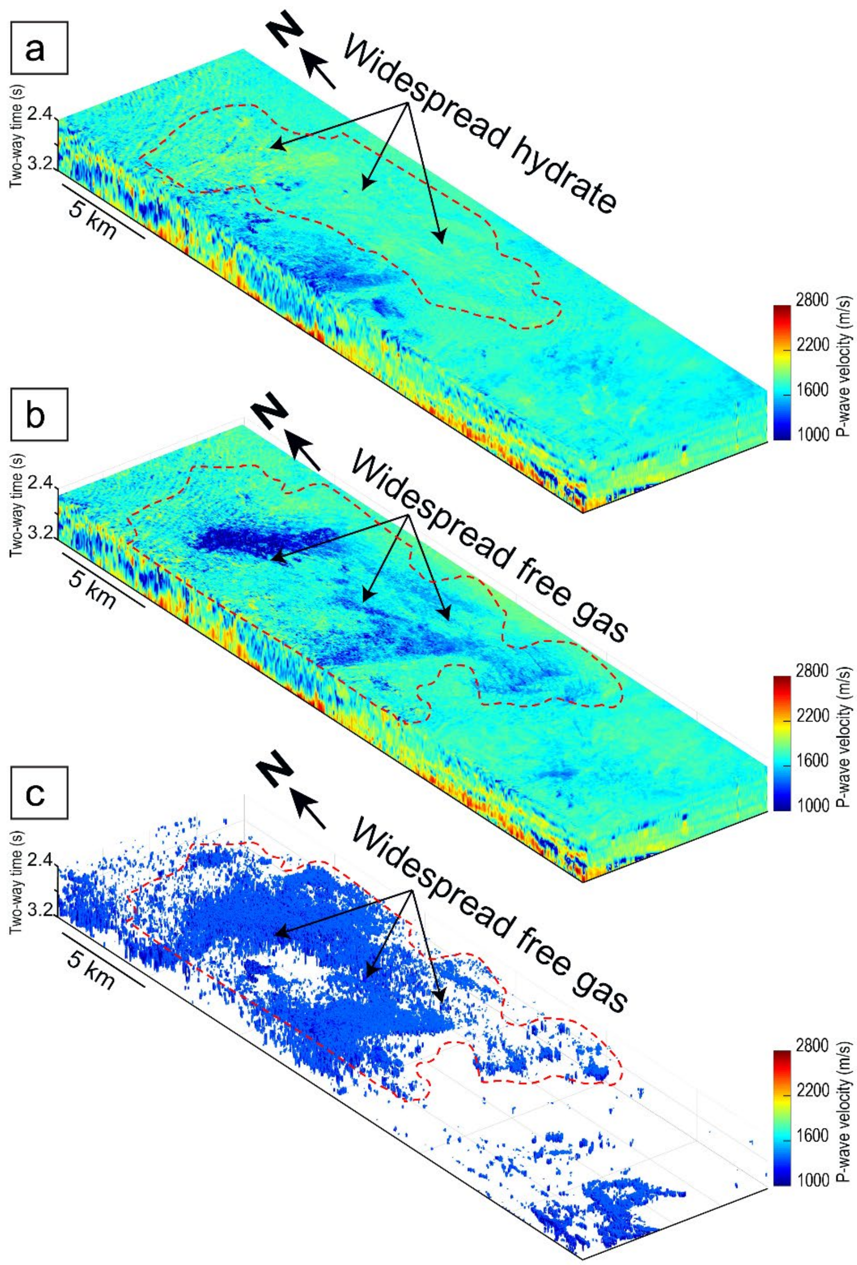

Figure 2-11. *3D views of the high-resolution P-wave velocity model at high gas saturation area (landward half of 3D survey area) showing (a) widespread gas hydrate at 2.4 s TWT, (b) widespread free gas at 2.50 s TWT, and (c) a low P-wave velocity distribution ranging from 1000 to 1400 m/s (lower than the velocity of seawater, generally ~1500 m/s) at 2.5 s TWT, indicative of the free-gas distribution. This figure suggests that there is more free gas in the northwest of the study area. Red dashed line showing the boundary of gas hydrate and free gas within the study area.*

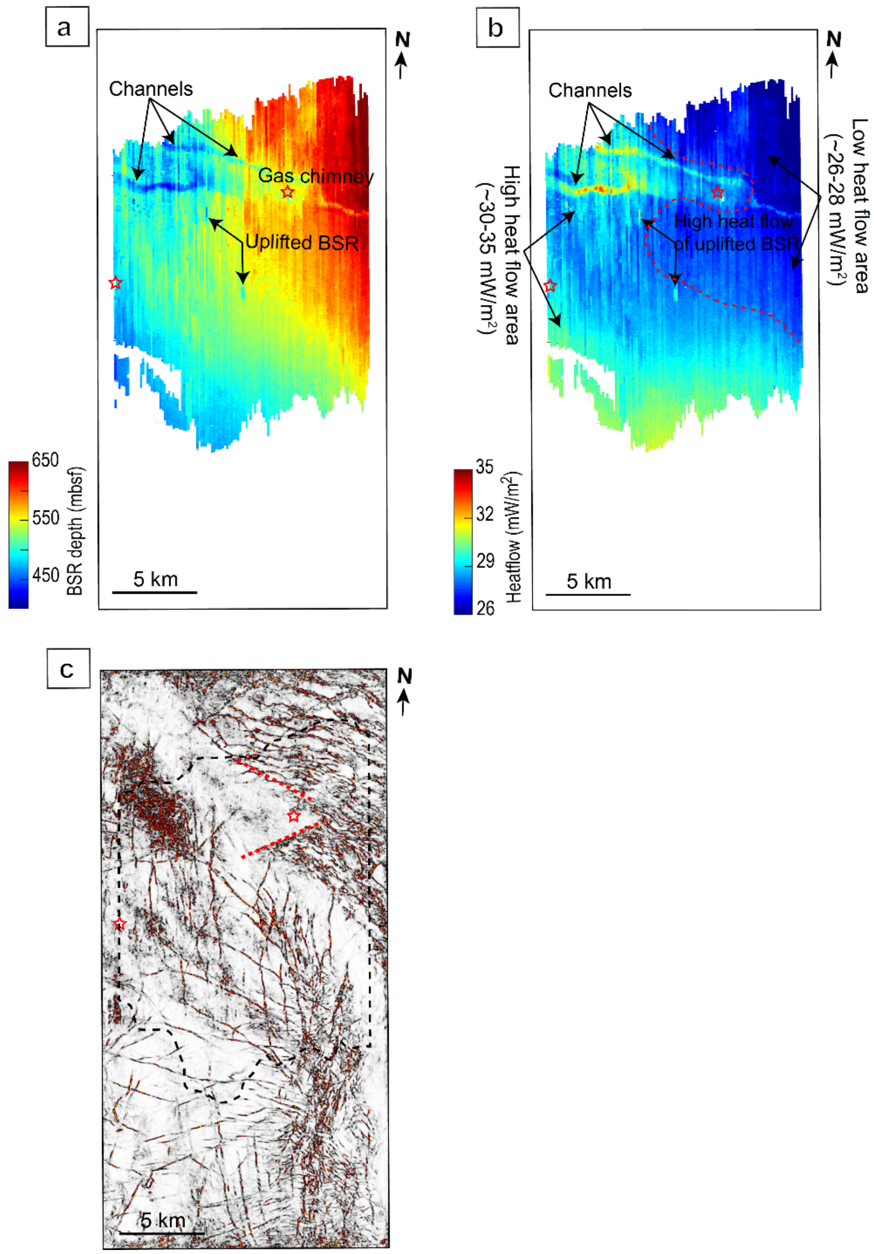

Figure 2-12. *BSR-derived heat-flow distribution in the study area showing the edge of the area of slumping (red dashed lines) and locations of gas chimneys (red stars) and channel-like structures due to the effect of channel at the seafloor. (a) Depth to BSR. (b) Heat flow. Red dashed line represents the boundary between high and low heat flow areas. (c) Chaos attributes at 3.94 s TWT showing the distribution of faults and edges of slump (Eng and Tsuji, 2019). Black dashed lines mark the boundary of the BSR observed within my study area.*

2-6 Discussion

2-6-1 Hydrocarbon migration pathways

Three-dimensional seismic data and estimated heat flow can be used to identify fluid migration pathways in forearc basins. Numerous faults, gas chimneys, dipping sedimentary layers, and slumps in my study area are the results of tectonic motion (i.e., extension and subsidence) (Figures 2-7, 2-8, and 2-10). These structural features have been shown to provide gas migration pathways leading to the accumulation of gas hydrate and free gas in Quaternary sequences off the east coast of Japan for which the depositional environment has changed from regressive to transgressive succession filled by turbiditic sediments (i.e., intercalated sand and mud facies) and slump deposits (*Takano and Tsuji,* 2017, *Eng and Tsuji,* 2019; *Miyakawa et al.,* 2014). I identified gas chimneys in the interval between the Miocene and Quaternary unconformities (Figure 2-10). One of these chimneys is near the edge of the area of slumping and clearly links gas-hydrate and free-gas accumulations (Figure 2-10e; *Eng and Tsuji,* 2019). The P-wave velocity within the chimney is up to ~300 m/s slower than in the surrounding sedimentary layers and the gas-hydrate zone, and clearly indicates the presence of free gas (Figures 2-10c and 2-10f). The low P-wave velocity within the gas chimneys could alternatively be explained by the effect of high pore pressure on the elastic moduli and density of the sediments (*Tsuji et al.,* 2008). In the Sanriku-Oki forearc basin, most of the gas chimneys have formed just above coal-bearing layers at the edges of slump deposits in Quaternary and late Miocene sediments (Figure 2-10e) (*Eng and Tsuji,* 2019). My heat-flow studies have demonstrated that gas chimneys can provide conduits for the upward migration of gas into shallow formations whose temperature and pressure conditions are favorable for the formation of gas hydrate. High P-wave velocity of gas hydrate forming an effective hydrological seal could deflect upward migration of fluid to the Quaternary reservoir rock.

Eng and Tsuji (2019) used post-stack seismic profiles extracted from the 3D seismic data I used in this study to discuss the major role of a series of slumps in providing gas-migration pathways in the region. The slump structures (labeled A to F in Figure 2-6b) are characterized by complex imbricate fault systems, chaotic reflections, and discrete seismic stratigraphic units within the Miocene to Quaternary sequence (Figures 2-6, 2-10b, and 2-10e). I used my high-resolution velocity model to delineate these slump deposits and their internal geometries. Most of the slump deposits within the basin have relatively low P-wave velocities, possibly due to the presence of free gas or numerous fractures (Figures 2-7 and 2-8), and therefore make an important contribution to the mobilization of free gas in the study area. The slumps above the BSR (E and F) have higher P-wave velocities than the deeper slumps, which suggests that these shallow, more porous slump deposits have higher gas-hydrate saturations.

However, the upward migration of gas might cease beneath impermeable layers, and could thus produce accumulations (pockets) of gas. Most of the gas pockets I identified are at depths of less than 900 mbsf and are within the Miocene and Quaternary sequence (Figure 2-7). They are characterized by high-amplitude reflection and low-velocity anomalies (Figure 2-7) and likely accumulated in sand-rich sediments below a clay-rich seal. They are of limited lateral extent and probably contain gas that has leaked upward from the edges of deeper slumps (Figures 2-6 and 2-7; *Eng and Tsuji,* 2019). The slump edges may be related to local shear-failure surfaces at downslopes within the loose unconsolidated faulted sediments and parallel to the direction of slump flow (*Bull et al., 2009*) that were initiated during episodes of extensional or compressional stress.

2-6-2 Implication of heat flow for the migration and accumulation of hydrocarbons

My high-resolution P-wave velocity model has improved my understanding of the spatial distributions of heat flow, gas hydrate, and free gas in the sediments of the study area. I have assumed that fluid migration is a key factor controlling the temperature gradient and is thus instrumental in the spatial variations of heat flow in the basin (*Bredehoeft and Papadopoulos,* 1965). On the seismic indicators of high concentration of gas-charged fluids (Figures 2-10b and 2-10e) include reductions in acoustic impedance, less reflective seismic horizon (*Jones* *et al., 2010*) and result as high and low velocity fluctuations, serving as important features in defining of hydrocarbons in marine sediments (*Spence et al., 2010*). Less reflective seismic zone below BSR could be because of acoustic attenuations of seismic wave travel through a thick gas-charged sediment (*Taladay et al., 2017*). I have shown that heat flow is high above faults and chimneys within these less reflective seismic zones (Figures 2-10 and 2-12). The areas of high heat flow in the study area likely correspond to areas with high concentrations of free gas and hydrate (Figure 2-10) (Li et al., 2014). In contrast, in the east and northeast of the study area, well-stratified reflection horizons contain uniform velocity of lithological units, where BSRs and concentration of free gas cannot be observed (Figure 2-10). Moreover, heat flow is relatively low in these areas, away from the area of intense faulting and gas chimneys. This area of lower heat flow might be related to the thicker forearc basin sediments and deeper basement there, which not allow fluid to easily migrate from depth to move upward compared to fluid flow that is more active in less overburden sediments (*Han et al.,* 2019).

Upward fluid flows are required to maintain high concentrations of gas hydrate in the shallow subsurface (*Kvenvolden and McMenamin,* 1980; *Hovland et al.,* 1999; *Judd and Hovland,* 2009). The presence of faults, chimneys, slumps, and underlying gas source rocks allow the upward migration of fluids to develop gas-hydrate accumulations in the overlying sedimentary sequence. Crustal extension in active forearc basins can induce faulting (*Hayes et al.,* 1995; *Bello et al.,* 2017; *Tsuji et al.,* 2013) and associated cracks (*Yan et al.,* 2006; *Li et al.,* 2012; *Fraser et al.,* 2016; *Hustoft et al.,* 2009; *Vanneste et al.,* 2005; Tsuji et al., 2015), both of which have been recognized as conduits for upward migration of gas. Previous studies (*Ando,* 2005; *Takano et al.,* 2013; *Yagishita and Takano,* 2005) have reported that Cretaceous to Paleocene coal-bearing fluvial and shallow-marine sediments in forearc basins off northeastern Japan provide major petroleum source rocks. The 3D seismic data I used show intense normal faulting that intersects potential hydrocarbon source rocks below the Miocene unconformity (Figures 2-6, 2-7, and 2-10) where there is considerable variability of the strike of faults, which might lead to anisotropic permeability of the sequence there (*Hustoft et al.,* 2009). The principle axis of permeability in faulted zones is parallel to the fault plane, so in areas where there are multiple fault strikes and numerous intersecting fault planes, fault zones may provide particularly effective conduits for upward fluid migration, thus producing high heat flow. The low P-wave velocities I identified above the chimneys and fault zones in my study area suggest that upward migration of fluid via fault system could be enhanced by high pore pressure fluids or gas (*Tsuji et al.,* 2014).

2-7 Conclusions

I have demonstrated that faults, chimneys, and slump deposits play an important role in the upward migration of gas in the study area and control the distributions of gas-hydrate and free-gas accumulations. My high-resolution P-wave velocity modeling provided clear evidence that gas hydrate and free gas are widely distributed in the study area and possibly in the wider Sanriku-Oki forearc basin. My heat-flow modeling based on the depth of the BSR provided strong evidence for upward fluid migration in the study area. My key findings are summarized below.

- I interpreted widespread zones of high P-wave velocities and low seismic amplitudes above the BSR to represent the presence of gas hydrate, and zones of P-wave velocities lower than 1500 m/s below the BSR to indicate the presence of free gas. High P-wave velocity of gas hydrate forming an effective hydrological seal could deflect upward migration of fluid to the Quaternary reservoir rock.
- Heat flow modeling showed that areas of high heat flow (30 to 35 mW/m^2) generally correspond to areas above the BSR with high concentrations of gas hydrate and to areas below the BSR where there are accumulations of free gas along the edges of slump structures in the intensely faulted western and northwestern parts of the study area, where there are also gas chimneys.
- Faults and chimneys likely provide pathways for upward gas migration, forming the gas-hydrate accumulations in the Quaternary sequence.

- I recognized free-gas accumulations within slump units; some of this gas likely migrated from the slumps to their edges via permeable and porous slump units and then upward to accumulate as gas pockets in strata below the BSR.

We have presented here the first application of high-resolution seismic velocity analysis in the Sanriku-Oki forearc basin that is not dependent on borehole velocity data. The resultant velocity and heat flow modeling allowed us to greatly improve our understanding of the geological processes leading to hydrocarbon accumulation in the complex tectonic environment of the plate subduction margin off northeastern Japan. The techniques we employed have considerable potential to contribute to the quantification of gas-hydrate and free-gas resources in other deep-water reservoirs on the eastern continental margin of Japan and at other plate subduction margins.

2-8 References

Ando, H. (2005), Geologic setting and stratigraphic correlation of the Cretaceous to Paleocene Yezo forearc basin in Northeast Japan. *Journal of the Japanese Association for Petroleum Technology*, *70*(1), 24-36.

Aoike, K. (Ed.), 2007. CDEX Laboratory Operation Report: CK06-06 D/V Chikyu Shakedown Cruise Offshore Shimokita: Yokohama (CDEX-JAMSTEC).

http://sio7.jamstec.go.jp/JAMSTEC-exp-report/902/CK06-06_CR.pdf

Arntsen, B., L. Wensaas, H. Løseth, and C. Hermanrud (2007), Seismic modeling of gas chimneys. *Geophysics*, *72*(5), SM251-SM259. https://doi.org/10.1190/1.2749570.

Ashi, J., H. Tokuyama, and A. Taira (2002), Distribution of methane hydrate BSRs and its implication for the prism growth in the Nankai Trough. *Marine Geology*, *187*(1-2), 177-191. https://doi.org/10.1016/S0025-3227(02)00265-7.

Bello, A., R. Heggland, and D. C. P. Peacock (2017), Pressure significance of gas chimneys. *Marine and Petroleum Geology*, *86*, 402–407. https://doi.org/10.1016/j.marpetgeo.2017.06.005.

Bredehoeft, J. D. and I. Papadopoulos (1965), Rates of vertical groundwater movement estimated form the earth's thermal profiles. *Water Resour Res* 1(2):325–328. https://doi.org/10.1029/WR001i002p00325.

Bünz, S., J. Mienert, M. Vanneste, and K. Andreassen (2005), Gas hydrates at the Storegga Slide: constraints from an analysis of multicomponent, wide-angle seismic data. *Geophysics*, 70 (5), B19–B34. https://doi.org/10.1190/1.2073887.

Chhun, C., A. Kioka, J. Jia, and T. Tsuji (2018), Characterization of hydrate and gas reservoirs in plate convergent margin by applying rock physics to high-resolution seismic velocity model. *Marine and Petroleum Geology*, *92*, 719–732. https://doi.org/10.1016/j.marpetgeo.2017.12.002.

Claypool, G. E., and I. R. Kaplan (1974), The origin and distribution of methane in marine sediments. *Natural gases in marine sediments* (pp. 99–139). *Springer*, Boston, MA.

Collett, T. S., and J. Ladd (2000), 19. Detection of gas hydrate with downhole logs and assessment of gas hydrate concentrations (saturations) and gas volumes on the Blake Ridge with electrically resistivity log data. *Proceedings of the Ocean Drilling Program, Scientific Results, Texas A&M University, College Station, TX, USA*, *164*.

Crutchley, G. J., K. F. Kroeger, I. A. Pecher, J. J. Mountjoy, and A. R. Gorman (2017), Gas Hydrate Formation Amid Submarine Canyon Incision: Investigations From New Zealand's Hikurangi Subduction Margin. *Geochemistry, Geophysics, Geosystems*, *18*(12), 4299-4316. https://doi.org/10.1002/2017GC007021.

Davis, E. E., R. D. Hyndman, and H. Villinger (1990), Rates of fluid expulsion across the Northern Cascadia Accretionary Prism: Constraints from new heat flow and multichannel seismic reflection data. *Journal of Geophysical Research: Solid Earth*, *95*(B6), 8869-8889. https://doi.org/10.1029/JB095iB06p08869.

Dickens, G. R., and M. S. Quinby-Hunt (1994), Methane hydrate stability in seawater. *Geophysical Research Letters*, *21*(19), 2115-2118. https://doi.org/10.1029/94GL01858.

Dickinson, W. R. (1995), Forearc basins, in Busby C.J., and Ingersoll, R.V., eds., Tectonics of Sedimentary Basins. Oxford, *Blackwell science*, 221–261.

Dix, C. H. (1955), Seismic velocities from surface measurements. *Geophysics*, 20 (1), 68–86. http://dx.doi.org/10.1190/1.1438126.

Eng, C., and T. Tsuji (2019), Influence of faults and slumping on hydrocarbon migration inferred from 3D seismic attributes: Sanriku-Oki forearc basin, northeast Japan. *Marine and Petroleum Geology*, *99*, 175-189. https://doi.org/10.1016/j.marpetgeo.2018.10.013.

Faure, K., J. Greinert, I.A. Pecher, I.J. Graham, G.J. Massoth, C.E. De Ronde, et al. (2006), Methane seepage and its relation to slumping and gas hydrate at the Hikurangi margin, New Zealand. *New Zealand Journal of Geology and Geophysics*, *49*(4), 503-516.

Fomel, S. (2009), Velocity analysis using AB semblance. *Geophysical Prospecting*. 57 (3), 311–321. http://dx.doi.org/10.1111/j.1365-2478.2008.00741.x.

Fomel, S., P. Sava, I. Vlad, Y. Liu, and V. Bashkardin (2013), Madagascar: Open-source software project for multidimensional data analysis and reproducible computational experiments. *Journal of Open Research Software*, *1*(1). http://doi.org/10.5334/jors.ag.

Fraser, D. R. A., A. R. Gorman, I. A. Pecher, G. J. Crutchley, and S. A. Henrys (2016), Gas hydrate accumulations related to focused fluid flow in the Pegasus Basin, southern Hikurangi Margin, New Zealand. *Marine and Petroleum Geology*, 77, 399–408. http://dx.doi.org/10.1016/j.marpetgeo.2016.06.025.

Fujii, T., K. Suzuki, T. Takayama, M. Tamaki, Y. Komatsu, Y. Konno, et al. (2015), Geological setting and characterization of a methane hydrate reservoir distributed at the first offshore production test site on the Daini-Atsumi Knoll in the eastern Nankai Trough, Japan. *Marine and Petroleum Geology*, 66, 310-322. http://dx.doi.org/10.1016/j.marpetgeo.2015.02.037.

Ganguly, N., G. D. Spence, N. R. Chapman, and R. D. Hyndman (2000), Heat flow variations from bottom simulating reflectors on the Cascadia margin. *Marine geology*, *164*(1-2), 53-68. https://doi.org/10.1016/S0025-3227(99)00126-7.

Gorman, A. R., W. S. Holbrook, M. J. Hornbach, K. L. Hackwith, D. Lizarralde, and I. Pecher (2002), Migration of methane gas through the hydrate stability zone in a low-flux hydrate province. *Geology*, *30*(4), 327-330. https://doi.org/10.1130/0091-7613(2002).

Grevemeyer, I., and H. Villinger (2001), Gas hydrate stability and the assessment of heat flow through continental margins. *Geophysical Journal International*, *145*(3), 647-660. https://doi.org/10.1046/j.0956-540x.2001.01404.x.

Gross, D., A. Bechtel, and G. J. Harrington (2015), Variability in coal facies as reflected by organic petrological and geochemical data in Cenozoic coal beds offshore Shimokita (Japan)-IODP Exp. 337. *International Journal of Coal Geology*, *152*, 63-79. https://doi.org/10.1016/j.coal.2015.10.007.

Han, W. C., L. Chen, C. S. Liu, C. Berndt, and W. C. Chi (2019), Seismic analysis of the gas hydrate system at Pointer Ridge offshore SW Taiwan. *Marine and Petroleum Geology*. https://doi.org/10.1016/j.marpetgeo.2019.04.028.

Hayes, D. E., S. S. Nissen, P. Buhl, J. Diebold, Y. Bochu, W. Zeng, and Y. Chen (1995), Throughgoing crustal faults along the northern margin of the South China Sea and their role in crustal extension. *Journal of Geophysical Research: Solid Earth*, *100*(B11), 22435-22446. https://doi.org/10.1029/95JB01867.

Henrys, S. A., S. Ellis, and C. Uruski (2003), Conductive heat flow variations from bottom-simulating reflectors on the Hikurangi margin, New Zealand. *Geophysical Research Letters*, *30*(2). https://doi.org/10.1029/2002GL015772.

Holbrook, W. S., H. Hoskins, W. T. Wood, R. A. Stephen, and D. Lizarralde (1996), Methane hydrate and free gas on the Blake Ridge from vertical seismic profiling. *Science*, *273*(5283), 1840-1843. https://doi.org/10.1126/science.273.5283.184.

Horozal, S., G. H. Lee, B. Y. Yi, D. G. Yoo, K. P. Park, H. Y. Lee, et al. (2009), Seismic indicators of gas hydrate and associated gas in the Ulleung Basin, East Sea (Japan Sea) and implications of heat flows derived from depths of the bottom-simulating reflector. *Marine Geology*, *258*(1-4), 126-138. https://doi.org/10.1016/j.margeo.2008.12.004.

Hovland, M., H. Løseth, P. A. Bjørkum, L. Wensaas, and B. Arntsen (1999), Seismic detection of shallow high pore pressure zones. *Offshore, Dec*, 94-96.

Hustoft, S., S. Bünz, J. Mienert, and S. Chand (2009), Gas hydrate reservoir and active methane venting province in sediments on <20 Ma young oceanic crust in the Fram Strait, offshore NW Svalbard. *Earth and Planetary Science Letters* 284 (1–2), 12–24. https://doi.org/10.1016/j.epsl.2009.03.038.

Hyndman, R. D., and G. D. Spence (1992), A seismic study of methane hydrate marine bottom simulating reflectors. *Journal of Geophysical Research: Solid Earth*, *97*(B5), 6683-6698. https://doi.org/10.1029/92JB00234.

Hyndman, R. D., and K. Wang (1993), Thermal constraints on the zone of major thrust earthquake failure: The Cascadia subduction zone. *Journal of Geophysical Research: Solid Earth*, *98*(B2), 2039-2060. https://doi.org/10.1029/92JB02279.

Hyndman, R. D., K. Wang, T. Yuan, and G. D. Spence (1993), Tectonic sediment thickening, fluid expulsion, and the thermal regime of subduction zone accretionary prisms: The Cascadia margin off Vancouver Island. *Journal of Geophysical Research: Solid Earth*, *98*(B12), 21865-21876. https://doi.org/10.1029/93JB02391.

Hyndman, R. D., G. D. Spence, R. Chapman, M. Riedel, and R. N. Edwards (2001), Geophysical studies of marine gas hydrate in northern Cascadia. *Washington DC American Geophysical Union Geophysical Monograph Series*, *124*, 273-295. https://doi.org/10.1029/GM124p0273.

Inagaki, F., K. U. Hinrichs and Y. Kubo and the Expedition 337 Scientists (2012), Deep coalbed biosphere off Shimokita: microbial processes and hydrocarbon system associated with deeply buried coalbed in the ocean. IODP Preliminary Report. https://doi.org/10.2204/iodp.pr.337.2012.

Itoh, Y., O. Takano, S. Kusumoto, and M. Tamaki (2014), Mechanism of long-standing Cenozoic basin formation in central Hokkaido: an integrated basin study on an oblique convergent margin. *Progress in Earth and Planetary Science*, *1*(1), 6. https://doi.org/10.1186/2197-4284-1-6.

Iván, V. C., T. Umberta, and V. M. Lucía (2017), Gas hydrate and free gas concentrations in two sites inside the Chilean margin (Itata and Valdivia offshores). *Energies*, *10*(12), 2154. https://doi.org/10.3390/en10122154.

Japan Oil, Gas and Metals National Corporation (JOGMEC) (2010), Report on the Sanriku 3D seismic data processing. (In Japanese).

Jones, A. T., J. Greinert, D. A. Bowden, I. Klaucke, C. J. Petersen, G. L. Netzeband, and W. Weinrebe (2010), Acoustic and visual characterisation of methane-rich seabed seeps at Omakere Ridge on the Hikurangi Margin, New Zealand. *Marine Geology*, *272*(1-4), 154-169. https://doi.org/10.1016/j.margeo.2009.03.008.

Judd, A., and M. Hovland (2009), Seabed fluid flow: the impact on geology, biology and the marine environment. Cambridge University Press.

Ker, S., Y. Thomas, V. Riboulot, N. Sultan, C. Bernard, C. Scalabrin., et al. (2019), Anomalously deep BSR related to a transient state of the gas hydrate system in the western Black Sea. *Geochemistry, Geophysics, Geosystems*, *20*(1), 442-459. https://doi.org/10.1029/2018GC007861

Kimura, G., S. Hina, Y. Hamada, J. Kameda, T. Tsuji, M. Kinoshita, and A. Yamaguchi (2012), Runaway slip to the trench due to rupture of highly pressurized megathrust beneath the middle trench slope: The tsunamigenesis of the 2011 Tohoku earthquake off the east coast of northern Japan, *Earth and Planetary Science Letters*, 339-340, 32-45, https://doi.org/10.1016/j.epsl.2012.04.002.

Kinoshita, M., G. F. Moore, and Y. N. Kido (2011), Heat flow estimated from BSR and IODP borehole data: Implication of recent uplift and erosion of the imbricate thrust zone in the Nankai Trough off Kumano. *Geochemistry, Geophysics, Geosystems*, *12*(9). https://doi.org/10.1029/2011gc003609.

Korenaga, J., W. S. Holbrook, S. C. Singh, and T. A. Minshull (1997), Natural gas hydrates on the southeast US margin: Constraints from full waveform and travel time inversions of wide-angle seismic data. *Journal of Geophysical Research: Solid Earth*, *102*(B7), 15345-15365. https://doi.org/10.1029/97JB00725.

Kvenvolden, K. A. (1993), Gas hydrates—geological perspective and global change. *Reviews of geophysics*, *31*(2), 173-187. https://doi.org/10.1029/93RG00268.

Kvenvolden, K. A., and M. A. McMenamin (1980), Hydrates of natural gas: a review of their geologic occurrence.

Li, H.L., T. He, and G.D. Spence (2014), North Cascadia heat flux and fluid flow gas hydrates: Modeling 3-D topographic effects. *Journal of Geophysical Research: Solid Earth*, 119, 99–115, https://doi.org/10.1002/2013JB010101.

Li, L., X. Lei, X. Zhang, and G. Zhang (2012), Heat flow derived from BSR and its implications for gas hydrate stability zone in Shenhu Area of northern South China Sea. *Marine Geophysical Research*, *33*(1), 77-87. https://doi.org/10.1007/s11001-012-9147-3.

Li, L., X. Lei, X. Zhang, and Z. Sha (2013), Gas hydrate and associated free gas in the Dongsha Area of northern South China Sea. *Marine and Petroleum Geology*, *39*(1), 92-101. https://doi.org/10.1016/j.marpetgeo.2012.09.007

Li, Y. M., X. H. Luo, X. Xu, X. Q. Yang, and X. B. Shi (2010), Seafloor in-situ heat flow measurements in the deep-water area of the northern slope, South China Sea. *Diqiu Wuli Xuebao*, *53*(9), 2161-2170. https://doi.org/10.1002/cjg2.1547.

Maekawa, T., S. Itoh, S. Sakata, S. Igari, and N. Imai (1995), Pressure and temperature conditions for methane hydrate dissociation in sodium chloride solutions, Geochem. J. 29, 325–329.

Martin, K. M., S. P. Gulick, N. L. Bangs, G. F. Moore, J. Ashi, J. O. Park, et al. (2010), Possible strain partitioning structure between the Kumano fore-arc basin and the slope of the Nankai Trough accretionary prism. *Geochemistry, Geophysics, Geosystems*, *11*(5). https://doi.org/10.1029/2009GC002668.

Mienert, J., and J. Posewang (1999), Evidence of shallow-and deep-water gas hydrate destabilizations in North Atlantic polar continental margin sediments. *Geo-Marine Letters*, *19*(1-2), 143-149. https://doi.org/10.1007/s003670050101.

Miyakawa, A., S. Saito, Y. Yamada, H. Tomaru, M. Kinoshita, and T. Tsuji (2014), Gas hydrate saturation at S ite C 0002, IODP E xpeditions 314 and 315, in the K umano B asin, N ankai trough. *Island Arc*, *23*(2), 142-156. https://doi.org/10.1111/iar.12064.

Neidell, N. S., and M. T. Taner (1971). Semblance and other coherency measures for multichannel data. Geophysics, 36(3), 482-497.

Oda, H. (2003), Cretaceous and paleogene coals in Japan as source rocks of natural gas and petrolem. *AAPG international conference* (pp. 1-5).

Ohde, A., H. Otsuka, A. Kioka, and J. Ashi (2018), Distribution and depth of bottom-simulating reflectors in the Nankai subduction margin. *Earth, Planets and Space*, *70*(1), 60. https://doi.org/10.1186/s40623-018-0833-5.

Osawa, M. (2002), Structure, tectonic evolution and gas exploration potential of offshore Sanriku and Hidaka provinces, Pacific Ocean, off northern Honshu and Hokkaido, Japan. *Journal of the Japanese association for petroleum technology*, *67*, 38-49.

Oyama, A., and S. Masutani (2017), A review of the methane hydrate program in Japan. *Energies*, *10*(10), 1447. https://doi.org/10.3390/en10101447.

Pecher, I. A., N. Kukowski, C. Huebscher, J. Greinert, and J. Bialas (2001), The link between bottom-simulating reflections and methane flux into the gas hydrate stability zone new evidence from Lima Basin, Peru Margin. *Earth and Planetary Science Letters*. 185, 343–354. https://doi.org/10.1016/S0012-821X(00)00376-9.

Pecher, I. A., S. A. Henrys, S. Ellis, S. M. Chiswell, and N. Kukowski (2005). Erosion of the seafloor at the top of the gas hydrate stability zone on the Hikurangi Margin, New Zealand. *Geophysical Research Letters*, *32*(24).

Pecher, I. A., T. A. Minshull, S. C. Singh, and R. von Huene (1996), Velocity structure of a bottom simulating reflector offshore Peru: Results from full waveform inversion. *Earth and Planetary Science Letters*, *139*(3-4), 459-469. https://doi.org/10.1016/0012-821X(95)00242-5.

Phrampus, B. J., R. N. Harris, and A. M. Tréhu (2017), Heat flow bounds over the Cascadia margin derived from bottom simulating reflectors and implications for thermal models of subduction. *Geochemistry, Geophysics, Geosystems*, *18*(9), 3309-3326. https://doi.org/10.1002/2017GC007077.

Plaza-Faverola, A., Westbrook, G. K., Ker, S., Exley, R. J., Gailler, A., Minshull, T. A., & Broto, K. (2010). Evidence from three-dimensional seismic tomography for a substantial accumulation of gas hydrate in a fluid-escape chimney in the Nyegga pockmark field, offshore Norway. *Journal of Geophysical Research: Solid Earth*, *115*(B8).

https://doi.org/10.1029/2009JB007078

Plaza-Faverola, A., S. Bünz, J. E. Johnson, S. Chand, J. Knies, J. Mienert, and P. Franek (2015), Role of tectonic stress in seepage evolution along the gas hydrate-charged Vestnesa Ridge, Fram Strait. *Geophysical Research Letters*, *42*(3), 733-742. https://doi.org/10.1002/2014GL062474

Plaza-Faverola, A., S. Vadakkepuliyambatta, W. L. Hong, J. Mienert, S. Bünz, S. Chand, and J. Greinert (2017), Bottom-simulating reflector dynamics at Arctic thermogenic gas provinces: An example from Vestnesa Ridge, offshore west Svalbard. *Journal of*

Geophysical Research: Solid Earth, *122*(6), 4089-4105. https://doi.org/10.1002/2016JB013761

Poort, J., O. M. Khlystov, L. Naudts, A. D. Duchkov, H. Shoji, S. Y. Nishio, et al. (2012), Thermal anomalies associated with shallow gas hydrates in the K-2 mud volcano, Lake Baikal. *Geo-Marine Letters*, *32*(5-6), 407-417. https://doi.org/10.1007/s00367-012-0292-0.

Rao, Y. H., C. Subrahmanyam, S. R. Sharma, A. A. Rastogi, and B. Deka (2001), Estimates of geothermal gradients and heat flow from BSRs along the Western Continental Margin of India. *Geophysical research letters*, *28*(2), 355-358. https://doi.org/10.1029/2000GL008528.

Riedel, M., A. M. Tréhu, and G. D. Spence (2010), Characterizing the thermal regime of cold vents at the northern Cascadia margin from bottom-simulating reflector distributions, heat-probe measurements and borehole temperature data. *Marine Geophysical Researches*, *31*(1-2), 1-16. https://doi.org/10.1007/s11001-010-9080-2.

Shipley, T. H., M. H. Houston, R. T. Buffler, F. J. Shaub, K. J. McMillen, J. W. Ladd, and J. L. Worzel (1979). Seismic evidence for widespread possible gas hydrate horizons on continental slopes and rises. *AAPG bulletin*, *63*(12), 2204-2213.

Singh, S. C., T. A. Minshull, and G. D. Spence (1993), Velocity structure of a gas hydrate reflector. *Science*, *260*(5105), 204-207. https://doi.org/10.1126/science.260.5105.204.

Singhroha, S., S. Chand, and S. Bünz, S (2019), Constraints on gas hydrate distribution and morphology in Vestnesa Ridge, W-Svalbard margin using multicomponent ocean-bottom seismic data. *Journal of Geophysical Research: Solid Earth*. https://doi.org/10.1029/2018JB016574.

Sloan Jr, E. D., and C. Koh (2007), *Clathrate hydrates of natural gases*. CRC press. https://doi.org/10.1201/9781420008494.

Spence, G. D., R. R. Haacke, and R. D. Hyndman (2010), Seismic indicators of natural gas hydrate and underlying free gas. In *Geophysical Characterization of Gas Hydrates* (pp. 39-71). Society of Exploration Geophysicists. https://doi.org/10.1190/1.9781560802197.ch4

Takano, O. (2017), Intermittent formation, sedimentation and deformation history of Cenozoic forearc basins along the Northwestern Pacific Margins as an indicator of tectonic scenarios. In *Dynamics of Arc Migration and Amalgamation-Architectural*

Examples from the NW Pacific Margin. IntechOpen. https://doi.org/10.5772/intechopen. 68290.

Takano, O., Y. Itoh, and S. Kusumoto (2013), Variation in forearc basin configuration and basin-filling depositional systems as a function of trench slope break development and strike-slip movement: Examples from the Cenozoic Ishikari–Sanriku-Oki and Tokai-Oki–Kumano-Nada forearc basins, Japan. In *Mechanism of sedimentary basin formation-multidisciplinary approach on active plate margins*. InTech. https://doi.org/ 10.5772/56751.

Takano, O., and T. Tsuji (2017), Fluvial to bay sequence stratigraphy and seismic facies of the Cretaceous to Paleogene successions in the MITI Sanriku-oki well and the vicinities, the Sanriku-oki forearc basin, northeast Japan. *Island Arc*, 26(4), https://doi.org/10.1111/iar.12184.

Taladay, K. B., and F. M. Gregory (2015), Concentrated gas hydrate deposits in the Kumano Forearc Basin, Nankai Trough, Japan. *Center for Natural Gas and Oil*, *412*(5), 386-7614.

Taladay, K., B. Boston, and G. Moore (2017), Gas-in-place estimate for potential gas hydrate concentrated zone in the Kumano Basin, Nankai Trough Forearc, Japan. *Energies*, *10*(10), 1552. https://doi.org/10.3390/en10101552.

Taner, M. T., and F. Koehler (1969). Velocity spectra—Digital computer derivation applications of velocity functions. Geophysics, 34(6), 859-881.

Tanikawa, W., O. Tadai, S. Morita, W. Lin, Y. Yamada, Y. Sanada, et al. (2016), Thermal properties and thermal structure in the deep-water coalbed basin off the Shimokita Peninsula, Japan. *Marine and Petroleum Geology*, *73*, 445-461. ttps://doi.org/10.1016/j.marpetgeo.2016.03.006.

Tanioka, Y., and K. Sataka (1996), Fault parameters of the 1896 Sanriku tsunami earthquake estimated from tsunami numerical modeling. *Geophysical Research Letters*, *23*(13), 1549-1552. https://doi.org/10.1029/96GL01479.

Tinivella, U., and F. Accaino (2000), Compressional velocity structure and Poisson's ratio in marine sediments with gas hydrate and free gas by inversion of reflected and refracted seismic data (South Shetland Islands, Antarctica). *Marine Geology*, *164*(1-2), 13-27. https://doi.org/10.1016/S0025-3227(99)00123-1.

Townend, J. (1997), Estimates of conductive heat flow through bottom-simulating reflectors on the Hikurangi and southwest Fiordland continental margins, New Zealand. *Marine Geology*, *141*(1-4), 209-220. https://doi.org/10.1016/S0025-3227(97)00073-X.

Tsuji, T., J. Ashi, M. Strasser, and G. Kimura (2015), Identification of the static backstop and its influence on the evolution of the accretionary prism in the Nankai Trough, Earth and Planetary Science Letters, 431, 15-25. https://doi.org/10.1016/j.epsl.2015.09.011.

Tsuji, T., J. Ashi, and Y. Ikeda (2014), Strike-slip motion of a mega-splay fault system in the Nankai oblique subduction zone. *Earth, Planets and Space*, *66*(1), 120. https://doi.org/10.1186/1880-5981-66-120.

Tsuji, T., K. Kawamura, T. Kanamatsu, T. Kasaya, K. Fujikura, Y. Ito, et al. (2013), Extension of continental crust by anelastic deformation during the 2011 Tohoku-oki earthquake: The role of extensional faulting in the generation of a great tsunami, *Earth and Planetary Science Letters,* 364, 44-58, https://doi.org/10.1016/j.epsl.2012.12.038.

Tsuji, T., K. Takai, H. Oiwane, Y. Nakamura, Y. Masaki, H. Kumagai, et al. (2012). Hydrothermal fluid flow system around the Iheya North Knoll in the mid-Okinawa trough based on seismic reflection data. *Journal of Volcanology and Geothermal Research*, 41–50. https://doi.org/10.1016/j.jvolgeores.2011.11.007.

Tsuji, T., H. Tokuyama, P. Costa Pisani, and G. Moore (2008), Effective stress and pore pressure in the Nankai accretionary prism off the Muroto Peninsula, southwestern Japan. *Journal of Geophysical Research: Solid Earth*, 113, B11401, https://doi.org/doi:10.1029/2007JB005002.

Vanneste, M., S. Guidard, and J. Mienert (2005), Bottom-simulating reflections and geothermal gradients across the western Svalbard margin. *Terra Nova*, *17*(6), 510-516. https://doi.org/10.1111/j.1365-3121.2005.00643.x.

Vargas-Cordero, I., U. Tinivella, L. Villar-Muñoz, and J. Bento (2018), High Gas Hydrate and Free Gas Concentrations: An Explanation for Seeps Offshore South Mocha Island. *Energies*, *11*(11), 3062. *Energies* 2018, *11*(11), 3062. https://doi.org/10.3390/en11113062.

Villinger, H. W., M. G. Langseth, H. M. Gröschel-Becker, and A. T. Fisher (1994). Estimating in-situ thermal conductivity from log data, *Proc. ODP Init. Repts,* 139, 545–552

Waite, W. F., J. C. Santamarina, D. D. Cortes, B. Dugan, D. N. Espinoza, J. Germaine, et al. (2009), Physical properties of hydrate-bearing sediments. *Reviews of geophysics*, *47*(4). http:// dx.doi.org/10.1029/2008RG000279.

Wang, J., P. Jaiswal, S. S. Haines, P. E. Hart, and S. Wu (2018), Gas hydrate quantification using full-waveform inversion of sparse ocean-bottom seismic data: A case study from Green Canyon Block 955, Gulf of Mexico. *Geophysics*, *83*(4), B167-B181. https://doi.org/10.1190/geo2017-0414.1

White, R. S (1979), Gas hydrate layers trapping free gas in the Gulf of Oman. *Earth and Planetary Science Letters*, *42*(1), 114-120. https://doi.org/10.1016/0012-821X(79)90196-1.

Xu, W., and L. N. Germanovich (2006), Excess pore pressure resulting from methane hydrate dissociation in marine sediments: A theoretical approach. *Journal of Geophysical Research: Solid Earth*, *111*(B1). https://doi.org/10.1029/2004JB003600.

Xu, X., Z. Wan, X. Wang, Y. Sun, and B. Xia (2016), The characteristics of heat flow in the Shenhu gas hydrate drilling area, northern South China Sea. *Marine Geophysical Research*, *37*(4), 325-335. https://doi.org/10.1007/s11001-016-9299-7.

Yagishita, K., and O. Takano (2005), Recognition of a Floodplain within Braid Delta Deposits of the Oligocene Minato Formation, North-East Japan: Fine Deposits Correlated with Transgression. *Fluvial Sedimentology VII*, 557-568. https://doi.org/10.1002/9781444304350.ch29.

Yamano, M., S. Uyeda, Y. Aoki, and T. H. Shipley (1982), Estimates of heat flow derived from gas hydrates. *Geology*, *10*(7), 339-343. https://doi.org/10.1130/0091-7613(1982)10.CO;2.

Yamano, M., M. Kinoshita, and S. Goto (2008), High heat flow anomalies on an old oceanic plate observed seaward of the Japan Trench. *International Journal of Earth Sciences*, *97*(2), 345-352. https://doi.org/10.1007/s00531-007-0280-1.

Yan, P., H. Deng, and H. Liu (2006), The geological structure and prospect of gas hydrate over the Dongsha Slope, South China Sea. *TAO: Terrestrial, Atmospheric and Oceanic Sciences*, *17*(4), 645. https://doi.org/10.3319/TAO.2006.17.4.645(GH).

Yessalina, S., and N. Suzuki (2005), Occurrences of sesqui-, di-, and triterpenoid hydrocarbons in the Tertiary oils and sediments from the Pacific side of Japan. *Researches in organic geochemistry*, *20*, 39-47.

Chapter 3

Grid-search inversion for pore geometry and grain elastic moduli

3-1 Introduction

Information about the chemical composition, physical state and structure of the Earth's interior is derived from seismic data. Understanding and interpretation of these seismic data are constrained by extrapolation of laboratory-measured seismic properties of rocks thought to exist in a given geological and physical environment. The elastic moduli and pore geometry provide the most vital parameterization to extract the information of the composition and structure of rock in the Earth's interior (Yu et al., 2016). The elastic moduli of rocks depend on the mineral compositions, porosity types, and pore geometry (e.g., crack aspect ratio), as well as elastic moduli of pore fluids (Potter et al., 1996; Carlson, 2010; Tsuji et al., 2014). The degree and type of hydrothermal alteration, the formation of secondary alteration and stage of fracturing all critically influence the seismic velocity (Cerney and Carlson, 1999; Wilkens et al., 1991; Tsuji and Iturrino, 2008). The ratio of *P*-wave velocity *Vp* to *S*-wave velocity *Vs* (*Vp/Vs*) can be used effectively to interpret geophysical field data in terms of both structure and lithology (e.g., Eng et al., 2017).

The variation of pore geometry (crack aspect ratio) within a rock is a key factor in defining reservoir heterogeneity, as it affects the complex migration pathways for recharge and discharge of pore fluids (e.g., Tsuji et al., 2012). Because the change in velocity with effective pressure is related to the degree of micro-crack closure, I can estimate crack aspect ratio from the relationship between seismic velocities and effective pressure derived from laboratory experiments (Ludwig et al., 1998; Tsuji and Iturrino, 2008; Wilkens et al., 1991).

However, these experiments are always time consuming and difficult to perform for many samples.

Here, I propose an inversion method to estimate grain elastic moduli and crack aspect ratio from *P*-wave velocity measurements of various types of rocks. In my inversion, I used Differential Effective Medium (DEM) theory to calculate the velocity–porosity relationships. My approach is easy to apply because it can be applied for physical properties measured at atmospheric pressure and surface temperature without changing pressure. I first apply my proposed inversion to synthetic data, and demonstrate the feasibility of estimating elastic moduli and pore geometries. Then, I apply my proposed approach to natural rock samples from hydrothermal ore deposits and oceanic basalts. The pore space of these geologic materials could be modelled by cracks (i.e., using a crack inclusion model).

3-2 Methods

To estimate aspect ratio and grain elastic moduli from the *P*-wave velocity–porosity relationship, I propose a grid search inversion using the DEM theory. The flow of my proposed inversion is illustrated in Figure 3-1. The details of each method are described as the following sections.

3-2-1 Differential Effective Medium Theory

The DEM theory models two-phase composites by incrementally adding inclusions of one phase (phase 2) to the matrix phase (phase 1) (Cleary et al., 1980; Mavko et al., 1998; Norris, 1985; Berryman et al., 2002; Tsuji et al., 2014; Li and Zhang, 2010). The matrix starts as phase 1 (when the concentration of phase 2 is zero) and is changed at each step as a new increment of phase 2 material is added. I assumed that the inclusion phase is water. Although an effective medium theory (using a crack-based model) is usually suitable for low-porosity

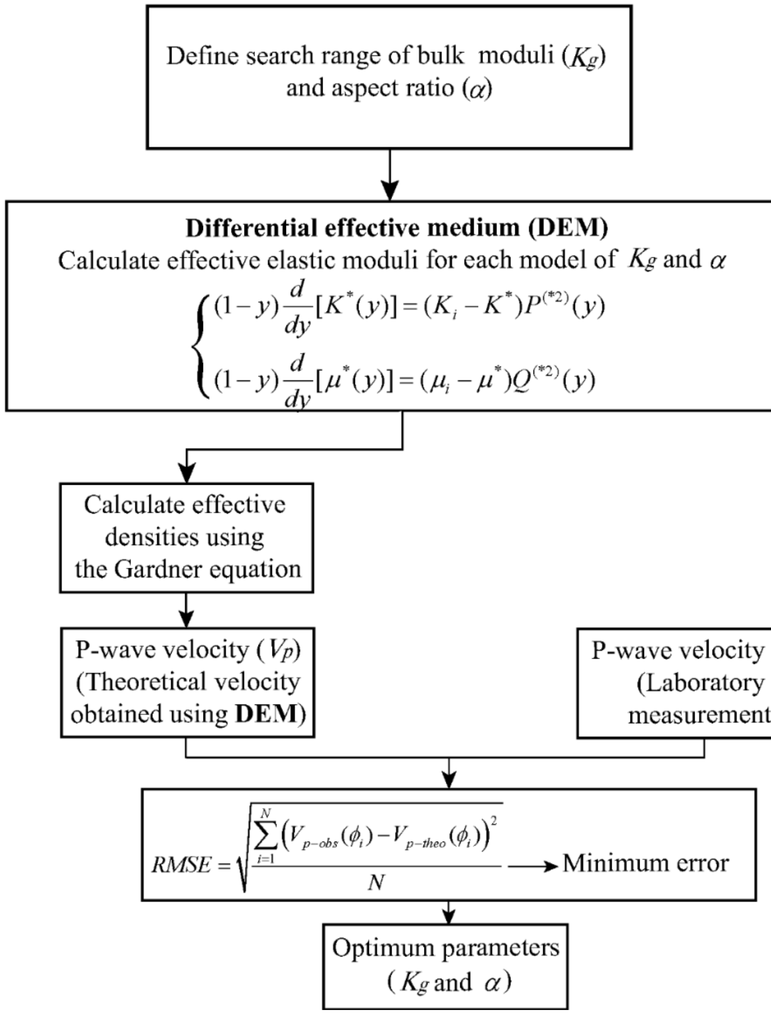

Figure 3-1. *Procedure for estimating grain elastic moduli and crack aspect ratio using grid search inversion with DEM.*

materials, DEM theory can be applied to relatively high-porosity materials, compared to other effective medium theories such as Kuster-Toksoz (1979) theory (Norris, 1985; Berge et al., 1992; Xu and White, 1995). The effective moduli depend on not only the final volume fractions of the constituents but also the order in which the incremental additions are made (Mavko et al., 1998). DEM theory requires the assumption of isolated cracks with respect to fluid flow (Mavko et al., 1998).

In DEM theory, the coupled system of ordinary differential equations is:

$$(1-y)\frac{d}{dy}[K^*(y)] = (K_i - K^*)P^{(*2)}(y) \tag{3-1}$$

$$(1-y)\frac{d}{dy}[\mu^*(y)] = (\mu_i - \mu^*)Q^{(*2)}(y) \tag{3-2}$$

where K^* and μ^* are the effective bulk and shear moduli, respectively. K_i and μ_i are the bulk and shear moduli of the incrementally added inclusion (phase 2), and y is the concentration of phase 2. In this study, I assume water to be the pore-filling medium. $P^{(*2)}$ and $Q^{(*2)}$ are geometric factors for penny-shaped cracks, considered to be randomly distributed (Mavko et al., 1998). To calculate effective bulk and shear moduli, I numerically solve Equations 3-1 and 3-2 using a Runge-Kutta scheme (see Appendix for details).

3-2-2 Grid Search Inversion

To estimate the grain elastic moduli and crack aspect ratio α from velocity–porosity relationship derived from laboratory measurement, I performed a grid search inversion using DEM theory. I calculated the root mean square error (*RMSE*) between effective *P*-wave velocities at each porosity, computed by DEM theory ($V_{p\text{-}theo}$) and those from laboratory data ($V_{p\text{-}obs}$). The *RMSE* was defined as:

$$RMSE(K_g, \alpha) = \sqrt{\frac{\sum_{i=1}^{N}(V_{p-obs}(\emptyset_i) - V_{p-theo}(\emptyset_i))^2}{N}} \tag{3-3}$$

where $\emptyset_i$ is the porosity for the *i*th sample and *N* is the number of samples. Here, *P*-wave velocities measured in three orthogonal directions on the cube-shaped samples were averaged, because the DEM theory I used in this study cannot be applied to an anisotropic medium. In addition to grain bulk moduli and crack aspect ratio, shear moduli and densities are required for the calculation of effective *P*-wave velocities using DEM theory. Estimation of grain shear moduli (or grain *S*-wave velocity) is difficult because I only acquired *P*-wave velocity data. Therefore, grain shear moduli were defined by assuming that the ratio between bulk and shear moduli was the same as the ratio between the elastic moduli of the grain mineral. Densities were defined using the Gardner equation (Gardner et al., 1974). I also assumed that rock samples from the same lithology would have cracks with the same aspect ratio. In my inversion, I searched the grain bulk modulus (K_g) and crack aspect ratio (α) space with a step size of 0.075 GPa and 0.001, respectively, and defined the model with the smallest *RMSE* as the best inverted model.

3-2-3 Evaluation of Proposed Grid-Search Method

I tested my proposed inversion with synthetic data in order to demonstrate the performance of my proposed method. In the synthetic test, I assumed the grain bulk modulus, shear modulus and aspect ratio to be 50 GPa, 50 GPa and 0.12, respectively. I calculated synthetic effective *P*-wave velocities by applying DEM calculations to 20 models with different porosity (red dots in Figure 3-2a). To consider a more realistic situation, I also introduced uncertainties into the synthetic data by generating 20 different sets of grain elastic moduli assuming a normal distribution around the true elastic moduli with the standard deviations (STD = 2.5 GPa and 5 GPa) (red dots in Figure 3-2b and 3-2c).

By applying the proposed grid search inversion process to these three cases, I were able to plot *RMSE* against K_g and α (Figure 3-3). As the uncertainty (STD) in the synthetic data increases, K_g and α with *RMSE* values close to the minimum *RMSE* (Emin) value are widely distributed around the true model. Nevertheless, the models with the minimum *RMSE* values (red symbols in Figure 3-3; Table 3-1) are close to the true K_g and α for all three cases, and the effective *P*-wave velocities and the porosity relationship constructed from the inverted models are consistent with the synthetic data (Figure 3-2). Estimation of K_g and α in my grid search inversion is straightforward because I have not observed secondary local minima in the distribution of *RMSE*. Thus, my synthetic test demonstrates that the proposed inversion can be effectively applied to seismic velocity data measured on rock samples with randomly oriented cracks and constant aspect ratio.

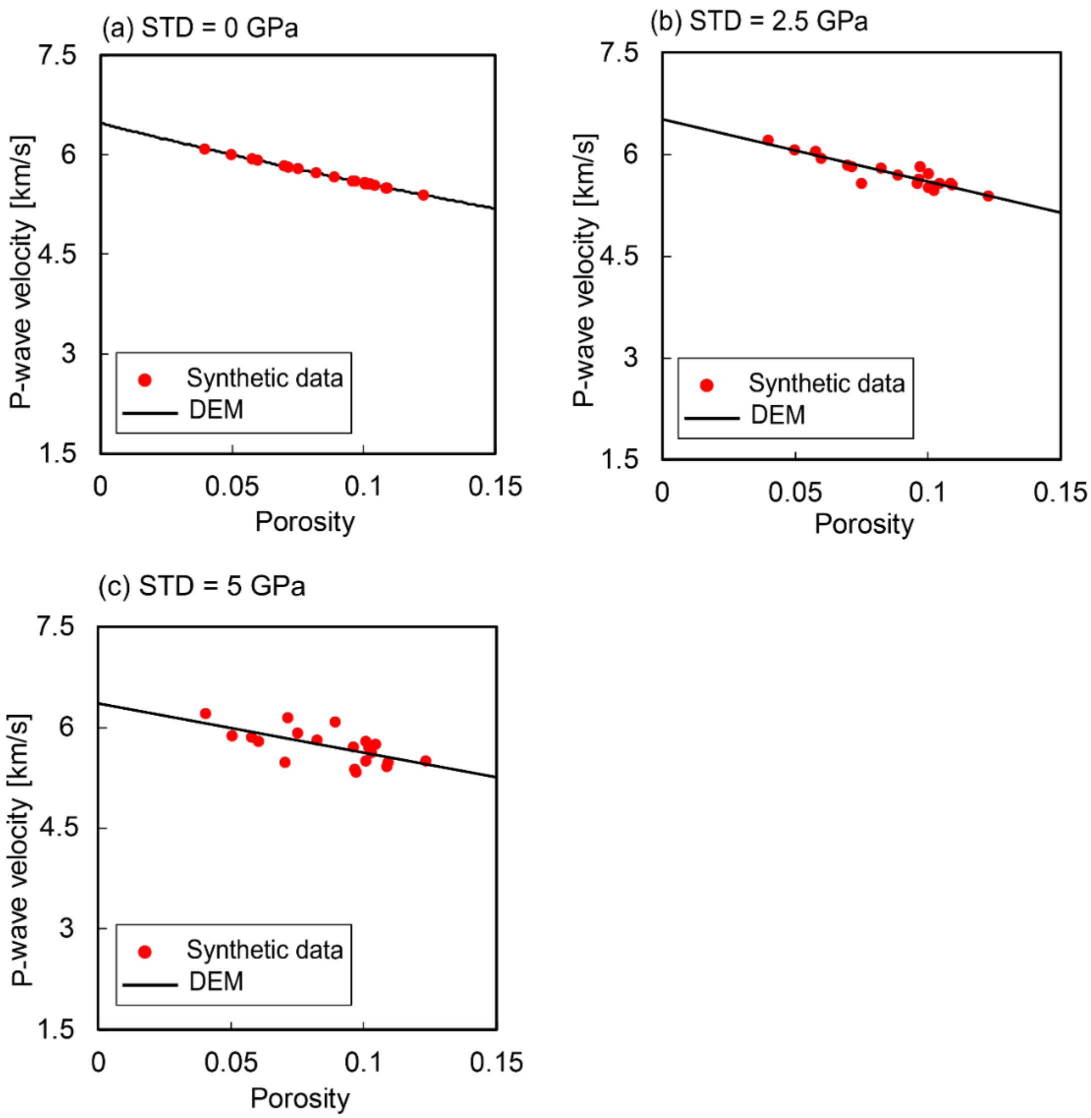

Figure 3-2. *Effective P-wave velocity–porosity relationship calculated from the inverted model (black line) for synthetic data with (a) STD = 0 GPa, (b) STD = 2.5 GPa, and (c) STD = 5 GPa. Red dots are synthetic data of effective P-wave velocity.*

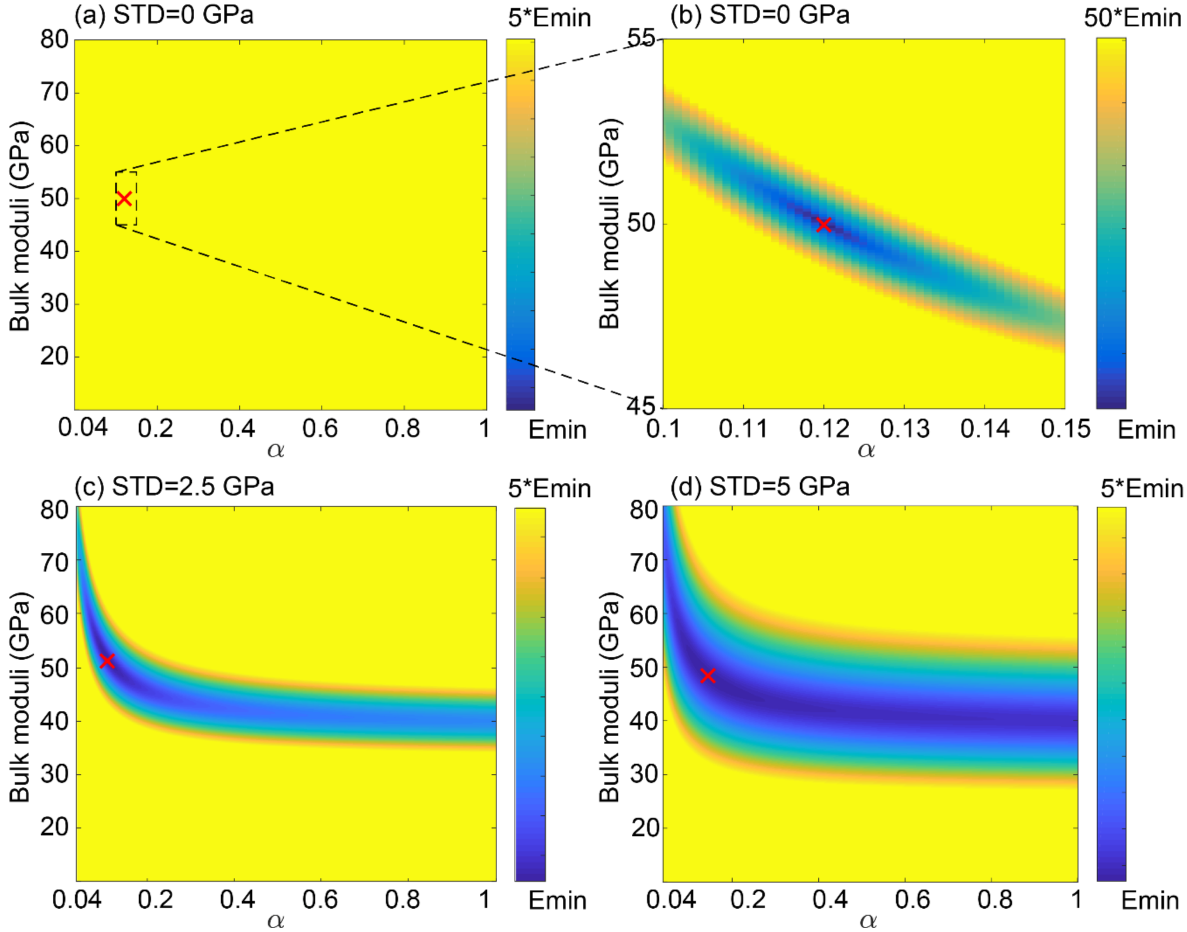

Figure 3-3. *Distribution of RMSE obtained by grid search inversion for synthetic data with (a) STD = 0 GPa, (c) STD = 2.5 GPa, and (d) STD = 5 GPa. (b) Enlarged view of panel (a). Red symbols represent the model parameters with the minimum RMSE values (Emin). The colour scale represents RMSE values scaled by Emin for each case.*

Table 3-1. *Grain elastic moduli (K_g) and crack aspect ratio (α) of the synthetic data (mean value of grain elastic moduli) and inversion results.*

	K_g (GPa)	α
True value	50	0.12
Inversion result (STD = 0 GPa)	49.975	0.12
Inversion result (STD = 2.5 GPa)	51.475	0.11
Inversion result (STD = 5 GPa)	48.4	0.144

3-3 Rock samples and Data

3-3-1 Ore deposits in the Okinawa Trough

Drilling Expedition 909 provided a good opportunity for subsurface rock sampling by coring drillholes in hydrothermal fields in the Okinawa Trough, southwest of Japan, in order to measure the physical properties of the hydrothermal field rocks (Figures 3-4a and 3-5). The Okinawa Trough is an active backarc basin extending for ~1200 km (Lee et al., 1980; Letouzey and Kimura, 1986), where the Philippine Sea Plate is subducting north-westward at ~6 cm/year beneath the Ryukyu arc (Seno, 1993). The Okinawa Trough was formed 6–9 Ma ago, with a second rifting phase active since 2 Ma (Letouzey and Kimura, 1986; Sibuet et al., 1998). The active hydrothermal fields in the Okinawa Trough are located in sediment–rich environments (Tsuji et al., 2012), in which hydrothermal alteration is generated as the result of subseafloor fluid-sediment interactions. The drilled cores of Expedition 909 of *D/V* Chikyu cruise showed layers of different lithologies (massive sulfide, pumice, and hydrothermal clay) with distinctive alteration zones containing various clay minerals. Vigorous venting of hydrothermal fluid from sulfide chimneys was investigated at ~1350m water depth (Ishibashi et al., 2014). Expedition 909 targeted sulfide mounds and a subseafloor sulfide zone that underlay the volcaniclastic sediments. A zone of sulfide mounds more than 20 m thick was discovered, lying from 30 m below the sea floor (mbsf) (METI, 2013).

Eight holes were drilled at the hydrothermal field. Altered clay, hydrothermal clay (silicified), hydrothermal sand, sulfide gravel and massive sulfide were the most abundant recovered lithologies. The cores recovered from this field are porous, and the pore structure can be observed visually. Thin cracks, circular or vesicular pores could be composed of complex, multistage fracturing and cavity linings. Drilled core samples from Sites C9025, C9028, C9026 and C9032 consisted of hemi-pelagic sediment, hydrothermal clay (pumiceous gravel), sulfide gravel, and hydrothermal clay (silicified) composed of quartz, clay minerals, muscovite and chlorite. Site C9027 is rich in massive sulfide and sulfide layers (Figure 3-5) composed of pyrite, sphalerite, galena, barite, and chalcopyrite. Thirty-one core samples were cut into cubic samples (2cm on each side) with faces orthogonal to the *x*-, *y*-, and *z*-axes of the core. Orientation of the axes was defined by taking the *z*-axis as pointing down the core axis.

The discrete *P*-wave measurement system used had a 230 kHz source frequency, and measured the traveltime of a *P*-wave through the sample. The wavelength (~1.2–3.3 cm) is larger than the cracks within the measured samples. *P*-wave velocities of 31 samples of massive sulfide, sulfide, and hydrothermal clay (silicified) were measured during the expedition, after being soaked for 24 hours in artificial seawater at atmospheric pressure and surface temperature conditions so that *P*-wave velocity measurements were not affected by the moisture content. For density and porosity measurements, each of the samples collected was weighed and then was placed in an oven for >24 hours at ~105°C. Dried samples were cooled in a desiccator at least 1 hour before dry mass and dry volume measurements. The volume of the dried samples was measured using a helium-displacement Quantachrome penta-pycnometer. Bulk density, grain density and porosity of each sample were measured after obtaining the volume of the dry samples.

The *P*-wave velocity values of silicified rocks range from 2.8 km/s to 5.7 km/s, and porosity values range from 9% to 25%. *P*-wave velocity values for sulfide samples range from 2.9 km/s to 5.8 km/s, and porosities range from 6% to 28%. *P*-wave velocities of massive sulfide, sulfide and silicified samples vary in wide porosity ranges (Figure 3-5), and there is no significant trend in index properties as functions of depth. The core of Site C9027 consisted mainly of sulfide-rich rocks. The core samples have the highest *P*-wave velocity (7.6 km/s) among drilled core samples, which is consistent with sulfide minerals, and porosities range from 8% to 25%. However, some massive sulfide samples at Site C9032 exhibited low *P*-wave velocities ~3.8 km/s with high porosity value of 38.8%.

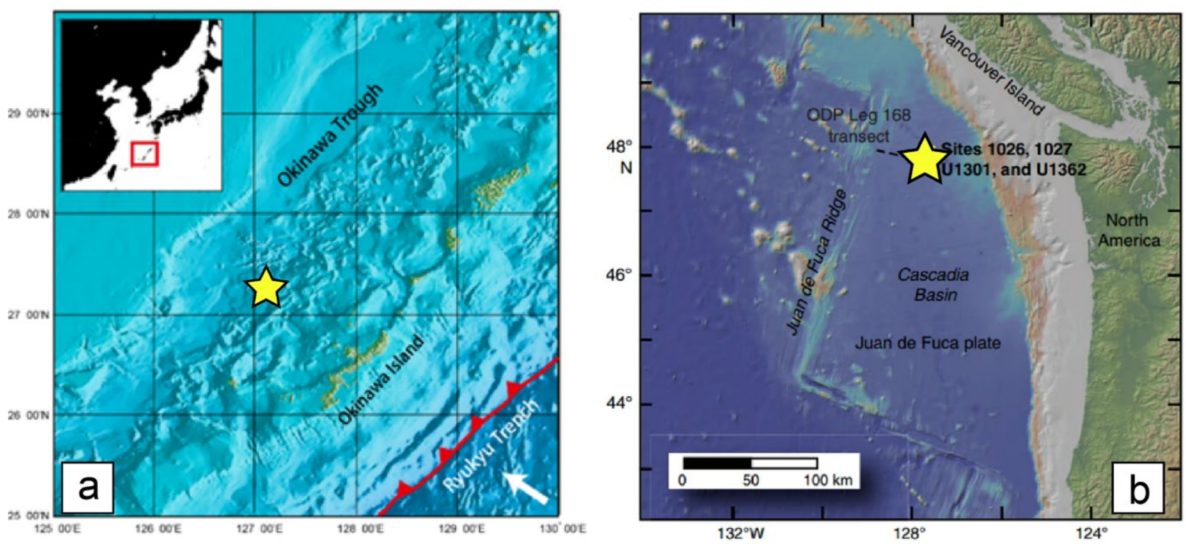

Figure 3-4. *Drilling sites in (a) the hydrothermal field in the Okinawa Trough (Tsuji et al., 2012) and (b) the Juan de Fuca Ridge (Fisher et al., 2011). Yellow stars represent the locations of drilling sites.*

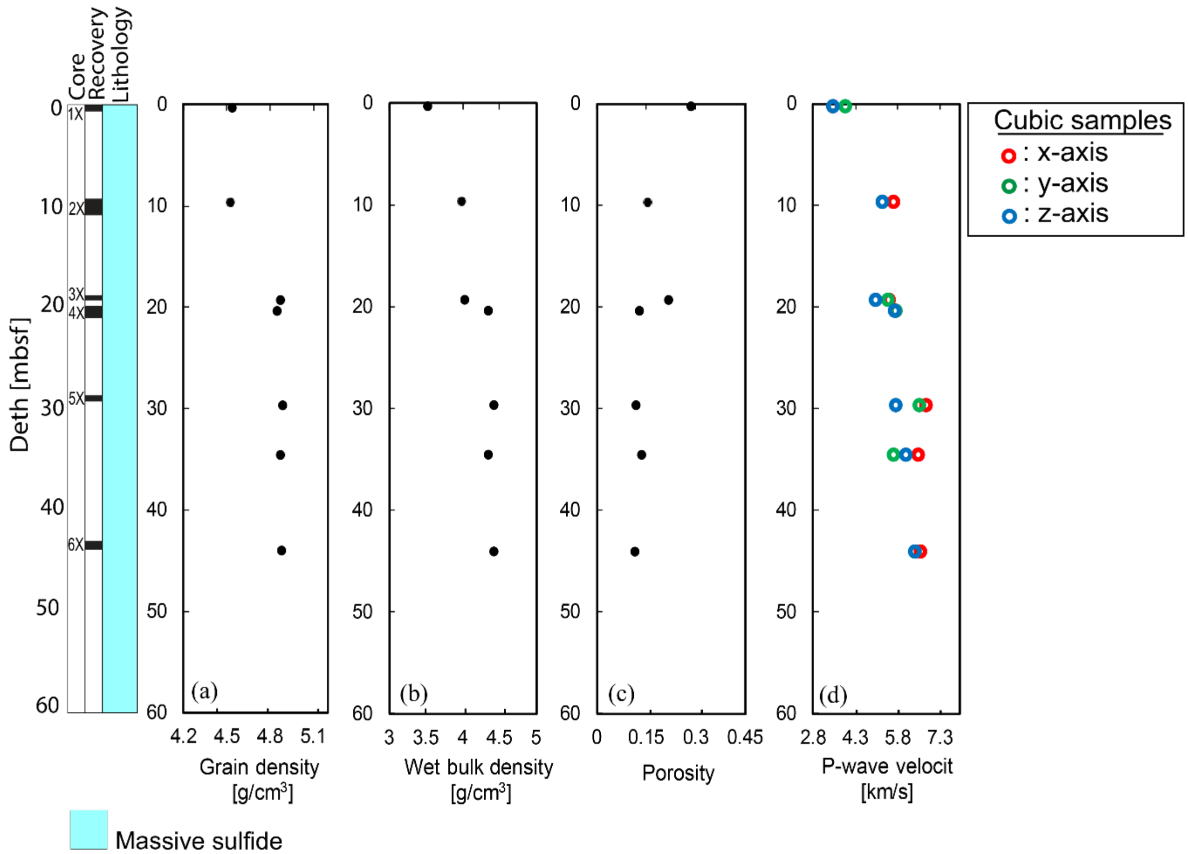

Figure 3-5. *Depth profile of (a) bulk density, (b) grain density, (c) porosity, and (d) P-wave velocity measured from cubic samples at atmospheric pressure, Cite C0927, the hydrothermal field in the Okinawa Trough.*

3-3-2 Basalt in Juan de Fuca Ridge

Integrated Ocean Drilling Program (IODP) Site U1362 (Fisher et al., 2011), located in the Juan de Fuca Ridge northwest region of North America, lies several hundred kilometres west of the North America continent (Giambalvo et al., 2000; Figures 3-4b and 3-6). The Juan de Fuca Ridge is located at the boundary between the Pacific plate and Juan de Fuca plate system (Neimovic et al., 2009). Fluid flow directions estimated from temperature measurements indicate that upper basaltic crust is naturally overpressured, but close to hydrostatic (Fisher et al., 1997). Fractures aligned with the ridge axis strongly control hydrothermal circulation (Fisher et al., 2011). Site U1362 is located on a buried basement ridge of 3.6 Ma old crust and ~100 km from the spreading centre. The basement at Site U1362 was cored from 346 to 496 mbsf with 44 m of core recovered.

Basaltic rocks are an abundant lithology in Hole U1362A. The recovered core consisted of (1) aphyric to moderately phyric pillow basalt, (2) aphyric to sparsely phyric sheet flows, and (3) sparsely to highly phyric basalt flows (Fisher et al., 2011; Tsuji et al., 2010). The pillow basalt varies from sparsely to highly phyric basalt. Plagioclase is the most abundant phase, with clinopyroxene and olivine also present in phyric samples. The mineralogy of the sheet flow ranges from aphyric to moderately phyric basalt. Overall, plagioclase, clinopyroxene and olivine are the most abundant minerals. The basalt flows have similar primary mineralogy as the pillow basalts and the sheet flow basalt (Fisher et al., 2011; Tsuji et al., 2010). The abundant secondary minerals are clay minerals varying from slight to completely altered. Several vesicular basalts were observed from Hole U1362A (Fisher et al., 2011).

Index properties of basaltic samples were measured on 70 discrete samples. As in the case of the Okinawa Trough, the cubic samples (2cm on each side) were cut from the core, with faces orthogonal to the x-, y-, and z-axes of the core. The measurement systems and conditions for *P*-wave velocity, density and porosity are similar to those in the Okinawa Trough.

The *P*-wave velocities measured in saturated conditions are ~200 m/s faster than those in dry conditions. Bulk density values of the basaltic rocks range from 2.2 to 2.9 t/m^3. Grain density values range from 2.4 to 3.0 t/m^3. Porosity and *P*-wave velocity range from 2.8% to 15.0% and from 4.5 to 6.0 km/s, respectively (Figure 3-6). The highest value of porosity was obtained from a highly altered sample with the lowest velocity.

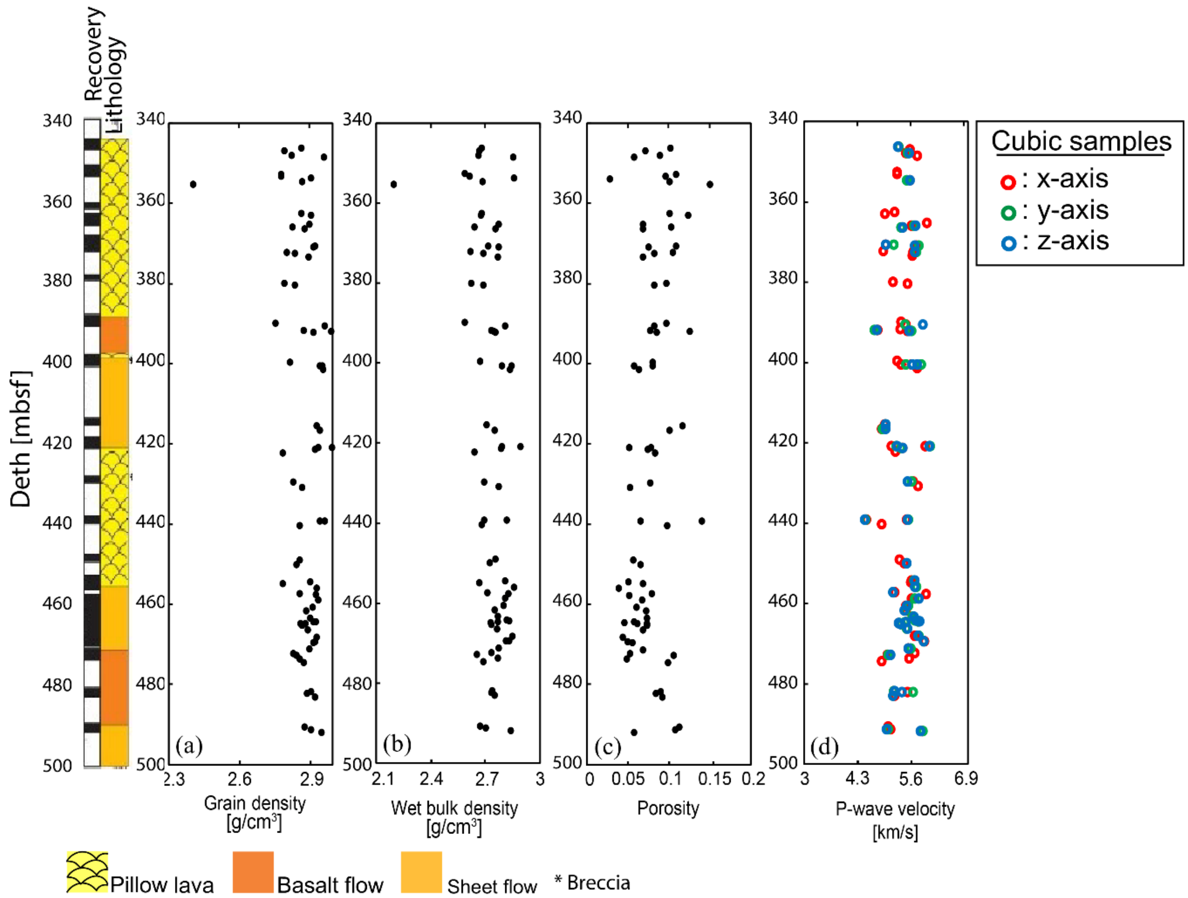

Figure 3-6. *Depth profile of (a) bulk density, (b) grain density, (c) porosity, and (d) P-wave velocity measured from cubic samples at atmospheric pressure (Fisher et al., 2011), Site U1362, the Juan de Fuca Ridge.*

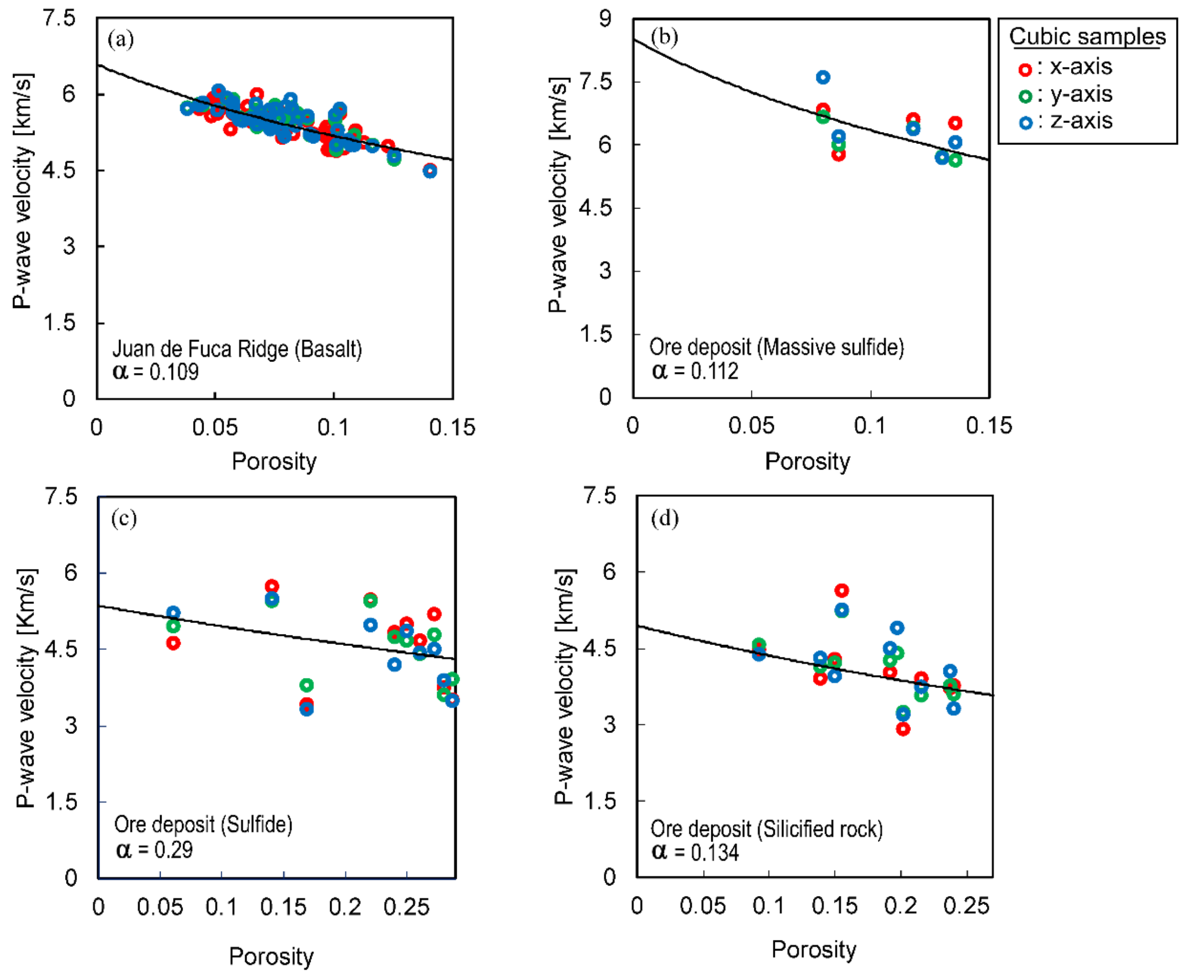

Figure 3-7. *The velocity–porosity relationships obtained using DEM for (a) basalts, (b) massive sulfide, (c) sulfide and (d) silicified rocks with aspect ratio (α) (lines). Red, green and blue circles represent cubic samples measured at atmospheric pressure for x, y and z directions, respectively.*

3-4 Results and Discussion

I applied the proposed inversion analysis to P-wave velocity data for massive sulfide, sulfide, silicified (Ore deposit, the Okinawa Trough), and basaltic samples (Juan de Fuca Ridge) shown in Figure 3-7. Since I could not estimate grain shear modulus directly, due to the lack of S-wave velocity measurements on the core samples, I defined the ratio between grain bulk moduli and shear moduli to be the same as the ratio between the elastic moduli of the mineral (Mavko et al., 1998) assuming that the grains of massive sulfide, sulfide, silicified rocks and basalt are mainly occupied by sphalerite, pyrrhotite, quartz and clay and plagioclase, respectively (Table 3-2).

The results of my grid search inversion clearly show different distributions of the *RMSE* values for each lithology (Figure 3-8). For basalt and massive sulfide, the shape of *RMSE* distribution around the minimum value is relatively sharp (Figures 3-8a and b). This indicates that K_g and α are well constrained, as theoretical velocity–porosity relationships derived from my inverted models are consistent with laboratory data (Figures 3-7a and b). On the other hand, I observed that *RMSE* values vary only slowly with K_g and α in the vicinity of the minimum, for sulfide and silicified rocks (Figure 3-8c and d). This may be because the *P*-wave velocity data measured in the laboratory are widely scattered and difficult to explain by the theoretical velocity–porosity relationships estimated by my inversion (Figure 3-7c and d). The proposed method provides good estimates of K_g and α at low porosity, in basalts and massive sulfides with a sharp trough around the minimum in *RMSE*, in contrast to the broader trough around the minimum in *RMSE* for high porosity silicified rocks and sulfides. As the DEM theory ignores crack-to-crack interactions, it is inapplicable for large–cracks cases. Therefore, I conclude that the analysis of the elastic moduli and crack aspect ratios in the different rock types suggests that the DEM theory is an appropriate choice for low porosity media.

The scattering of *P*-wave velocity data could be related to the difference in pore geometry (crack shape), fabric or degree of fracturing or mineralogy of the ore deposit within the same lithology. The same rock type having different index properties could also be explained by the variation of cementation and silicification from sulfide to silicified rocks, or a different hydrothermal regime. In active hydrothermal deposits, the fluid in cracks often exhibits abrupt changes of its bulk modulus because of phase transformations induced by temperature changes or pressure changes (Nishizawa, 1982). A large velocity change should appear when liquid in cracks turns into gas or is replaced by other minerals (Nishizawa, 1982; Eng et al., 2017). Furthermore, mineralogy affects seismic velocities through the bulk and shear moduli of the solid matrix of the rock, which are primary inputs to the forward calculation in DEM theory. Variation of bulk and shear moduli of the solid matrix would induce variation of effective velocity as I observed the variation of *P*-wave velocity by introducing uncertainties into grain elastic moduli (Figure 3-2).

Since the DEM theory used in my inversion assumes a randomly oriented crack distribution with a constant aspect ratio and constant grain elastic moduli for the same lithology, my inversion would be difficult to apply for core samples with anisotropic pore geometries and heterogeneous mineral compositions. I calculated the degree of anisotropy of P-wave velocity of all samples. The anisotropy of most samples was less than 15% (Figure 3-9). If I assume that samples with anisotropy larger than 15 % are anisotropic samples and remove them from the inversion, I obtain similar results (i.e., similar crack aspect ratio).

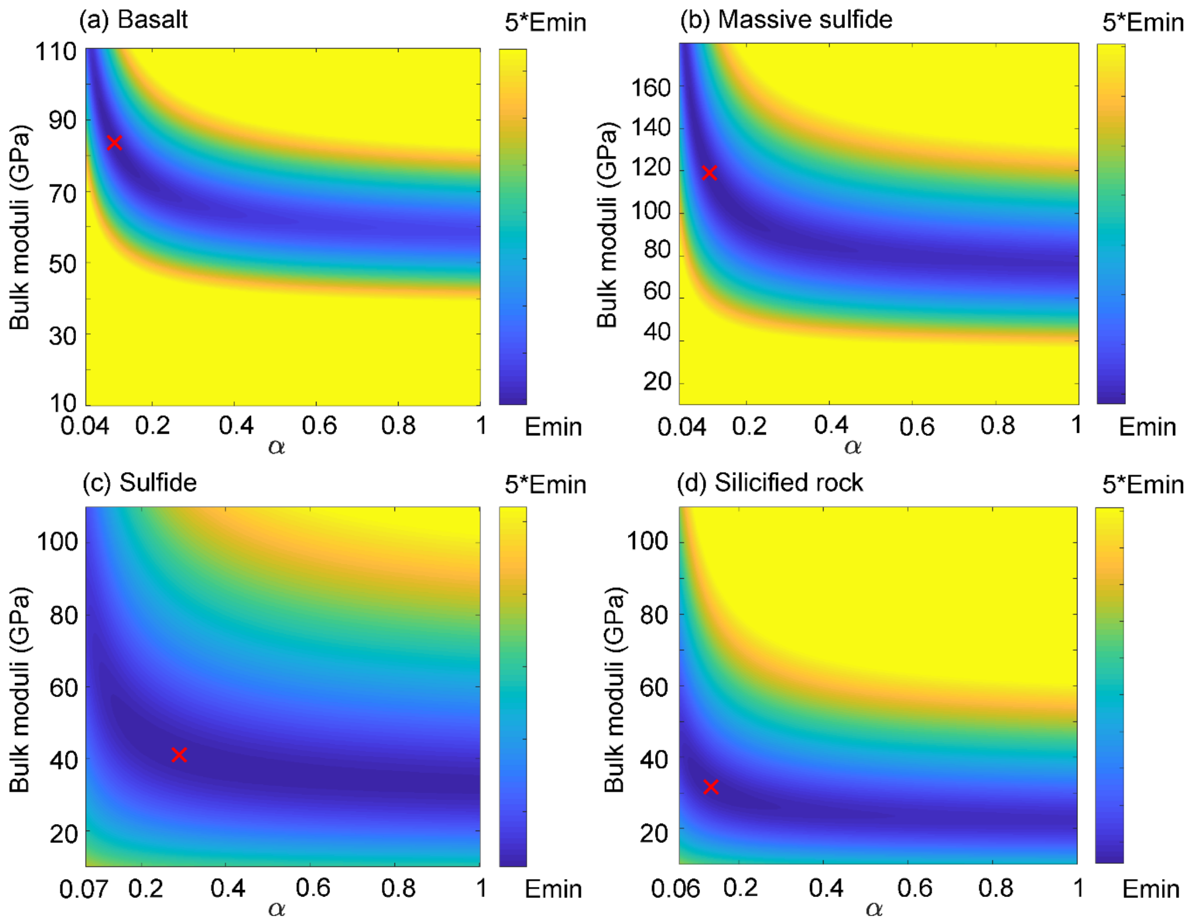

***Figure 3-8**. Distribution of RMSE obtained by grid search inversion for (a) basalts (Juan de Fuca Ridge), (b) massive sulfide (Ore deposit), (c) sulfide (Ore deposit) and (d) silicified rocks (Ore deposit). Red symbols represent the model parameters with the minimum RMSE values (Emin). The colour scale represents RMSE values scaled by Emin for each case.*

***Table 3-2**. Ratio of μ_g to K_g (μ_g/K_g) assumed in inversion and inverted K_g and α.*

	μ_g/K_g (GPa)	K_g (GPa)	α
Basalt	25.6/75.6	83.575	0.109
Massive sulfide	32.3/75.2	118.825	0.112
Sulfide	34.7/53.8	41.125	0.29
Silicified rock	33/39	31.675	0.134

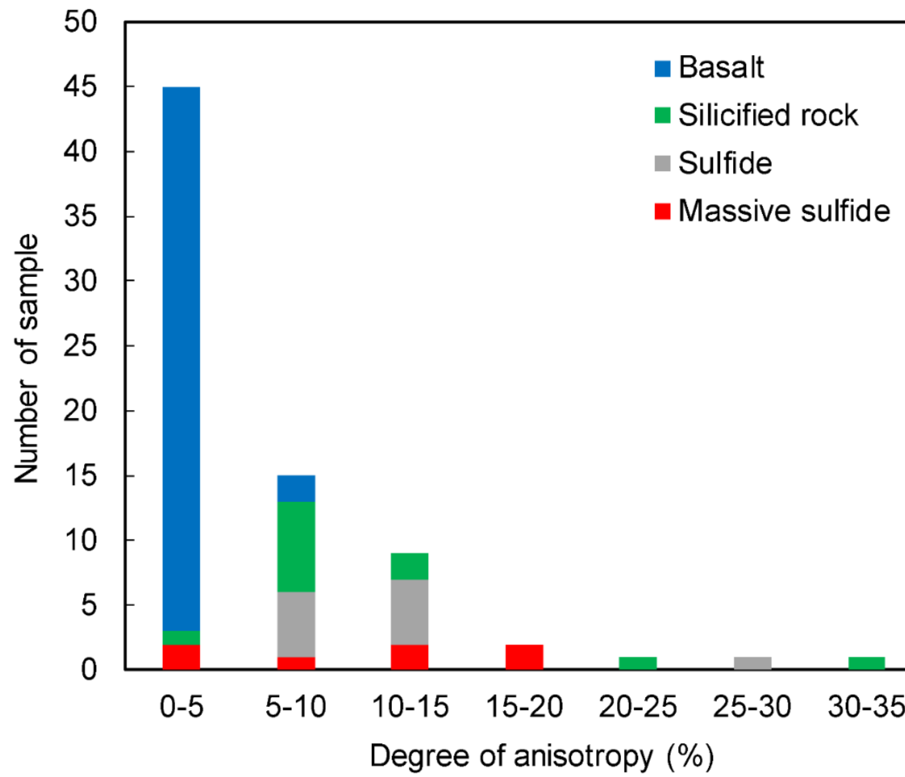

***Figure 3-9.** The distribution of degree of anisotropy of P-wave velocity of all measured samples.*

In this study, furthermore, I used physical and elastic properties measured at atmospheric pressure. The cracks are developed by decreasing the effective stresses as samples are brought to the surface, and the seismic velocity decreases at atmospheric pressure. Therefore, laboratory experiments have been often conducted under in-situ effective pressure conditions. To evaluate the influence of effective pressure upon the estimated aspect ratio, I compared the results of 100 discrete samples measured at atmospheric pressure and 10 samples at higher effective pressure (Tsuji and Iturrino, 2008). I found that samples measured at atmospheric pressure and under higher effective pressure have a similar relationship between velocity and porosity and have a similar averaged crack aspect ratio (~0.05–0.1). This indicates that only a small proportion of thin cracks are closed when pressure is increased. Therefore, my proposed method can be used to estimate the average crack aspect ratio of samples measured at atmospheric pressure.

3-5 Interpretation

I compared the crack aspect ratios estimated in this study with microscopic images of similar lithologies (Figure 3-10). I analysed the petrography for massive sulfide (Figure 3-10b) and sulfide (Figure 3-10c) samples. I further used microscopic images of silicified rocks (Figure 3-10d) and basalt (Figure 3-10a) obtained at the same drilling sites from the previous studies (Yamasaki, 2016; Fisher et al., 2011). The microscopic images from core samples taken using an optical petrographic microscope showed the textural complexities and pore fabrics. Although the crack aspect ratio estimated by my grid-search inversion in this study is an averaged value, and accounts for the elastic properties (i.e., velocity), I clearly find that the pore aspect ratio of sulfide (Figure 3-10c) is larger than that other lithologies, and the crack aspect ratio in the basaltic samples (Figure 3-10a) is smaller than in the other lithologies. These microscopic observations are consistent with the crack aspect ratio estimated in the inversion based on DEM theory (Figure 3-7).

In the inversion results for grain bulk moduli and crack aspect ratios (α) of each lithology (Table 3-2), massive sulfide, sulfide and silicified rocks derived from the same geological zones show distinct characteristics. The grain bulk modulus of massive sulfide is larger than that of basalts, sulfide and silicified rocks. The bulk modulus of sulfides is small, possibly due to intense silicification from sulfide to silicified rocks. The bulk modulus of silicified rocks is relatively small possibly due to the abundance of clay minerals and small crack aspect ratios. Basalts exhibited high bulk modulus possibly because of an abundance of plagioclase and clinopyroxene minerals.

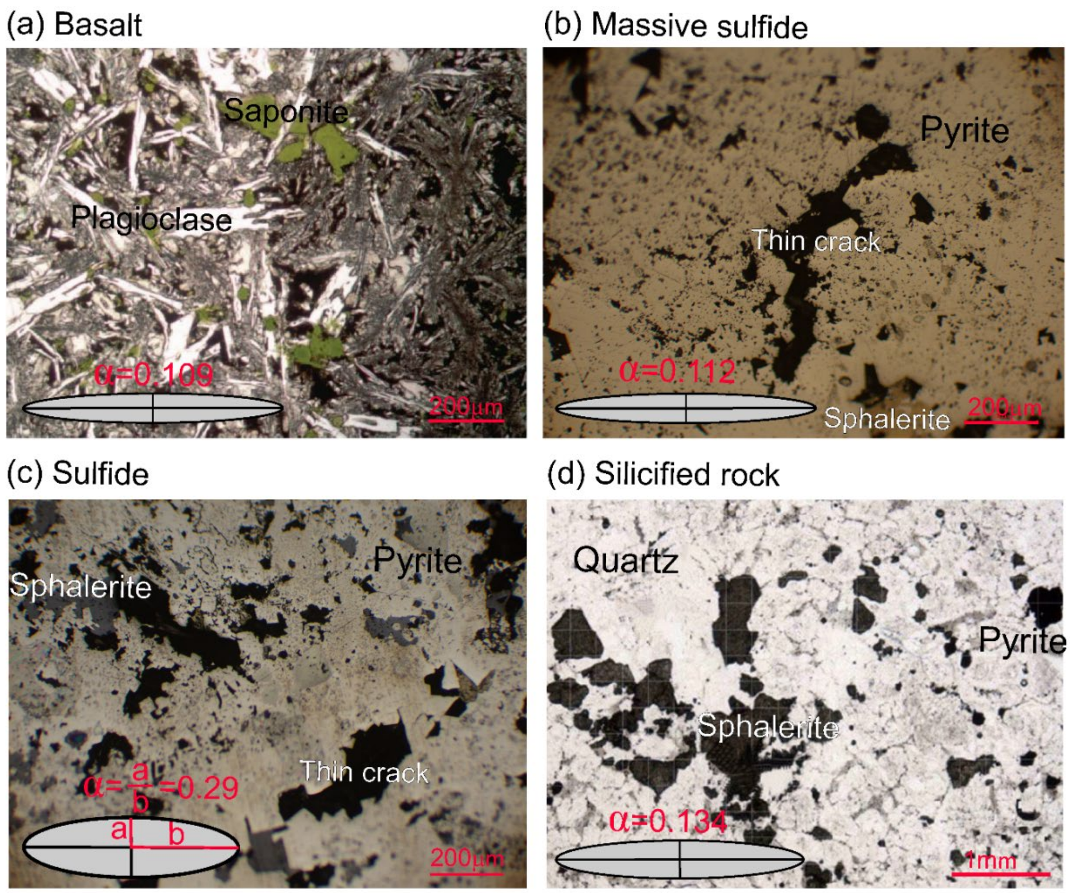

Figure 3-10. *Microscopic images taken from core samples of (a) basalt (Fisher et al., 2011), (b) massive sulfide, (c) sulfide and (d) silicified rock (Yamasaki, 2016), showing the complex texture and pore fabric. The penny-shaped crack symbol displayed in each panel is the corresponding shape estimated in my inversion.*

3-6 Conclusion

To estimate the grain elastic moduli and crack aspect ratio from *P*-wave velocity data measured in the laboratory, I have proposed a grid-search inversion method based on DEM theory. I demonstrated the feasibility of my inversion using synthetic data. I then applied my proposed method to *P*-wave velocity–porosity relationships constructed from laboratory measurements on core samples of oceanic basalt and hydrothermal ore deposit with different lithologies. My key findings are summarized below.

- The velocity–porosity relationships derived from the inverted models using the DEM theory were well consistent with those derived from laboratory measurement. I can therefore model the pore geometry of basaltic rocks and ore deposits. Although my method does not consider anisotropic media, cannot be applied to high porosity samples, and does not use measured S-wave velocity, my approach, using physical properties measured at atmospheric pressure, is easy to apply to predict pore geometry and elastic moduli.
- The *RMSE* distribution obtained in the grid-search inversion method enables us to evaluate the uncertainty of the estimated crack aspect ratio and grain elastic moduli. I could use the information derived from my analyses for reservoir characterization (i.e., physical and hydraulic property estimation) using permeability models based on crack aspect ratios (e.g., Sarout, 2012).

3-7 Appendix

Analytical computation of effective bulk elastic modulus (K^*)

I describe a Runge-Kutta scheme (Berryman et al., 2002) used to solve the ordinary differential equations in DEM theory (Equation 3-1 and 3-2) for penny-shaped cracks. Here K^* and μ^* are effective bulk and shear moduli, respectively. At the initial time the corresponding y (concentration of inclusion) value is y_o, K^* is equal to K_o and μ^* equals μ_0. The effective bulk modulus at y can be calculated as follows:

$$K^*(y) = K_i + \frac{h}{6}(k_1 + 2k_2 + 2k_3 + k_4), \qquad \text{(A1)}$$

where h is the step size and

$$k_1 = f(y, K^*) = (K_i - K_m)P^{(*2)}$$

$$k_2 = f\left(y + \frac{h}{2}, K_m + \frac{h}{2}k_1\right) = \frac{2P^{(*2)}}{2-h}\left(K_i - K_m - \frac{hP^{(*2)}}{2}K_i + \frac{hP^{(*2)}}{2}K_m\right)$$

$$k_3 = f\left(y + \frac{h}{2}, K_m + \frac{h}{2}k_2\right) = \frac{2P^{(*2)}}{2-h}\left(K_i - K_m - \frac{hP^{(*2)}}{2-h}K_i + \frac{hP^{(*2)}}{2-h}K_m + \frac{h^2(P^{(*2)})^2}{4-2h}K_i - \frac{h^2(P^{(*2)})^2}{4-2h}K_m\right) \qquad \text{(A2)}$$

$$k_4 = f(y + h, K_m + hk_3) = \frac{P^{(*2)}}{1-h}\left(K_i - K_m - \frac{2hP^{(*2)}}{2-h}\left(K_i - K_m - \frac{hP^{(*2)}}{2-h}K_i + \frac{hP^{(*2)}}{2-h}K_m + \frac{h^2(P^{(*2)})^2}{4-2h}K_i - \frac{h^2(P^{(*2)})^2}{4-2h}K_m\right)\right)$$

with the initial condition $K^*(0) = K_m$

Analytical computation of effective shear modulus (μ^*)

Using the same procedures as for computing the effective bulk modulus, I calculated the effective shear modulus using a Runge-Kutta scheme as follows:

$$\mu^*(y) = \mu_i + \frac{h}{6}(k_1 + 2k_2 + 2k_3 + k_4), \quad \text{(A3)}$$

where h is the step size and

$$k_1 = f(y, \mu^*) = (\mu_i - \mu_m)Q^{(*2)}$$

$$k_2 = f\left(y + \frac{h}{2}, \mu_m + \frac{h}{2}k_1\right) = \frac{2Q^{(*2)}}{2-h}\left(\mu_i - \mu_m - \frac{hQ^{(*2)}}{2}\mu_i + \frac{hQ^{(*2)}}{2}\mu_m\right)$$

$$k_3 = f\left(y + \frac{h}{2}, \mu_m + \frac{h}{2}k_2\right) = \frac{2Q^{(*2)}}{2-h}\left(\mu_i - \mu_m - \frac{hQ^{(*2)}}{2-h}\mu_i + \frac{hQ^{(*2)}}{2-h}\mu_m + \frac{h^2(Q^{(*2)})^2}{4-2h}\mu_i - \frac{h^2(Q^{(*2)})^2}{4-2h}\mu_m\right) \quad \text{(A4)}$$

$$k_4 = f(y + h, \mu_m + hk_3) = \frac{Q^{(*2)}}{1-h}\left(\mu_i - \mu_m - \frac{2hQ^{(*2)}}{2-h}\left(\mu_i - \mu_m - \frac{hQ^{(*2)}}{2-h}\mu_i + \frac{hQ^{(*2)}}{2-h}\mu_m + \frac{h^2(Q^{(*2)})^2}{4-2h}\mu_i - \frac{h^2(Q^{(*2)})^2}{4-2h}\mu_m\right)\right)$$

with the initial condition $\mu^*(0) = \mu_m$

3-8 References

Berge, P. A., Fryer, G. J., Wilkens, R. H., 1992. Velocity–porosity relationships in the upper oceanic crust: Theoretical considerations. J. Geophys. Res., 97, 15,239–15,254.

Berryman, J. G., Pride, S. R., Wang, H. F., 2002. A differential scheme for elastic properties of rocks with dry or saturated cracks. Geophysics. J. Int. 151. 597-611.

Carlson, R.L., 2010. How crack porosity and shape control seismic velocities in the upper oceanic crust: Modeling downhole logs from Holes 504B and 1256D. An electronic journal of the earth sciences, volume 11, number 4. doi:10.1029/2009GC002955.

Cerney, B., and Carlson, R.L., 1999. The effect of cracks on the seismic velocities of basalt from site 990, Southeast Greenland margin. Proceedings of the Ocean Drilling Program, Scientific Results, Vol. 163.

Cleary, M. P., Chen, I. W., Lee, S. M., 1980. Self-consistent techniques for heterogeneous media. Am. Soc. Civil Eng. J. Eng. Mech., 106, 861–887.

Eng, C., Ikeda, T., Tsuji, T., 2017. Study of the Nankai seismogenic fault using dynamic wave propagation modelling of digital rock from the Nobeoka Fault, Exploration Geophysics, doi: 10.1071/EG17129.

Fisher, A. T., Becker, K., and Davis, E. E., 1997. The permeability of young oceanic crust east of Juan de Fuca Ridge determined using borehole thermal measurements. Geophysical Research Letters, Vol. 24, No. 11, 1311-1314.

Fisher, A. T., Wheat, C. G., Becher, K., Cowen, J., Orcutt, B., Hulme, S., Inderbitzen, K., Haddad, A., Pettigrew, T. L., Davis, E. E., Jannasch, H., Grigar, K., Aduddell, R., Meldrum, R., Macdonald, R., and Edwards, K. J., 2011. Design, deployment, and status of borehole observatory systems used for systems used for single-hole and cross-hole experiments, IODP Expedition 327, eastern flank of Juan de Fuca Ridge. In Fisher, A.T., Tsuji, T., Petronotis, K., and the Expedition 327 Scientists, Proc. IODP, 327: Tokyo

(Integrated Ocean Drilling Program Management International, Inc.). doi:10.2204/iodp.proc.327.107.2011.

Fisher, A.T., Tsuji, T., Petronotis, K., and the Expedition 327 Scientists, 2011. Proceedings of the Integrated Ocean Drilling Program, Volume 327, Integrated Ocean Drilling Program Management International, Inc.,doi:10.2204/iodp.proc.327.101.2011,2011.09

Gardner, G. H. F., Gardner, L. W., Gregory, A. R., 1974. Formation velocity and density-the diagnostic basics for stratigraphic traps: Geophysics, 39, 770-780.

Giambalvo, E.R., Fisher, A.T., Martin, J.T., Darty, L., Lowell, R.P., 2000. Origin of elevated sediment permeability in a hydrothermal seepage zone, eastern flank of Juan de Fuca Ridge, and implications for transport of fluid and heat. Journal of Geophysical Research, Vol. 105, No. B1, 913-928.

Ishibashi, J. I., Noguchi, T., Toki, T., Miyabe, S., Yamagami, S., Onishi, Y., Yamanaka, T., Yokoyama, Y., Omori, E., Takahashi, Y., Hatada, K., Nakaguchi, Y., Yoshizaki, M., Konno, U., Shibuya, T., Inagaki, F., Kawagucci, S., 2014. Diversity of fluid geochemistry affected by processes during fluid upwelling in active hydrothermal fields in the Izena Hole, the middle Okinawa Trough back arc-basin. Geochemical Journal, Vol. 48, pp. 357-369. doi:10.2343/geochemj.2.03111.

Lee, C. S., Shor, G. G., Bibee, L. D., Lu, R. S., Hilde, T. W. C., 1980. Okinawa Trough, origin of a back-arc basin. Marine Geology, 35, 219-241.

Letouzey, J., Kimura, M., 1986. The Okinawa Trough: Genesis of a back-arc basin developing along a continental margin. Tectonophysics, 125, 209-230.

Li, H., Zhang, J., 2010. Modulus ratio of dry rock based on differential effective-medium theory. Geophysics, Vol. 75. No. 2. N43-N50.

Ludwig, R. J., Iturrino, G. J., and Rona, P. A., 1998, Seismic velocity–porosity relationship of sulfide, sulfate, and basalt samples from the TAG hydrothermal mound, in P. M. Herzig, S. E. Humphris, D. J. Miller R. A. Zierenberg, eds. Proceedings of the Ocean

Drilling Program, Scientific Results, 158: College Station, TX (Ocean Drilling Program), 313–327.

Mavko, G., Mukerji, T.,Dvorkin, J., 1998. The Rock Physics Handbook, Tool for Seismic Analysis in Porous Media, Cambridge Univ. Press, U.K.

Neimovic, M.R., Bohnenstiehl, D.R., Carbotte, S.M., Canales, J.P., Dziak, R. P., 2009. Faulting and hydration of the Juan de Fuca plate system. Earth and Planetary Science Letters 284, 94-102.

Nishizawa, O., 1982. Seismic velocity anisotropy in a medium containing oriented cracks-transversely isotropic case. J. Phys. Earth, 30, 331-347.

Norris, A. N., 1985. A differential scheme for the effective moduli of composites, Mech. Mater., 4, 1–16.

Potter, C, C. Miller, S. L. M., Margrave, G. G., 1996. Formation elastic parameters and synthetic P-P and P-S seismograms for the Blackfoot field. CREWES Research Report - Volume 8.

Sarout, J., 2012. Impact of pore space topology on permeability, cut-off frequencies and validity of wave propagation theories. *Geophysics. J. Int.* 189, 481-492. doi: 10.1111/j.1365-246X.2011.05329.x

Seno, T., 1993. A model for the motion of the Philippine Sea plate consistent with NUVEL.1 and geological data. J. Geophysics. Res., 89, B10, 17941-17948.

Sibuet, J. C., Deffontaines, B., Hsu, S. K., Thareau, N., Le Formal, J. P., Liu, C. S., Act Party., 1998. Okinawa trough back-arc basin:early tectonic and magmatic evolution . Journal of Geo. Research. 30,245-30,267.

METI (2013) Report for the first stage of the program. Development of deep-sea mineral resources (in Japanese). http://warp.da.ndl.go.jp/info:ndljp/pid/8296268/www.meti.go.jp/press/2013/07/20130705003/20130705003-2.pdf.

Tsuji, T., Iturrino, G. J., 2008. Velocity–porosity relationships of oceanic basalt from eastern flank of the Juan de Fuca Ridge: The effect of crack closure on seismic velocity. Exploration Geophysics, 39, 41-51.

Tsuji, T., Tokuyama, H., Pisani, P. C., Moore, G., 2008. Effective stress and pore pressure in the Nankai accretionary prism off the Muroto Peninsula, southwestern Japan. Journal of Geophysical Research, vol. 113. doi:10.1029/2007JB005002.

Tsuji, T., Yamaguchi, H., Ishii, T., Matsuoka, T., 2010. Mineral classification from quantitative X-ray maps using neural network: Application to volcanic rocks, Island Arc, 19, 105-119, doi: 10.1111/j.1440-1738.2009.00682.x.

Tsuji, T., Takai, K., Oiwane, H., Nakamura, Y., Masaki, Y., Kumagai, H., Kinoshita, M., Yamamoto, F., Okano, T., Kuramoto, S., 2012. Hydrothermal fluid flow system around the Iheya Norht Knoll in the mid-Okinawa trough based on seismic reflection data. Journal of Volcanology and Geothermal Research, 41–50. doi: 10.1016/j.jvolgeores.2011.11.007.

Tsuji, T., Kamei, R., Pratt, G., 2014. Pore pressure distribution of a mega-splay fault system in the Nankai Trough subduction zone: Insight into up-dip extent of the seismogenic zone, Earth and Planetary Science Letters, Vol.396, 165-178, doi:10.1016/j.epsl.2014.04.011.

Walsh, J. B., 1965. The effect on the compressibility of rock, J. Geophys. Res.

Wilkens, R. H., Fryer, G. J., Karsten, J., 1991. Evolution of porosity and seismic structure of upper oceanic crust: Importance of aspect ratios: Journal of Geophysical Research, vol. 96, no. B11, 17,981-17,995.

Xu, S., White, R. E., 1995. A new velocity model for clay–sand mixtures, Geophys. Prospect., 43, 91–118.

Yamasaki, T., 2017. Petrography and whole-rock major and trace element analyses of igneous rocks from Iheya North Knoll, middle Okinawa Trough, SIP Expedition CK14-

04 (Exp. 907), *Jour. Gelo. Soc. Japan*, Vol. 123, No. 1, p.23-29, doi: 10.5575/geosoc.2016.0049.

Yu, C., Ji, S., Li, Q., 2016. Effect of porosity on sesmic velocities, eslastic moduli and Poisson's ratios of solid materials and rocks. Journal of Rock Mechanics and Geotechnical Engineering 8, 35-49. http://dx.doi.org/10.1016/j.jrmge.2015.07.004.

Chapter 4

Conclusion

4-1 Conclusion

Fundamental geophysical applications, such as prospecting of oil and gas, need accurate evaluation of the seismic response from the subsurface to assess rock properties and to construct the accurate geophysical subsurface model. Moreover, rock physics model, the part of geophysics concerned with establishing relations between various properties of rocks, has been widely applied for evaluating the presence of reservoir rocks and hydrocarbon on oil and gas exploration expeditions. This thesis concentrates on the new practical study of using high-resolution seismic velocity analysis and rock physics model for reservoir characterization. The new findings are summarized as follow:

Based on the results from high-resolution velocity analysis, I revealed gas hydrate and free gas widely distributed in the Sanriku-Oki forearc basin. High P-wave velocities and low amplitude are widespread above the BSRs, suggesting the presence of gas hydrate, while P-wave velocity lower than 1500 m/s indicating the presence of free gas below the BSRs. Gas hydrate and free gas are widely distributed in the porous slump units. Additionally, heat flow was determined from the depths of BSRs. The distributions of gas hydrate and heat flow are greatly related to gas chimneys, faults observed on seismic profiles providing pathways for fluid in deeply-buried sediments to migrate upward to shallow sediments to form gas hydrate under suitable temperature and pressure. Interestingly, high heat flow (30 to 35 mW/m^2) are correspondent to areas with high concentration of gas-hydrates and free gases above chimney and slump edge. Several gas pockets within strata are accumulated below the BSRs through the edge of slumps and permeable sedimentary layers. Moreover, this study is the first heat flow study in this new gas hydrate province and will provide a good base for understanding the evolution of gas hydrate system in the complex tectonic environment reservoirs.

To estimate the grain elastic moduli and aspect ratio from the core samples of hydrothermal ore deposits, I proposed the grid-search inversion with DEM theory to search a wide range of grain elastic moduli and crack aspect ratio. First, I demonstrated the feasibility of my inversion using synthetic data. Then, I applied my proposed method for P-wave velocity - porosity relationship constructed from laboratory measurement on rock samples acquired at the hydrothermal ore deposits. The velocity-porosity relationship derived from laboratory measurement was well consistent with that using DEM theory for inverted models. I can therefore model the pore geometry of the basaltic rocks and use them for reservoir characterization from seismic data (velocity). Even though my approach does not consider anisotropy and does not use measured S-wave velocity, I can estimate crack aspect ratio and grain elastic moduli from physical properties at the atmospheric pressure. I was able to evaluate the uncertainly of crack aspect ratio and grain elastic moduli using my RMSE distribution obtained in grid-search inversion. By using permeability model based on crack aspect ratios, the crack aspect ratio and grain elastic of rocks could be used for reservoir characterization.

4-2 Future works

Researchers have long speculated that gas hydrates are global phenomenon, occurring in permafrost regions in the deep-water parts of continental margin worldwide. But, the amount of gas hydrate contains enormous amount of natural gas and can eventually be commercial producible energy resource. Gas hydrate deposits have been explored in recent years with recognition that this unconventional resource would possibly be explored and developed with the conventional oil and gas production using seismic reflection method combined with well log data, which is a potential method to reveal the physical properties.

An extension of my work using high-resolution seismic velocity would be applicable to find out more promising geological settings for rigorous reservoir characterization including gas hydrate and free gas saturation (Chhun et al., 2018) and pore fluid pressure estimation (Singha et al., 2014; Tsuji et al., 2014a) via rock physics theories to the seismic data. I will be able to discuss more detail the mechanisms of gas hydrate formations using the relationship between seismic velocity, gas saturation, heat flow and in-situ pore fluid pressure.

Pertaining to rock physics model in CO_2 storage, it is difficult to distinguish the CO_2 saturation from pore pressure increasing, because both effects (high saturation and high pore pressure) decrease P-wave velocity. Using rock physics (DEM theory; Kret et al., 2019), I can distinguish these effects. This is considered as very big problem in monitoring study to clarify the reason of velocity decreasing in monitoring data. However, if I use S-wave velocity (or Vp/Vs), Vp/Vs could increase due to high pore pressure, and Vp/Vs could decrease due to high CO_2 saturation because Vs is almost constant and Vp decreases due to CO_2 injection. Therefore, I believe that Vp/Vs is important parameter to distinguish CO_2 saturation from high pore pressure. If I can clarify which factors (saturation and pore pressure) influence on the Vp (i.e. distinguishing saturation from pore pressure using Vp/Vs), it would be very impacted technology. This research topic can also be applied in gas production as in monitoring data using Vs.

4-3 References

Chhun, C., A. Kioka, J. Jia, and T. Tsuji. 2018. Characterization of hydrate and gas reservoirs in plate convergent margin by applying rock physics to high-resolution seismic velocity model. Marine and Petroleum Geology, 92, 719–732. https://doi.org/10.1016/j.marpetgeo.2017.12.002

Kret, K., Ikeda, T., and Tsuji, T. 2019. Grid-search inversion based on rock physics model for estimation of pore geometry and grain elastic moduli: application to hydrothermal ore deposits and basalt. *Exploration Geophysics*, 1-11. https://doi.org/10.1080/08123985.2018.1548605.

Singha, D. K., Chatterjee, R., Sen, M. K., and Sain, K. 2014. Pore pressure prediction in gas-hydrate bearing sediments of Krishna–Godavari basin, India. *Marine Geology*, *357*, 1-11.

Tsuji, T., Kamei, R., Pratt, R.G., 2014a. Pore pressure distribution of a mega-splay fault system in the Nankai Trough subduction zone: insight into up-dip extent of the seismogenic zone. Earth Planet. Sci. Lett. 396, 165 –178. http://dx.doi.org/10.1016/j.epsl.2014.04.011.

Acknowledgments

I would like to express my sincere gratitude and thank to my supervisor Professor Takeshi Tsuji for accepting me as his PhD student. Professor Tsuji is an excellent professor who has always been ready to give excellent advices; without his assistance, willingness in contributing the essential ideas, encouragement, and help this work will never be successfully completed. I am thankful to him for introducing me to the field of rock physics models and natural gas hydrates. Professor Tsuji provided to me opportunities including the participation in international conferences and scientific exploration cruise.

I am deepest grateful to my co-supervisor assistant Professor Tatsunori Ikeda for his excellent guidance and very valuable suggestions. Professor Ikeda helped me with his great knowledge in computer programming to solve problems related to the inversion codes and the knowledge of rock physics model.

I would like to thank to following thesis examiners Professor Yasuhiro Fujimitsu and Professor Hemanta Hazarika for their guidance, valuable comments, suggestions, and valuable constructive comments to improve the quality of this dissertation.

I thank all members and staffs of Exploration Geophysics Laboratory for their very great and comfortable greeting during my research study and their useful suggestions for me for all circumstances.

I am deeply acknowledge the Japan International Cooperation Agency (JICA) and AUN/SEED-Net program for providing the opportunity to me as a PhD student at Kyushu University. In addition, I would like to thank Kyushu University, particularly the Department of Earth Resources Engineering , Faculty of Engineering, Exploration Geophysics Laboratory.

I thank the Ministry of Economy, Trade and Industry (METI) and Japan Oil, Gas and Metals National Corporation (JOGMEC) for providing the 3D seismic data acquired through the 2008FY METI Geophysical Survey and Basin Evaluation Project “Sanriku Oki 3D”. I also gratefully acknowledge the Japan Agency for Marine-Earth Science and Technology (JAMSTEC), Expedition 327 Scientists and crews for the acquisition of the index properties data.

Finally, a special thanks to my beloved parents, wife, siblings and friends for their warm encouragement, sharing both sadness and happiness, support and love, which provided me the hope that is fuel for my mind to accomplish all works successfully. I desire to share everything I have with you, plain and simply because I do love you.

Kakda Kret

Fukuoka, July 2019